Dissociation of Lithium 11

By

Jon Justin Kruse

A DISSERTATION

Submitted to
Michigan State University
in partial fulfillment of the requirements
for the Degree of

Doctor of Philosophy

Department of Physics and Astronomy

1999

Professor Aaron Galonsky

ABSTRACT

Dissociation of Lithium 11

By

Jon Kruse

Dissociation of the ^{11}Li neutron halo nucleus has been studied. The measurements were kinematically complete, allowing a determination of excitation energy, event by event. The experiment has yielded evidence of a direct breakup mechanism in the dissociation of the nucleus, as opposed to the decay through an excited resonant state. Neutron and fragment momentum distributions were measured, and are also consistent with a direct breakup picture. Finally, the structure of the neutron-unbound nucleus ^{10}Li was also examined.

To perform these measurements, the Beam Sweeping Dipole System was developed.

To my parents.

ACKNOWLEDGEMENTS

I must begin by expressing my sincere gratitude to my advisor, Professor Aaron Galonsky. To a large degree it was sheer luck that brought me to work with you in the summer of 1990. Our collaboration through the following summer and the years of graduate work was no accident, however. Physics graduate school would have a much tamer reputation if every student were fortunate enough to enter the program under the direction of a professor whose primary interest is the well being and advancement of his students. You have been a remarkable teacher, an unwavering advocate, and most of all, a good friend.

I owe a great debt to the entire staff of the NSCL. At some point in my graduate career, nearly every person at the NSCL has gone far out of his or her way to help me along. I must single out Professor Dave Morrissey, who has been an excellent source of professional advice and personal friendship. Also, I must acknowledge my first roommate in Lansing, Renan Fontus. We had many great times together, times that I won't forget soon.

Thank you to Gian DiLoreto, who was always happy to pick up a wrench and help me beat whichever four-wheel drive dead horse was in my garage at the time. Thanks also to Joelle Murray, for pretending to be only mildly annoyed by our nightly screening of *Raising Arizona*. This is a good place to acknowledge Mathias Steiner, who would always offer a chair, anxious to hear my dead horse stories.

Certainly, I have enjoyed many friendships with my fellow graduate students at the NSCL:

Jac Caggiano, my golf partner, I have always appreciated your willingness to pull out a 3-wood and knock a ball into the fairway so that I could nearly kill myself slicing a ball into the next area code.

Chris Powell, I must thank you for being prepared for any situation. Whether we required the fridge in your office or the sleeping bag in your car, you were always ready to deliver.

Barry Davids, my office mate, thanks for always cleaning out the press, and for understanding that mine is one of those special computers that doesn't work unless I pound my desk and scream profanity at it.

Erik Tryggestad, the day you showed up as our REU student was the day I realized I had new friend. Thanks for always being someone I could count on.

Pat Lofy, my boot-legger friend, thanks for always thinking of me when you returned to the land of sky-blue waters.

Don Anthony, I sincerely appreciate the countless meals and favors you and Paola have shared with Jodi and me. Your friendship has made the most trying time of my life very enjoyable, and I'm sure that no better relationship has ever been forged over a single lunch break.

On a more profound level, I must thank my parents, Gene and Vaunceil Kruse. Although only a small fraction of everything you have done for me, your undying commitment to my education has been a gift which I can't begin to repay you for. As far back as I can remember I wanted to be a scientist like my dad, and you have supported me in absolutely every means along the way. I try every day to make you proud – thanks for always telling me when I do.

Finally, I thank my lovely wife, Jodi. I can't imagine completing this task without your strength, your patience, and your love. Thank you for always picking me back up when life knocks me down. Certainly everything I have accomplished so far, and everything I can ever hope to accomplish in the future, pales in comparison to the day I married you. I love you.

Contents

List of Tables

List of Figures

Part I

The Beam Sweeping Dipole and its Associated Fragment Detection System

1 The Beam Sweeping Dipole

We have developed a Beam Sweeping Dipole magnet for use in studies of exotic, neutron rich nuclei. The apparatus includes a vacuum chamber and a variety of charged particle detectors used for kinematically complete measurements of the dissociation of halo nuclei. Section 1.1 provides the motivation for construction of the system, and Section 1.2 describes the characteristics of the magnet itself. The fragment detectors and vacuum chamber are described in sections 1.3 and 1.4. Finally, the operation of the Beam Sweeping Dipole is outlined in section 1.5.

1.1 Motivation: First Generation ^{11}Li(g,2n)^{9}Li Experiment

Of all the isotopes available for study with the development of Radioactive Nuclear Beam facilities, none has received the attention given to ^{11}Li. One of the first studies of ^{11}Li to be performed at the NSCL was a kinematically complete measurement of the coulomb dissociation of ^{11}Li into a ^{9}Li and two neutrons [1,2,3]. Performed in 1991 by Sackett et al., the experiment was designed to map out the electric dipole excitation function for ^{11}Li and study ground state n-n correlations of ^{11}Li. To do this, experimenters placed a lead target in a beam of 30 MeV/A ^{11}Li nuclei. The coulomb field of the lead nucleus acted as a field of virtual photons, capable of exciting the ^{11}Li nucleus. ^{11}Li has no bound excited states, and the energy required to remove two neutrons from ^{11}Li is only 300 keV, so most excitations of ^{11}Li to an energy greater than

300 keV resulted in dissociation of the nucleus into a ^{9}Li and two free neutrons. By measuring the energies and angles of the ^{9}Li fragment and both neutrons, Sackett et al. were able to perform an event-by-event reconstruction of each dissociation and determine the excitation energy for each event. A diagram of the experimental setup used in that measurement is shown below.

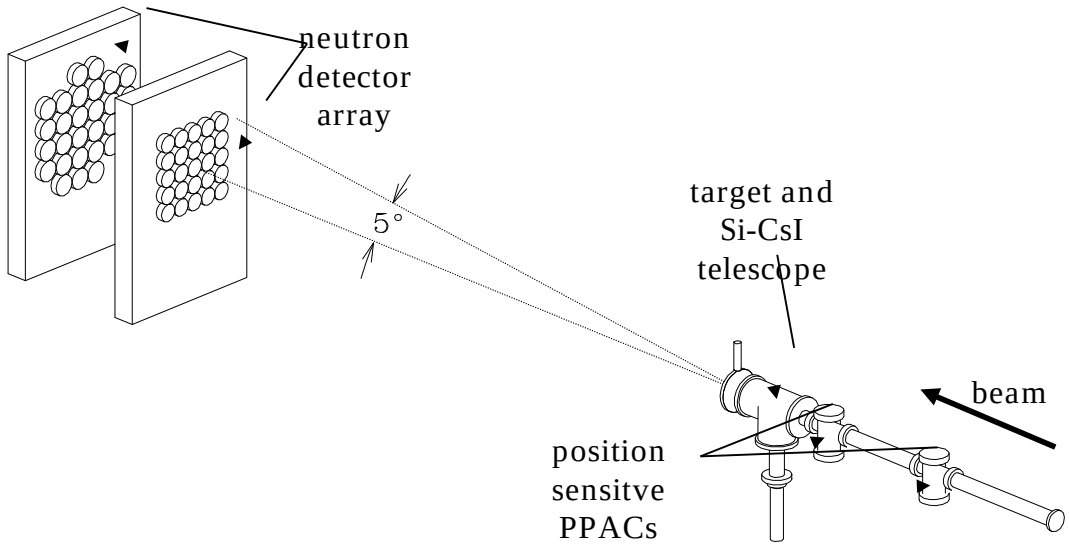

Figure 1 -- Experimental setup used by Sackett et al. in 1991 to measure the complete kinematics of ^{11}Li(g,2n)^{9}Li.

To perform the 1991 experiment, Sackett et al. produced a beam of 30 MeV/A ^{11}Li with the A1200 fragment separator. Before impinging on a lead target, the ^{11}Li nuclei passed through a pair of Parallel Plate Avalanche Counters (PPAC's) [19]. Each PPAC provided an (x,y) position measurement of the location of the beam particle on the detector. Used together, the two PPAC measurements determined the direction of each beam particle's velocity, as well as its point of interaction on the lead target. The lead target had a thickness of 598 mg/cm^2, producing a ^{11}Li dissociation in approximately 1% of the projectiles. A typical coulomb excitation event provided only a few hundred thousand electron volts of decay energy, shared among the fragment and two neutrons. Because the ^{9}Li fragment and neutrons were moving through the lab with an energy of

approximately 28 MeV/A, all of the reaction products left the target in a small, forward focused cone. Because of this focusing effect, the fragment detectors were a small telescope of silicon and cesium iodide detectors situated directly behind the target. Similarly, the neutrons were detected by two small arrays of liquid scintillation detectors centered at zero degrees. The arrays were located at five and six meters downstream from the target to allow for time-of-flight measurements of the neutrons' energies.

Since the execution of the 1991 ^{11}Li experiment, significant improvements have been made in the neutron detection arrays. The arrays shown in Figure 1 were made up of 54 individual, six-inch diameter containers. The detectors were five-inch diameter cylindrical volumes filled with liquid organic scintillator and coupled to two-inch photomultiplier tubes by lucite light pipes. When the cylindrical detectors were stacked into a tight array, the geometry produced a minimum 50% dead space between the detectors, decreasing the array's efficiency. The array also contained a high fraction of mass such as lucite and phototubes, which scattered neutrons but was not active neutron-detecting material. These two arrays of individual detectors have been replaced with the NSCL Neutron Walls, a pair of 2m x 2m liquid scintillator arrays, which will be described in section 3.2.2.

Another significant improvement over the equipment used by Sackett *et al*. lies in an entirely new fragment detection system. The fragment array used in 1991 was a three element, 5 cm x 5 cm Si/CsI telescope. Located six inches downstream from the target, the first element of the array was a 300μm thick silicon strip detector. One side of the detector had an array of 16 3.125mm wide horizontal strips which collected free electrons, while the other side had 16 vertical strips which collected electron holes. These strips effectively divided the detector into an array of 256 (x,y) pixels, facilitating a measurement of the angle at which the fragments emerged from the target. In addition, the pulse height of the signal from the silicon detector gave energy loss information, which was used to identify the isotope of each fragment in a ΔE-E plot. Directly behind

the silicon strip detector was a standard 5cm x 5cm, 300μm thick silicon detector, whose purpose was to provide additional energy loss information. Finally, the third element of the telescope was a CsI scintillator crystal read out by four PIN diodes. The CsI crystal stopped all fragments and beam particles and provided a measurement of their total energies.

The three element telescope performed a number of tasks – it measured the energies and angles of fragments, as well as serving as a Faraday cup, stopping and counting all unreacted beam particles. Unfortunately, despite the thickness of the lead target, only approximately 1% of the ^{11}Li particles dissociated in the target. Of the remaining ^{11}Li particles which were to be stopped and counted by the fragment array, about another 1% dissociated in the silicon or CsI detectors. Such a dissociation event produced a ^{9}Li at some point in the detector stack, and two neutrons which could be detected by the neutron array. Most of these events could not be distinguished from the actual target events, and so a significant portion of the beam time was devoted to running with no target, so that the contribution from the fragment array could be measured and subtracted. A Monte Carlo simulation of the experiment showed that the dominant contribution to the width of the decay energy resolution came from the thickness of the target, and the experimenters' inability to determine exactly where in the target and at what energy the ^{9}Li was created. Use of a thinner target would have improved the experimental resolution, but would also have resulted in an even smaller dissociation rate, causing the experiment to be dominated by dissociations in the detector stack. It was in order to perform such experiments with a thinner target, while at the same time reducing the ratio of detector to target dissociations that the Beam Sweeping Dipole was developed.

1.2 The Beam Sweeping Dipole

The fragment detection system used in a kinematically complete measurement performs a variety of functions. It measures the angle at which charged fragments leave the reaction target and determines the isotopic identity of each fragment. It also stops the fragments, measures their kinetic energies, and provides a time reference signal for time-of-flight measurements of neutron energies. Because the charged fragments generally exit the target at very small angles relative to the beam axis, the detectors also serve as a Faraday cup, stopping and counting unreacted beam particles.

The fragment detection system developed for our most recent coulomb excitation experiments involves the use of a Beam Sweeping Dipole magnet. The reaction target is placed at the opening of a large dipole magnet. If dissociation occurs in the target, the neutrons and fragment leave the target in a small, forward-focused cone. The neutrons travel straight through the field and find the neutron detection array situated at zero degrees. The fragment, however, is swept by the magnetic field through an angle before being stopped by a detector. Likewise, unreacted beam particles are also swept through an angle before being stopped, so that if they react and dissociate in the detector, the neutrons produced leave the vacuum chamber at a sufficient angle that they either miss, or can be shielded from the neutron detectors. Because only coincidence measurements of a fragment and two neutrons permit a determination of excitation energy, dissociations of beam particles in the detector are eliminated as a source of background.

The magnet we obtained for such experiments is a former beam-line dipole magnet from the Bevalac at Berkeley. It is a 7-ton, room temperature, c-shaped magnet which originally had a pole gap of 6 inches. With a six-inch opening, a 1000 ampere current produced a peak magnetic field strength of approximately 1.7 Tesla. The pole faces, which are 13 inches wide 24 inches long, are surrounded by coils, which means that a neutron produced in the target must travel nearly 40 inches downstream before it has left the 6 inch vertical aperture of the magnet. This aperture corresponds to a vertical

half-angle of only 4.3 degrees. Although the neutrons produced by the coulomb excitation of halo nuclei are very forward focused, the magnet was meant to be used in conjunction with the 2m x 2m Neutron Walls. When located 5 meters downstream from the target, a Neutron Wall detector subtends a vertical half angle of 11.3 degrees. Looking from the target through the magnet, only 75 centimeters of the detector's 2m height would be visible to neutrons we would like to detect. To better utilize our neutron detection system, the dipole was dissasembled and an additional 1.5 inches of steel was inserted in the return yoke of the magnet, increasing the vertical gap to 7.5 inches. The peak magnetic field strength in the pole gap was decreased to approximately 1.5 tesla, but the increased vertical aperture of the device improved the acceptance of our neutron detectors.

To facilitate the design of a fragment detection system and data analysis, the field of the magnet was mapped after its aperture was increased to 7.5 inches. The mapping surface was a 4-foot by 8-foot sheet of plywood reinforced with aluminum rails for stiffness. Rows of brass pins were partially driven into the wood to create channels which could accommodate an aluminum meter stick. A hall probe was fastened to the meter stick, and the vertical component of the magnetic field was recorded at one inch intervals as the meter stick traveled through one channel. At the end of a channel, the meter stick was removed and placed in the neighboring channel for the next row of measurements. A total area of 38 inches by 64.8 inches was mapped, on a grid size of 1 inch by 1.2 inches, resulting in 2184 points per map. The corners of the mapping surface were supported by lab jacks, so that the board could be leveled, and its elevation could be changed to map various planes in the magnet's gap. The midplane of the magnet was mapped several times and averaged, and in addition, the planes one-inch below midplane, and 1, 2, and 3 inches above the midplane were mapped. The maps of planes one inch above midplane and one inch below midplane were compared to confirm the field's vertical symmetry about the midplane. Only the vertical component of the field was

measured, but the other components were determined to have a negligible effect on the fragments in the experiment. Figure 2 below shows a schematic sketch of the dipole magnet, illustrating the orientation of the magnetic field maps with respect to the magnet.

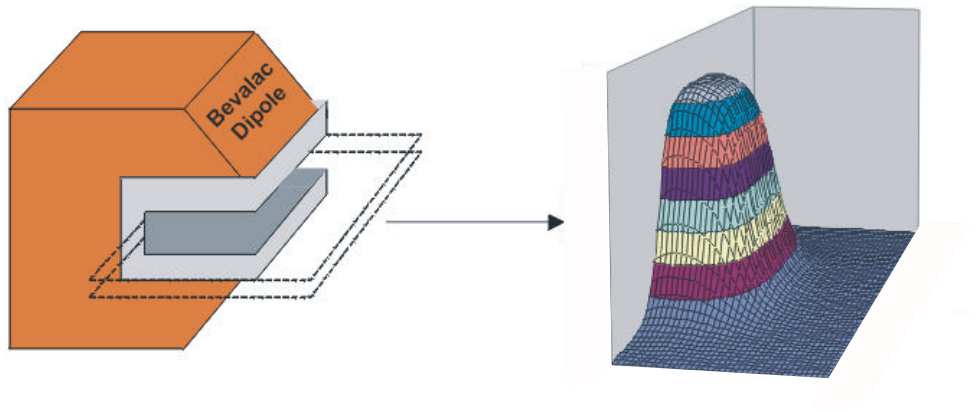

Figure 2 -- Orientation of the mapping plane with respect to the Beam Sweeping Dipole.

Figure 3 shows charts of four of the planes mapped – from midplane to three inches above midplane.

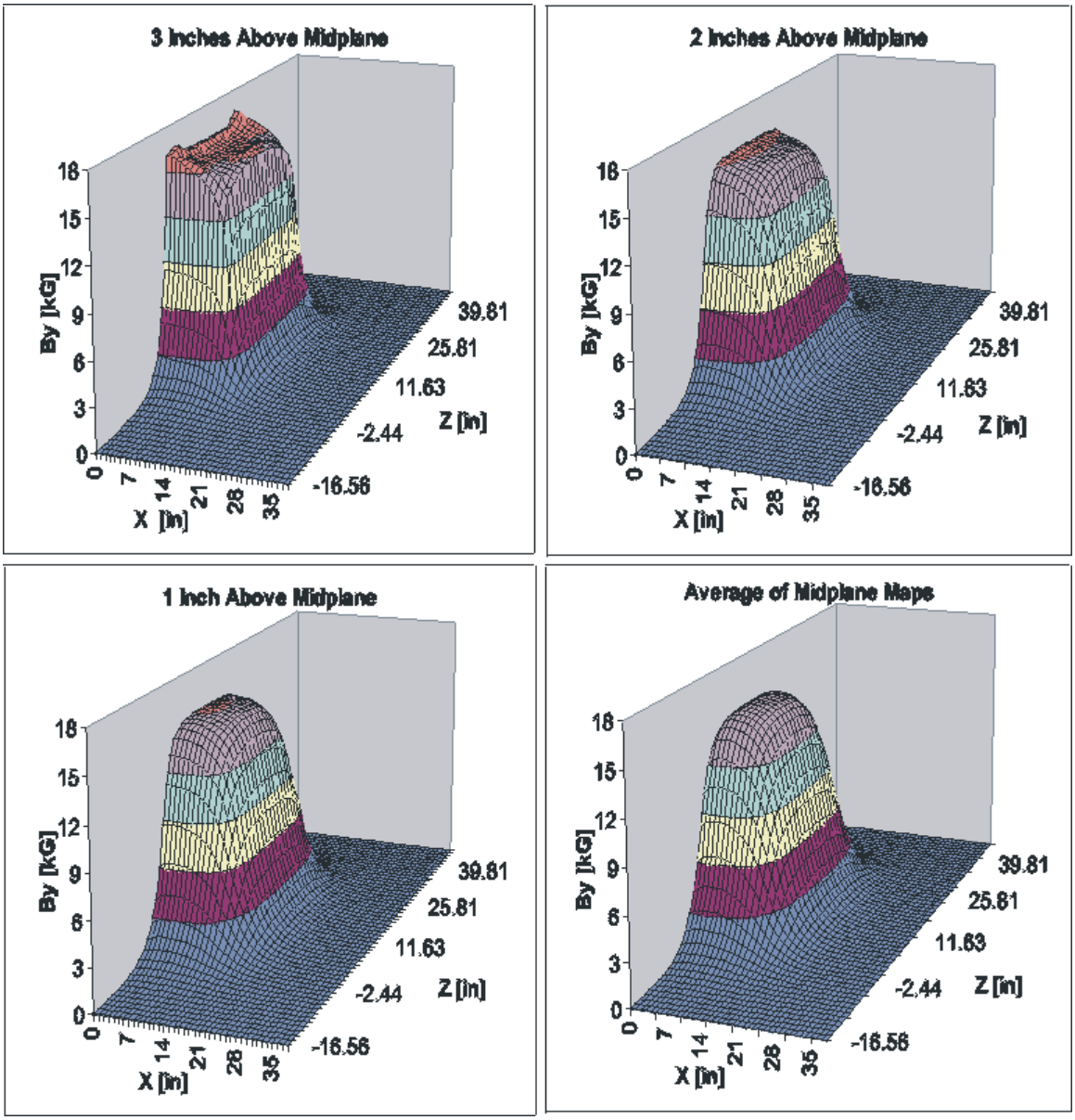

Figure 3 -- Maps of the vertical component of the magnetic field of the Beam Sweeping Dipole, displayed for four of the planes measured.

1.3 Fragment detection

A kinematically complete measurement of dissociation events requires that we measure the energy and angle of all fragments produced. Analysis of the experiment also requires an isotopic identification of each charged particle as well as a count of the total number of beam particles incident upon the target. A three-element array was developed to perform these tasks in conjunction with the Beam Sweeping Dipole. The first element is a pair of gas-filled Parallel Plate Avalanche Counters (PPAC's), identical to those used by Sackett *et al*. They measure each beam particle's position at two points upstream from the target, indicating each particle's point of intersection with the target. The second element is a pair of silicon strip detectors placed 6 inches downstream from the target, between the coils of the magnet. The detectors provide a measurement of the angle at which the fragments leave the target. They also supply an energy loss measurement to be used for particle identification. The third portion of the system is a large plastic scintillator array placed downstream from the exit of the magnet at an angle to the beam axis. The plastic array stops charged fragments produced in the target and measures their energies. The array also stops and counts all beam particles which left the target unreacted. Below is a diagram of the Beam Sweeping Dipole, and the associated detector system.

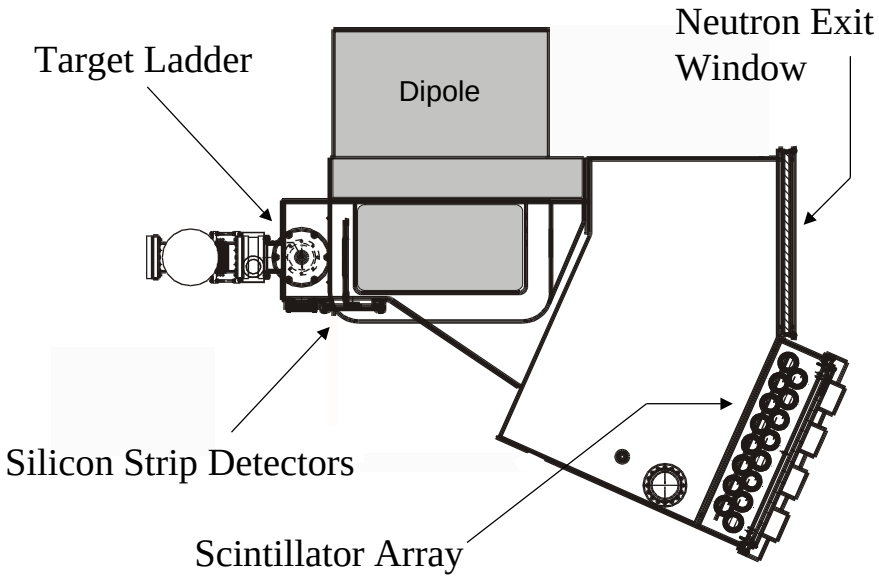

Figure 4 -- Diagram of the Beam Sweeping Dipole, its vacuum chamber, and associated detectors. The beam enters the chamber from the left. Not shown are the position sensitive PPAC detectors, upstream from the target.

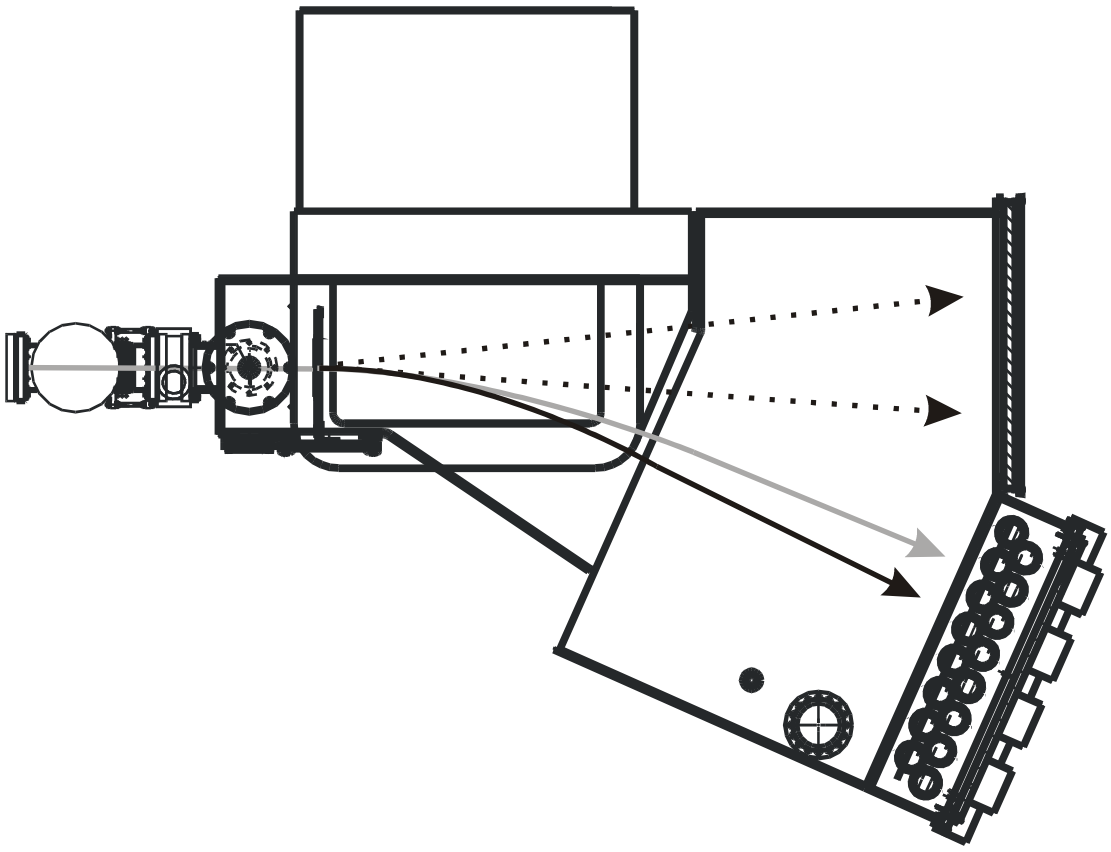

Figure 5 -- Particle trajectories through the magnet. The grey curve shows the path of an unreacted ^{11}Li particle through the magnet, while the solid black curve shows the path of a ^{9}Li fragment created in the target. The dotted lines represent the paths of two neutrons produced in coincidence with the ^{9}Li.

1.3.1 Silicon Detectors

Ideally, the complete kinematics of the reactions would be determined without placing any detectors at zero degrees behind the target, as they could contribute background events to the experiment. However, a measurement of the angle at which a fragment left the target, using only detectors at the exit of the magnet, would require very precise knowledge of the magnetic field, as well as a computationally intensive analysis. Furthermore, because it would be a considerable distance from the target, such a position sensitive detector would have to be quite large, and consequently expensive and fairly difficult to handle. Therefore, silicon strip detectors were placed directly behind the target at zero degrees for the purpose of measuring the fragments' angles, but there was no stopping detector there. While the silicon detectors are a source of background events, their contribution relative to the target is much smaller than that made by the former zero-degree telescope.

In the 1991 experiment, the fragment telescope, which was a problematic source of background, consisted of a 300-μm silicon strip detector, followed by another 300-μm silicon detector, and finally a 1.2-cm thick CsI crystal. In contrast, the newer configuration uses only 250 μm of silicon behind the target. In the present ^{11}Li experiment, a total of 1115 ^{9}Li-2n coincidences were detected with the lead target in place. Less than 20% of those were created by reactions in the silicon detectors. The contribution of the silicon detector to the set of coincidence events was efficiently measured using one of the reaction targets -- a 120 mg/cm^2 aluminum target. Because of the equivalence between silicon and aluminum as target nuclei, the 120 mg/cm^2 of aluminum combined with the 58 mg/cm^2 of silicon in the strip detectors effectively acted as one target. The increased reaction rate provided by the aluminum target meant that

less beam time was devoted to measuring the reaction contribution from the silicon detectors.

The silicon strip detectors, produced by MICRON, are 250 μm thick, cover an area of 5cm x 5cm each, and have opposing 3.125 mm wide strips on each surface to facilitate an (x,y) position measurement. A novel feature of these detectors is that unlike conventional silicon strip detectors, which are framed on all four sides with a G-10 mount, the side of the frame opposite the cable connection is trimmed away from these detectors. Their active areas extend completely to one edge of each device so that, when aligned side by side, they actively cover a uniform 5-cm x 10-cm area. The detectors are mounted six inches downstream from the target, directly between the coils of the magnet. At a distance of 6 inches from the target, a 3.125 x 3.125 mm2 pixel subtends an angle of approximately 1.2°. In Figure 6 is a photo of the strip detectors, mounted on an ISO flange which bolts to the vacuum chamber.

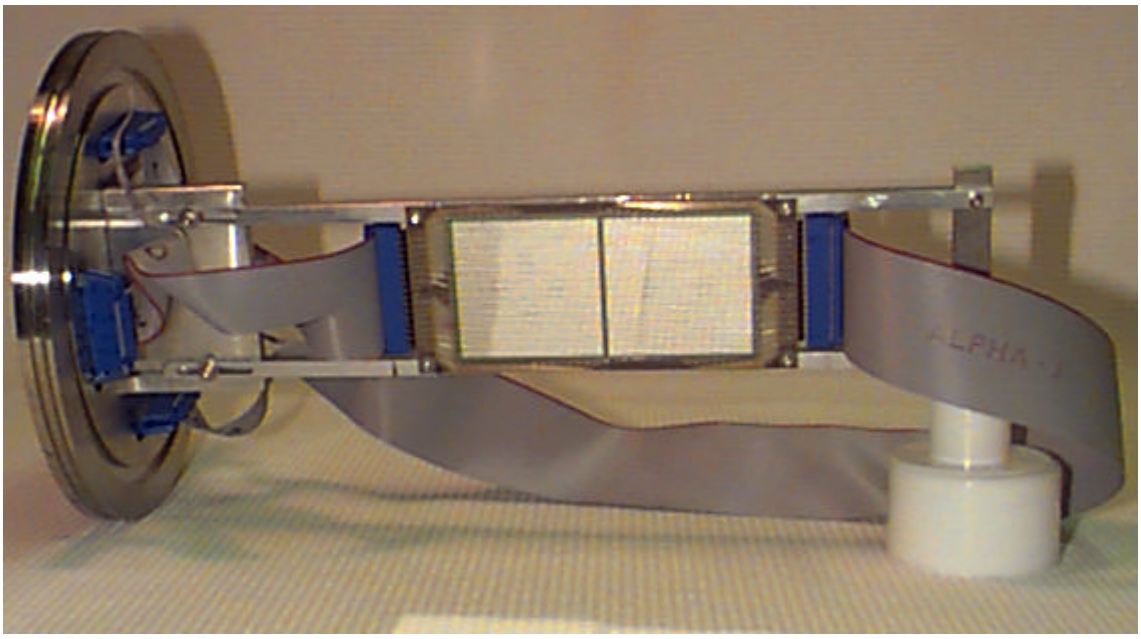

Figure 6 -- The silicon strip detectors. The 3.125 mm horizontal strips are visible on the front surfaces. The flange at left bolts to the vacuum chamber to suspend the detectors at zero degrees behind the target.

The signals from the silicon strips are amplified by a set of MSU constructed S800 pre-amps and shaped by Washington University built, CAMAC controlled shapers. The shaped signals are digitized by Philips peak-sensing ADC's, providing an energy loss measurement, as well as x-y pixel information for an angle measurement. In addition to being shaped and digitized, the pre-amp signals are boosted by MSU built quad fast amplifiers and processed by LeCroy CAMAC constant-fraction discriminators, providing a time signal from the detectors.

1.3.2 Scintillator Array

After the silicon strip detectors, the remaining tasks to be performed by the fragment detection array are to stop and measure the total energy of the charged fragments, as well as stop and count the unreacted beam particles. This is accomplished with the use of a plastic scintillator array. The array is located outside the magnet, 60 inches downstream from the target location, with its normal at an angle of 23.4 degrees with the beam axis. The array is constructed of 16 bars of Bicron BC-408 fast plastic scintillator, and covers a total area of 40.64 x 64 cm2. The system is made up of 16 vertical bars of plastic, each 4 cm wide, 2 cm thick, and 40.64 cm long. A 2" photomultiplier tube (PMT) views each end of each scintillator bar. The PMT's are 8575 Burle, and similar Hamamatsu tubes, with a photocathode diameter of 45.7 cm. The 2 cm thickness of the scintillator bars is somewhat greater than the ranges of light fragments with energies of around 30 MeV/A. Given a 2 cm thickness, a 4 cm width is chosen for the bars so that the entire cross-sectional area can be covered by the photocathode of an 8575 PMT without use of a light pipe, as light pipes would have necessitated the construction of a taller vacuum chamber. Because the cross-sectional size of the PMT's is larger than that of the scintillators, the bars are staggered into two parallel planes, one plane 4.75 cm behind the other. This arrangement provides uniform coverage of the exit plane of the magnet by the plastic array. The horizontal size of the array is designed to stop both very rigid unreacted beams such as ^{8}He, as well as

fragments such as ^{4}He which the magnet sweeps through a much larger angle. Because of the large angle through which ^{4}He fragments are deflected, they actually leave the magnet between the side coils, and not at the downstream end of the device. Such a trajectory means that they travel a shorter distance between the poles of the magnet and therefore see a larger vertical aperture defined by the poles. The height of the scintillator bars, 16 inches, is chosen to catch ^{4}He particles which emerge from between the magnet's poles at the maximum vertical angle.

The surfaces of the scintillator bars are not treated by wrapping or aluminum deposition, so that all scintillation light created within a cone of critical angle with respect to the scintillator surfaces is transmitted to the ends of the bars by total internal reflection. Approximately 60% of the scintillation light is emitted at angles less than the critical angle and escapes the bar, but 'cross-talk' effects in which the escaped light triggers neighboring phototubes is not found to be an important effect. As the totally internally reflected light travels from its origin to each of the two phototubes, the only losses are due to exponential attenuation by the plastic. The characteristic length of this absorption, 300 cm, is considerably longer than the 40 cm length of the scintillators. Still, to account for what attenuation occurs, the geometric mean of the two PMT signals is calculated. The mean of the two signals compensates for the exponential loss, and a position independent pulse height measurement is achieved.

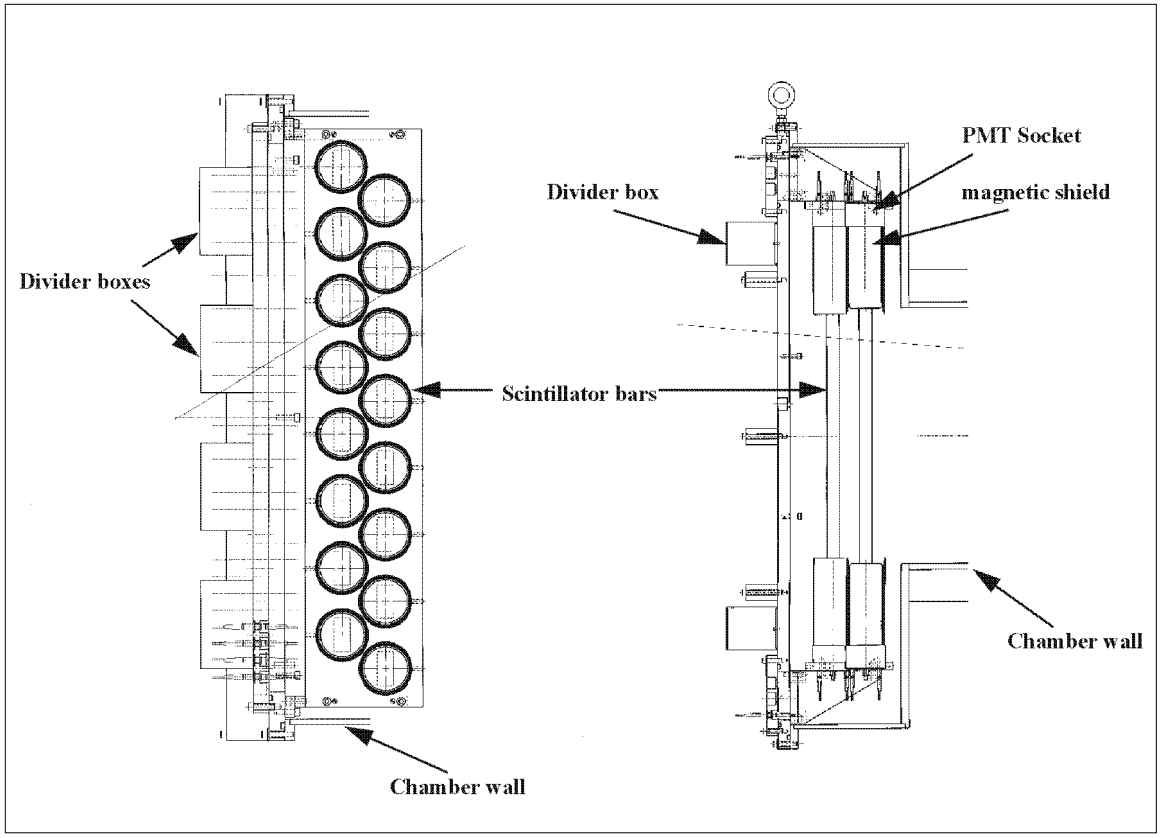

Figure 7 -- CAD drawings of the plastic scintillator array at the exit of the Beam Sweeping Dipole.

The PMT's are biased and read out by high voltage bases built at the NSCL. The bases are modified versions of the Hamamatsu model E394 base. The first modification to the Hamamatsu design is that the resistors in the NSCL version have half the resistance of the Hamamatsu version. This doubles the bleeder current through the device, assuring

linearity for large pulses. The second modification is that the bases are split into two separate modules. Inside the vacuum chamber a socket device containing the capacitive portion of the circuit is connected directly to the PMT's. These sockets are connected via ribbon cable feed-throughs to the resistor chains on the outside of the vacuum chamber. The voltage dividers are placed outside the vacuum to dissipate heat generated in the resistors, preventing gain drifts from resistive heating, and damage to the system caused by excessive heating of the bases. Two signals are pulled from each phototube base. In addition to the anode pulse, which was integrated by a charge to digital converter for an energy measurement, a signal from the eleventh of the twelve dynodes is inverted and used for timing purposes.

To monitor what gain drifts do occur, a blue light emitting diode is fixed to the face of each PMT. The LEDs are fired at a rate of 1 pulse per second throughout the experiment, and the resulting PMT signals are recorded along with the experimental data. Offline analysis showed that over the course of a several week experiment the gain drifts of the PMTs were negligible compared to the resolution of the scintillator array.

Vacuum Chamber

The last piece of equipment constructed for use with the Beam Sweeping Dipole is a vacuum chamber to contain the detectors and couple the system to the beamline. The chamber was make of stainless steel rather than aluminum because its strength allowed the chamber to be constructed with thinner walls, maximizing the vertical aperture of the chamber between the poles of the magnet. The vacuum chamber consists of three regions. The first region couples to the beamline and fits between the poles of the magnet. Like the rest of the chamber, it is constructed of ¼" walls, so the interior height of the chamber between the poles is 7". The next section of the chamber begins at the exit of the magnet and has an interior height of 16.5", to allow fragments to see the entire vertical height of the scintillator bars. The last section of the vacuum chamber houses the scintillator array, and so it is 36" tall, to facilitate the plastic bars and their phototubes.

At the far upstream end of the vacuum chamber, it is coupled to the beamline through a gate valve. In the beamline is a pair of gas-filled PPAC detectors used to measure the incoming beam particles' direction. PPAC detectors are damaged by rapid pressure changes, and so the gate valve can be closed to isolate the chamber from the beamline, allowing rapid pump down and venting of the chamber while the PPAC's stay under vacuum of the beamline. Between the gate valve and the magnet are vertical lengths of pipe extending above and below the chamber. A large target ladder, capable of holding 7 reaction targets 2" high and 3" wide is mounted in the pipe. The target ladder is manipulated by a push rod that can be run up or down by hand to change the reaction target.

Six inches downstream from the target ladder, between the coils of the magnet, are located the silicon strip detectors. The detectors are mounted on an aluminum rail that is bolted to an ISO flange on one side of the chamber. The flange includes feed-throughs for all cable connections to the detectors, and can be quickly removed and replaced with a standard blank-off for work in the chamber that does not involve the silicons. A mounting rack for the silicon preamps was built which can be clamped to the chamber to ensure a solid ground between the vacuum chamber and the preamp cases. When bolted into place, the preamps are suspended directly in front of the feed through flange, allowing the cables between the preamps and the flange to be only a few inches long, minimizing their tendency to pick up noise.

The performance of a silicon detector is impaired by thermal noise in the device, and these detectors are placed between the coils of a room temperature magnet that becomes considerably warmer than room temperature when operating. In test runs with the device, we found that as the magnet coils warmed the vacuum chamber, radiative heating of the silicons from the chamber walls quickly increased the leakage current of the detectors and impaired their resolution. To prevent such heating, a copper shroud was built and installed inside the chamber between the pole faces, shielding the detectors from

the warm surfaces of the vacuum chamber. The shroud is a box with a rectangular opening for the beam particles to enter, and the entire downstream end is open for fragments to leave the detector over a large range of angles. The shroud is insulated from the vacuum chamber by ceramic feet, and copper lines are soldered onto its surface. Cold domestic water flows through the lines, cooling the shroud and shielding the silicon detectors from the warm chamber walls. When the magnetic field is ramped up or down, eddy currents in the copper shroud tend to pull it around the chamber. To fix it in place, two stainless steel studs were welded to the chamber, and the shroud was bolted down.

Immediately outside the magnet's coils, both on the open side of the magnet and the downstream end, is the junction between the first and second regions of the vacuum chamber. With an inside height of 16.5", the second region of the chamber allows charged particles created in the target to see the entire height of the scintillator array. This portion also is constructed of ¼" stainless steel, with the exception of a neutron exit window, centered at zero degrees on the back wall of the chamber. To minimize scattering of the target neutrons in flight to the Neutron Walls, this window is made from a plate of aluminum Hex-Cel material, which is bolted to the chamber with an aluminum frame and sealed with an o-ring. Though it is strong enough to support the atmospheric load of the vacuum, the 19.5" x 26" window weighs only ~3lbs(?), compared to 36 lbs. for a stainless steel sheet of similar dimensions.

The third and final portion of the vacuum chamber is a box which houses the plastic scintillator array. The back wall of this section of the chamber is a 3/4" thick aluminum plate bolted to the chamber and sealed with an o-ring. The scintillator array is mounted on this plate, so that the entire assembly can be removed from the chamber in one piece, and the plate replaced with a blank-off for work not requiring the scintillator array.

The purpose of the magnet is to prevent neutrons produced in the fragment detectors from reaching the Neutron Wall arrays. Although a 21 MeV/A ^{11}Li beam is

bent by an angle of 22 degrees before stopping in the plastic, the sweeping of the beam alone is not enough to ensure that no neutrons from the detectors will reach the Walls. Using the maps of the magnetic fields, the trajectories of unreacted beam particles are calculated through the magnet to determine where they strike the scintillator array. Directly outside the vacuum chamber, behind this region of the plastic array, a large stack of neutron shielding is assembled to absorb detector neutrons as they exit the chamber. In the 1996 ^{11}Li experiments, this shield was an 8" thick stack of brass and copper. While it greatly reduced the flux of neutrons from the plastic array to the Walls, the data contained a significant number of ^{9}Li-n coincidences that were the result of reaction in the scintillators. However, because of the absorption of neutrons by the shielding, the set of ^{9}Li-n-n coincidences showed an insignificant contamination from detector events. For subsequent experiments, the brass and copper shielding was replaced by a 12" thick stack of steel. In addition, two 2" thick copper shielding bars were bolted to the inside of the aluminum detector plate, behind the region of the scintillator array struck by unreacted beam. The additional shielding essentially eliminates one neutron coincidences resulting from reactions in the plastic array.

1.5 Operation of the System

1.5.1 Energy measurement

In the ^{11}Li dissociation experiment, the silicon strips were calibrated with secondary beams of ^{4}He at 20 and 25 MeV/A, and ^{9}Li at 20 and 25 MeV/A. The last quadrupole doublet in the beamline was defocused to illuminate the entire silicon array with each calibration beam. The ^{9}Li particles lost approximately 10 MeV in the silicon, and the detectors measured the loss with a resolution of approximately 6%, FWHM. The measured energy loss spectrum from the 20 MeV/A ^{9}Li beam in the silicon detectors is shown in Figure 8, as is the calibration curve for the array.

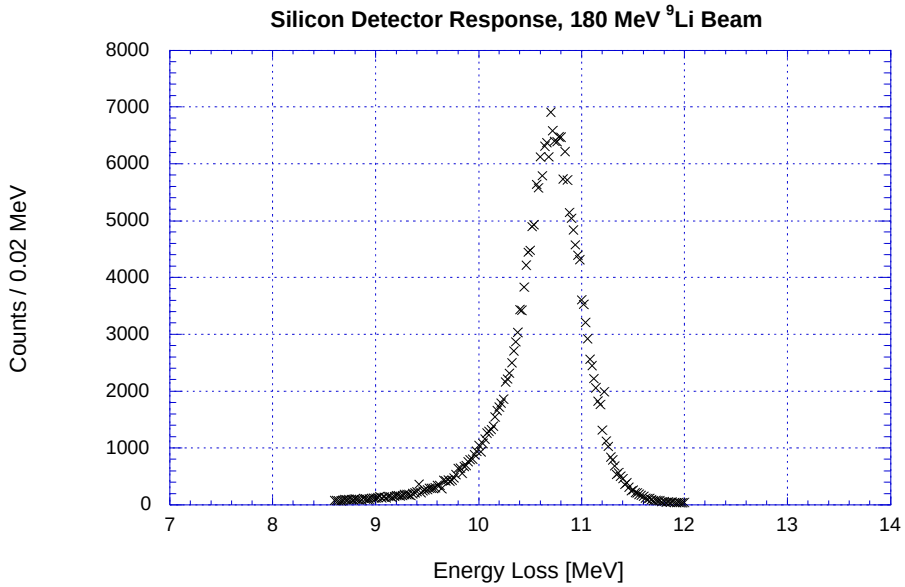

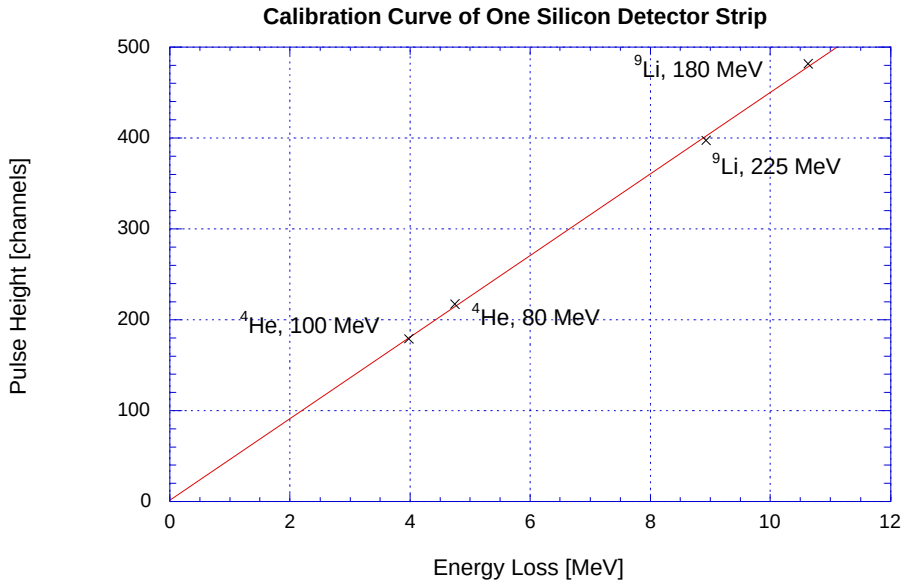

Figure 8 -- Detector response and calibration of silicon strip detectors

The scintillator array was calibrated with the same ^{4}He and ^{9}Li beams used to calibrate the silicon strip detectors. The field of the dipole magnet was adjusted to sweep the focused beams over the scintillator array, illuminating as many bars as the bending power of the magnet would permit. The pulse height of scintillation light produced in the plastic bars is not directly proportional to the amount of energy deposited in the detector by the fragment. For our purposes, an acceptable parameterization of the light production is achieved by the method developed by D. Cebra, *et al*. [4] All detectors are gain matched, and then the pulse height is converted to light in units of MeV electron equivalent by the equation:

$$L=0.265(E^{1.39}/Z^{0.78}A^{0.41})$$

where E is the total energy of the fragment in MeV, and Z and A are the atomic and mass numbers of the fragment. For each calibration beam, the measured pulse height is plotted against the calculated light production for that isotope and energy. The points are fit with a line, and the fit is used to convert from pulse height to ^{9}Li energy. For ^{9}Li particles of 25 MeV/A, an energy resolution of 4% FWHM was achieved. Shown in Figure 9 is the pulse-height to energy calibration curve for a scintillator bar, as well as the response of the detector to a calibration beam of ^{9}Li particles.

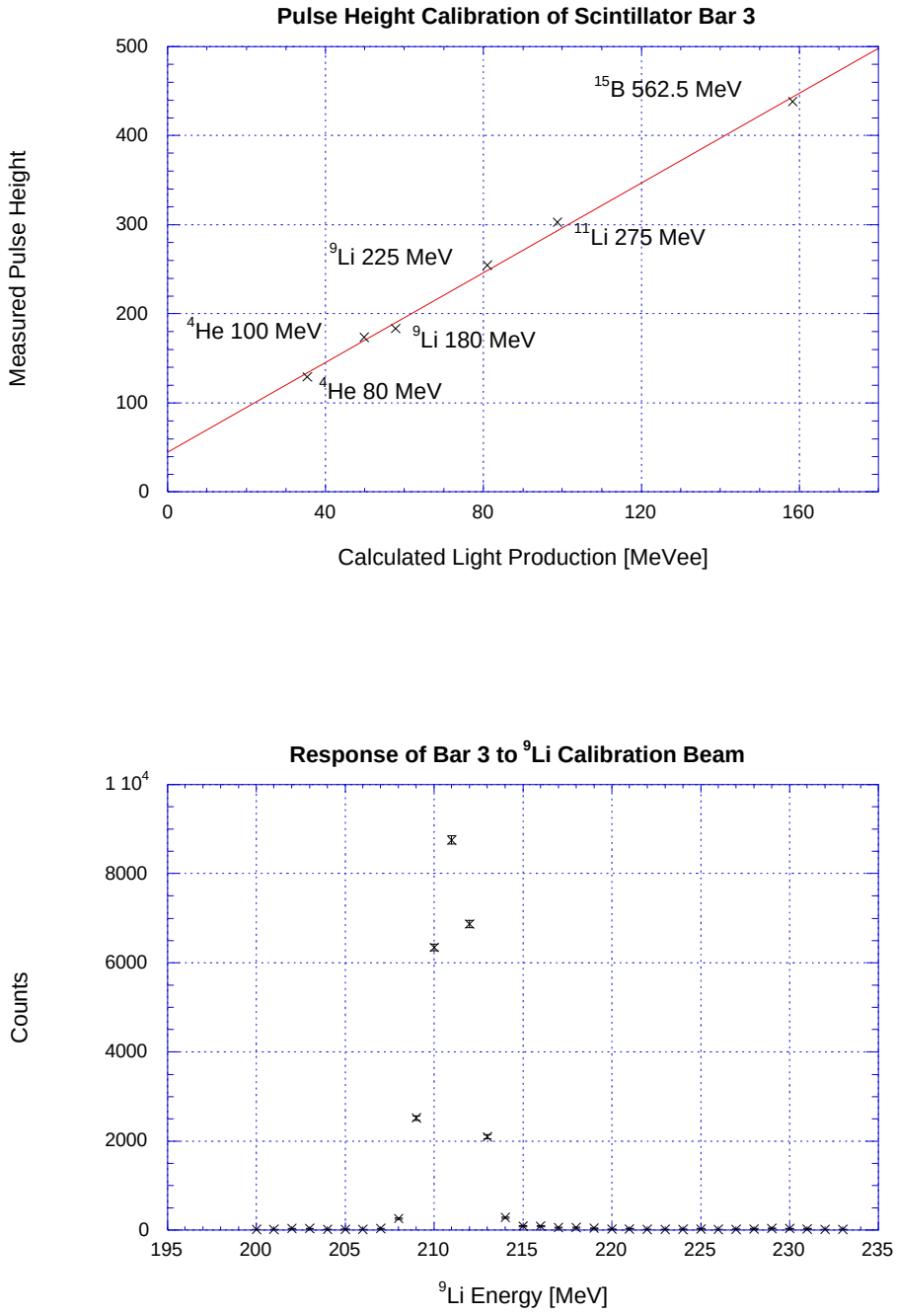

Figure 9 -- Top: Pulse height measured in scintillator bar 3 vs. calculated light production for each calibration beam, as well as a number of experimental beams. Bottom: Pulse height resolution of bar 3 in response to a 216 MeV ^{9}Li calibration beam. The width of the peak is 4% FWHM.

1.5.2 Particle Identification

Isotopic identification of charged fragments and beam particles is achieved by the ΔE-E method. For each particle, the energy loss measured by the silicon detectors is plotted against the total energy measured by the silicon and the plastic bars. Shown below is a ΔE-E plot measured between the silicon strips and the scintillator array in the ^{11}Li experiment.

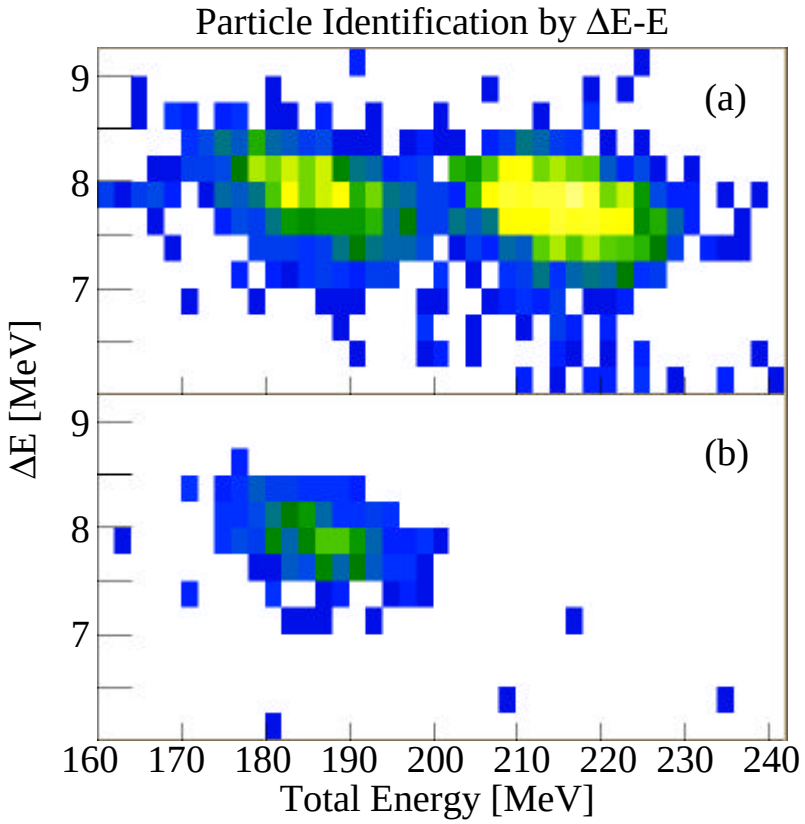

Figure 10 -- DE-E plots from ^{11}Li experiment. Only the region around ^{11}Li and ^{9}Li is shown. a) ^{9}Li and ^{11}Li for all event types, including fragment singles as well as 1n and 2n coincidences. b) Particle identification plot for fragment – 2n coincidences only.

Because the neutron shielding behind the scintillator bars in the ^{11}Li experiment was not entirely effective at absorbing detector neutrons, the ΔE-E spectra from bars which stopped the ^{11}Li beam show some contamination between the ^{9}Li and ^{11}Li regions of the plots. This contamination is caused by ^{11}Li particles which lost some of their energy in the detector before dissociating and liberating two neutrons. The neutrons then carried off energy not detected by the scintillator, yielding a lower than normal energy measurement for that particle. However, the shield was effective enough that the set of ^{9}Li-2n coincidences show no such contamination. A plot of ΔE-E for ^{9}Li-2n coincidences is shown in Figure 10, part b.

1.5.3 Time-of-Flight Reference

To perform a time-of-flight (TOF) measurement of neutrons detected in the Neutron Walls, the fragment detection system must also provide a time signal when the fragment leaves the target. Ideally, this signal would come from the silicon strip detectors, as the six inch flight path between target and detector would require a negligible correction for the fragment's flight time. However, in the vicinity of the dipole magnet power supplies, the fast outputs of the silicon pre-amps are prone to noise pickup problems, and the system is unstable. A more reliable time signal is obtained from the dynode signals of the plastic array PMTs. To compensate for the varying transit times of the light in the scintillators at different detection points, the average of the time signals from each bar's two PMTs is calculated. The inherent timing resolution of the scintillator bar - Neutron Wall combination is illustrated by events in which the primary beam reacts in the plastic of the fragment array, creating γ rays which are detected by the Neutron Walls. A TOF spectrum for γs created by an ^{18}O beam in the bars is shown in Figure 11. There are six channels per nanosecond, and the resolution of the γ peak is 0.8 ns, FWHM.

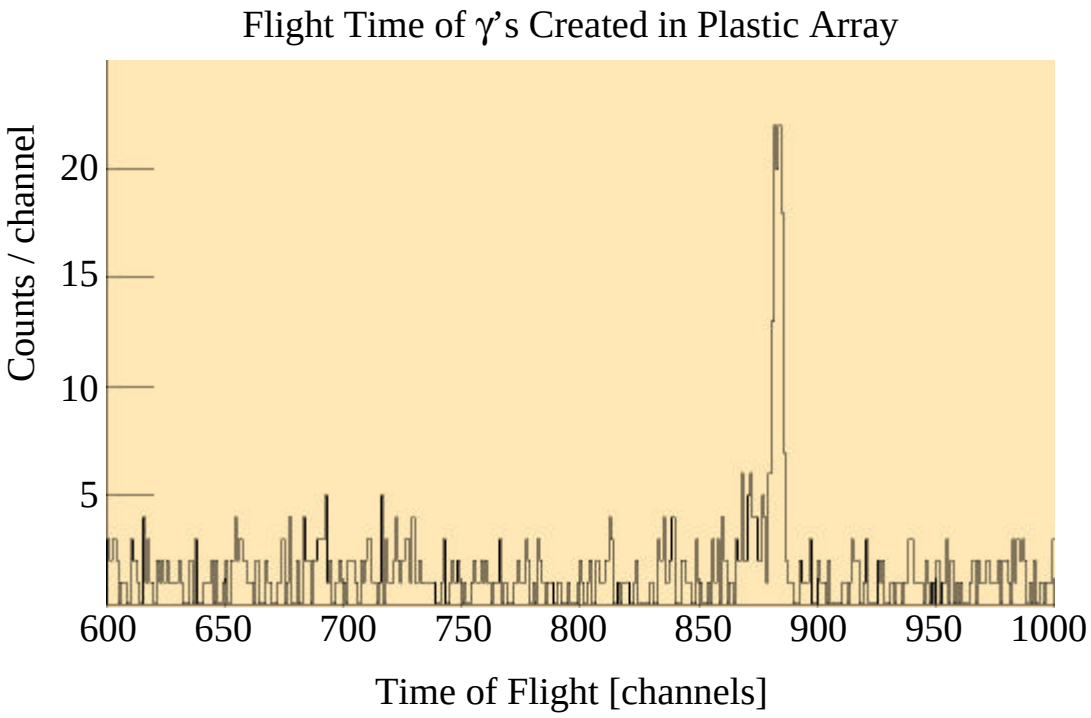

Figure 11 -- TOF of g-rays created in scintillator bars by a beam of ^{18}O and detected by the Neutron Walls. The peak has a resolution of 0.8 ns, FWHM.

In addition to the γ spectrum shown above, the timing of the scintillator array -- Neutron Wall system is calibrated with a ^{60}Co γ source. The source is positioned inside the vacuum chamber near the silicon detectors, and γ-γ coincidences are recorded between the scintillators and the Neutron Walls. Because of the small pulse height of these events, the time resolution of the ^{60}Co coincidence spectrum is inferior to the spectrum from beam induced γ rays produced in the scintillators. However, a long acquistion time with the source provides excellent statistics, and even with a resolution of 3.5 ns, FWHM, these data provide adequate time calibration for bars which do not show a γ peak induced by beam particles. Figure 12 shows a ^{60}Co timing calibration for one scintillator bar vs. the front Neutron Wall.

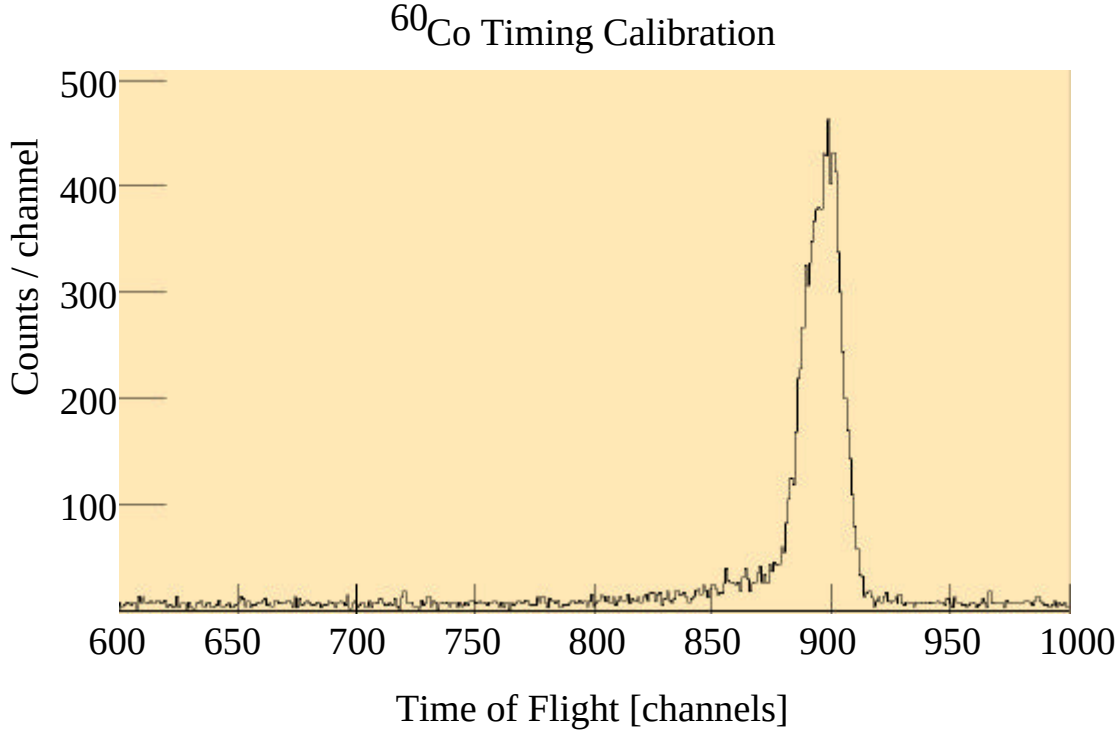

Figure 12 -- ^{60}Co timing calibration for one bar vs. front Neutron Wall. The peak has a resolution of 3.5 ns, FWHM.

When measuring the TOF of neutrons and γs created in the target, a correction is made for the flight times of the fragments travelling from the target to the bars, because the time signal from the bars is used as the neutron TOF stop. Using the magnetic field maps, a fragment's trajectory can be calculated through the magnet using a fourth-order Runge-Kutta integration routine, as described in Numerical Recipes [5]. The scintillators are positioned with respect to the magnet such that, over a broad range of energy and incident angle, the flight path between the target and the front surface of the plastic array is nearly constant for a fragment of a given isotope. For ^{9}Li fragments, varying in energy from 20 to 30 MeV/A, and ranging in angle into the magnet from –10 to 10 degrees, the flight paths from the target to the front of the plastic array differ by less than 2 cm, or approximately one third of a nanosecond. While no correction, therefore, is necessary for a fragment's energy or angle, an additional 4.75 cm of flight path length is added for events in which the fragment is detected by even-numbered bars, compensating for the stagger of the array. (See Figure 7) After a fragment's energy is determined from the size of the light pulse, its velocity is calculated, and an event by event determination of each fragment's TOF from target to detector is calculated. This correction is added to neutron TOF measurements. The resolution of this method could not be determined for the ^{11}Li experiment because insufficient statistics prevented the detection of a prompt γ peak originating in the target.

1.5.4 Rejection of Detector Dissociation Events

As discussed earlier, the neutron shielding used behind the scintillator array in the ^{11}Li experiment did not entirely eliminate detector events from the set of fragment - 1n coincidences. However, 1n coincidence events could be analyzed free of contamination from scintillator reactions by rejecting data from scintillator bars which stopped the unreacted beam. Because of the difference in magnetic rigidity between ^{11}Li and ^{9}Li, more than half of the true ^{9}Li-1n target events were retained by this method without

contribution from detector reactions. The bars which received the highest flux of ^{9}Li fragments from the target, bars 6, 7, and 8, were struck by no unreacted ^{11}Li beam particles, while the bars which stopped the majority of the ^{11}Li beam, bars 3 and 4, detected a much smaller portion of ^{9}Li fragments. In a concurrent study of ^{6}He [6], the difference in rigidity between ^{6}He and ^{4}He caused the two isotopes to stop on completely different portions of the array. Ignoring events in bars which stopped the ^{6}He beam allowed us to reject 100% of dissociations in the plastic array, retaining all of the ^{4}He-1n coincidence events which were created by the target.

In addition to target neutrons and neutrons created by reactions in the scintillator bars, we also expect to detect neutrons which are 'in-scattered' – that is – neutrons which are created in the target but arrive at the Walls by a path other than a direct flight from target to detector. In order to measure the intensity of in-scattered neutrons as well as neutrons created in the scintillator array, a device known as a shadow bar is used. The shadow bar is a piece of material placed in the flight path of the target neutrons, between the target and the Neutron Walls. The purpose of the bar is to block neutrons created in the target from reaching one portion of the Neutron Walls, shadowing that region from the neutrons we wish to detect. A typical shadow bar, a 1-foot thick bar of copper, will prevent approximately 95% of the neutrons which strike it from reaching the Neutron Walls. With the shadow bar in place, then, nearly all of the neutrons detected in the shadowed region of the Walls are known to have come from the plastic array, or from the target via in-scattering. In the 1996 ^{11}Li experiment, the shadow bar was a 12" long piece of brass placed at the exit of the vacuum chamber, directly behind the aluminum Hex-Cel window. It cast a 6.4" by 13.4" rectangular shadow on the first Wall, and an examination of the position distribution of neutron events on the first Wall displays the magnet's ability to suppress detector reactions and in-scattered neutrons as a source of contamination to the coincidence data.

Below are position distributions of neutrons detected by the front Neutron Wall in the ^{11}Li experiment. Figure 13 a) shows the (x,y) position on the Wall of single neutrons detected in coincidence with a fragment. Figure 13 c) shows the x position of single neutron coincidences, detected only by Neutron Wall cell number 9, a cell that was partially shadowed by the shadow bar. The shadow of the bar is visible in the plots, but there are a significant number of in-scattered and detector neutrons present in the spectra. Figures 13 b) and d) display the same parameters, but only for coincidences in which the fragment was detected by bars 6, 7, or 8. None of these bars stopped unreacted beam particles, and the number of counts in the shadowed region relative to the total is down by a factor of five from plots a) and c). The remaining counts in the shadow are due to in-scattered target neutrons, rather than reactions in the plastic array.

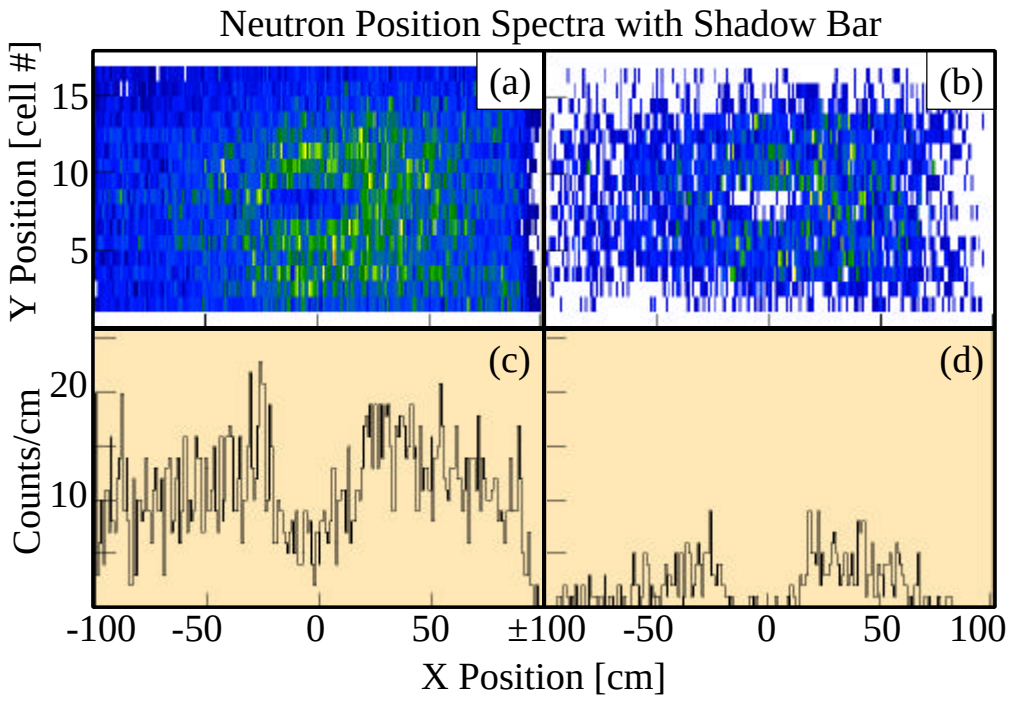

Figure 13 -- Position spectra of neutrons on the front wall with shadow bar in place. Plot a) displays the (x,y) position of single neutrons detected by the front Neutron Wall, in coincidence with a fragment. Plot c) shows the x position of single neutron coincidences detected by Neutron Wall cell number 9. Plots b) and d) are a subset of a) and c), displaying data only for events in which the fragment was detected by scintillator bars 6, 7, or 8.

Part II

Dissociation of ^{11}Li

2 Introduction

One of the most recent experimental techniques to emerge in nuclear physics is the use of radioactive beams. Usually produced by the fragmentation of stable nuclei, beams of radioactive nuclei have given experimenters access to exotic isotopes which have challenged some of the most fundamental tenets of nuclear physics. Perhaps the most studied of all radioactive nuclei is ^{11}Li. The remarkable properties of ^{11}Li were first discovered in an experiment by Tanihata et al. [7]. They created beams of all bound lithium isotopes (^{6,7,8,9,11}Li), and impinged them on a carbon target, measuring the interaction cross section of each isotope. From the interaction cross sections they could determine the matter radii of the projectiles, and found that ^{6,7,8,9}Li behaved exactly as expected. That is, the radius of a nucleus is given by $1.2\ A^{1/3}$ fm, where A is the total number of protons and neutrons in the nucleus. The interaction cross section of ^{11}Li, however, was found to be unexpectedly large, suggesting an extended matter distribution. In the first of many experiments to measure the momentum of ^{9}Li from the fragmentation of ^{11}Li, Kobayashi *et al*. [8] found that the transverse momentum distribution of the ^{9}Li was much narrower than predicted by the Goldhaber model [9] of projectile fragmentation. Like the enhanced interaction cross section, the narrow momentum distribution of the ^{9}Li fragments was interpreted as evidence of a large spatial extent of the ^{11}Li nucleus, specifically with the two valence neutrons forming a diffuse halo around a ^{9}Li core [ST 8,10,11]. It has been found that the halo structure of the ^{11}Li nucleus is caused by the very small binding energy, 0.30 MeV [12], of the two valence neutrons. The small binding energy leads to very long tails on the radial wave functions of the neutrons.

In addition to the large interaction cross section measured by Tanihata, it was found that the dissociation cross section for ^{11}Li was very large on targets of high Z, suggesting a large coulomb excitation cross section. The large cross section was explained in terms of a new type of collective excitation – a soft dipole resonance. [10,13,14] In the soft dipole resonance, the ^{9}Li core oscillates against the neutron halo of the ^{11}Li nucleus. The restoring force of this proposed oscillation is very weak, and so it was expected to occur at low energy, near 1 MeV [10,14].

In an attempt to study the soft dipole resonance of ^{11}Li, Sackett *et al.* [1] performed a kinematically complete measurement of the dissociation of ^{11}Li on a target of lead. The large coulomb field of the lead nucleus acting as a field of virtual photons to the passing ^{11}Li projectiles, excited them. ^{11}Li has no bound excited states, ^{10}Li is neutron unbound, and ^{9}Li is particle stable to 4.06 MeV [15], so coulomb excitation of ^{11}Li up to 4.36 MeV led only to a final state of ^{9}Li and two free neutrons. The energies and angles of the three particles were measured, and each event was reconstructed to determine the excitation energy of the event. The electric dipole strength function was then mapped out and fitted with a Breit-Wigner resonance shape that was consistent with predictions of the soft dipole resonance. However, it was found that, on average, the ^{9}Li fragment was travelling faster in the final state than the two liberated neutrons. This was interpreted as evidence of a direct-breakup mechanism, in which the ^{11}Li dissociated near the lead target nucleus. The coulomb field of the lead nucleus accelerated the free ^{9}Li away, while leaving the velocity of the two neutrons unchanged. The magnitude of this coulomb acceleration effect was used to calculate the lifetime of the ^{11}Li excited state, which was found to be much shorter than the period of a soft dipole resonance. Therefore, they concluded that the picture of a resonant excited state was not appropriate in this case, but rather the dissociation proceeded via a direct breakup mechanism.

Of further interest is the nature of the interaction between the halo neutrons in the ^{11}Li ground state. Because ^{10}Li is neutron unbound, the pairing interaction between the

halo neutrons must be important in the formation of a bound ^{11}Li. Early theories of ^{11}Li suggested that the correlation between the two neutrons is so strong that they form a bound dineutron coupled to a ^{9}Li core [10]. The experiment by Sackett *et al*. [1], as well as others [16,17] has attempted to probe the nature of the neutron-neutron interaction by studying the relative momentum between the two neutrons following breakup. Sackett found that the spectra were well reproduced by a calculation assuming that the ^{9}Li and two neutrons shared the available decay energy via a phase-space distribution, with no correlation at all.

The current work is an extension of the experiment performed by Sackett *et al*. To enhance experimental efficiency at large decay energy, a pair of large area, highly efficient neutron detectors, the Neutron Walls, were constructed. In addition, a new fragment detection system was built, featuring a large dipole magnet to prevent detection of reactions which occurred in the fragment detectors. The experiment was performed with targets of lead, tin, and aluminum. In contrast to lead, where the dominant reaction mechanism is coulomb excitation, nearly all of the reactions in the aluminum target were due to nuclear interactions. The use of a variety of targets allowed us to subtract the small nuclear dissociation component from the total reaction cross section measured with the lead target. The result was a pure coulomb cross section.

The use of a variety of targets facilitated a more systematic study of the coulomb acceleration effect. The interactions with the aluminum target, which were largely neutron stripping reactions, were also used to populate and study the neutron unbound ^{10}Li system. Neutron-neutron correlations were also revisited in the current work.

3 The Experiment

3.1 The ^{11}Li Beam

The beam of ^{11}Li particles used in the experiment was produced by projectile fragmentation in the NSCL A1200 Fragment Separator [18]. At the target location of the A1200, a ^{7}Be production target with a thickness of 1.924 g/cm^2 was bombarded with an $^{18}O^{6+}$ beam at 80 MeV/A. The intensity of the primary beam was of the order of $1*10^{11}$ particles/second. ^{11}Li particles emerged from the production target with an average energy of 37.5 MeV/A. The ^{11}Li beam passed through a slit aperture at Image 1, producing a beam profile whose full width in momentum was 3%. At the A1200 Image 2 location, the dispersive image of the beam impinged on a wedge shaped energy degrader. The wedge was made of lucite and the thickness was equivalent in energy loss to a piece of ^{12}C 940 mg/cm^2 thick. The ^{11}Li beam particles emerged from the A1200 with an average energy of 25.3 MeV/A, and these particles were our beam of projectiles.

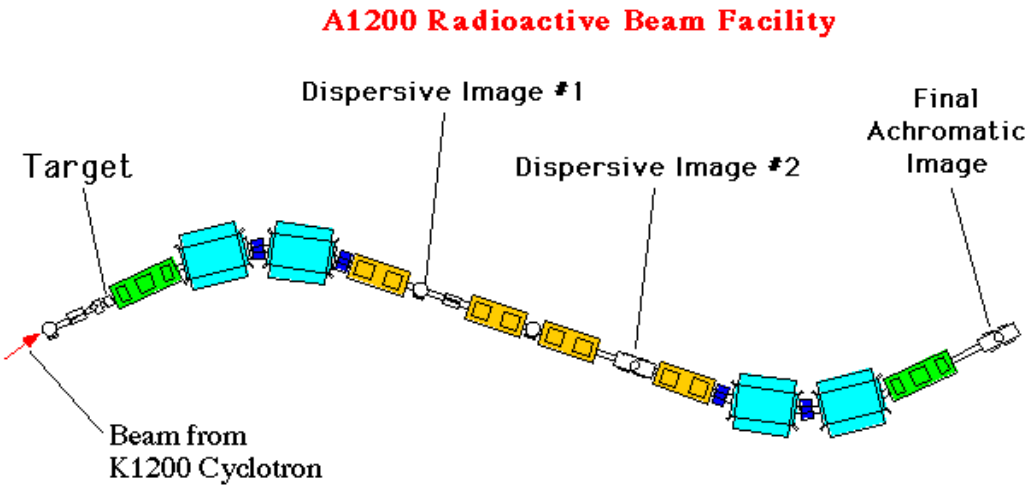

Figure 14 – Schematic of the A1200 Fragment Separator at the NSCL.

The beam energy of 25 MeV/A was chosen for three reasons. The first consideration was that when low energy neutrons are produced in an experiment, the problem of neutron cross-talk is simpler and can be reliably accounted for. Secondly, the

E1 coulomb excitation cross section, the process we set out to study, is inversely proportional to beam energy. Finally, the experiment was run with the Beam Sweeping Dipole, a large aperture, room temperature magnet. A low rigidity ^{11}Li beam maximizes the effectiveness of this device. Many of these considerations would favor an even lower energy ^{11}Li beam, but the beam was produced by projectile fragmentation, and when the secondary beam energy is decreased, the intensity and quality of the beam suffer. As we learned, 25 MeV/A is close to the lower practical limit in ^{11}Li beam energy when produced by particle fragmentation.

Initially, the beam intensity on target in the N4 vault was as low as 50 particles/second. In an attempt to increase the secondary beam intensity, the degrader wedge was removed from Image 2, and placed in front of the last beam-line dipole magnet before the N4 vault. This method of transporting a higher energy secondary beam was used by Sackett *et al*. in a 1991 measurement of ^{11}Li dissociation, but showed no substantial gain over the conventional production and delivery technique. Eventually, the wedge was replaced at Image 2, and the quadrupole magnets of the A1200 were adjusted, more closely matching the dispersion of the spectrometer to the material angle of the thick degrader wedge. This arrangement eventually yielded a secondary beam intensity as high as 500 ^{11}Li particles/second on the target in N4. Integrated over the entire run, the average beam rate was 150 ^{11}Li/second on target.

In pushing the ^{11}Li energy as low as 25 MeV/A, the purity of the secondary beam suffered as well. Unfortunately, the majority of the beam particles were actually not ^{11}Li, but ^{15}B at 37.55 MeV/A. Table 1 shows all nuclei present in the secondary beam, with relative intensities and energies.

Beam Particle	Fraction of Total Beam	Energy [MeV/A]
^{15}B	97.10%	37.55
^{11}Li	1.38%	25.3
^{10}Be	0.80%	53.62
^{14}C	0.23%	61.31
^{7}Li	0.18%	61.31
^{6}He	0.14%	37.55
^{8}Li	0.09%	47.28
^{9}Li	0.06%	37.55

Table 1 – Intensities and energies of nuclei in the secondary beam delivered to N4 vault.

Careful attention was paid to the very strong ^{15}B component of the beam, as it was possible for these particles to react in the target, producing a ^{9}Li-2n coincidence of the kind we hoped to measure. Normally, in addition to the momentum slit aperture at Image 1 of the A1200, there is also a thin plastic timing scintillator. Measuring the Time-of-Flight of each beam particle between Image 1 and our detectors in N4 would have allowed a selection of only events in which the beam particle was a ^{11}Li, as this was the only projectile with an energy of 25 MeV/A. However, when the degrader wedge was removed from Image 2 and placed in the beam-line near N4, it was mounted on the TOF scintillator. When the wedge was replaced at Image 2, the timing scintillator was no longer available. Fortunately, because of the neutron halo nature of the ^{11}Li nucleus, the dissociation of ^{11}Li into ^{9}Li is usually due to a peripheral reaction, and produces 9Li fragments with a small spread in energy. The energy of ^{9}Li particles produced by ^{11}Li in the lead target was 21 ± 2 MeV/A. On the other hand, a reaction which produces a lithium fragment from a ^{15}B projectile is, in general, a much more central collision, and produces the fragments with a large spread in energy. The ^{15}B beam particles did, in fact, produce lithium fragments, but they were higher in energy and spread over a larger range in energy, than the ^{9}Li fragments created by reactions of the ^{11}Li beam. The lithium

fragments created by the ^{15}B left the target with an average energy of 33 MeV/A and were predominantly ^{7}Li and ^{8}Li fragments. The ΔE-E plot below shows two distinct groups of lithium fragments that were easily separated for analysis of the ^{11}Li dissociations – ^{9}Li at 21 MeV/A, and ^{7,8}Li at 33 MeV/A. For clarity, fragments in coincidence with two neutrons are shown. A total energy measurement is not available for ^{7,8}Li fragments in the plot, because the scintillators were calibrated to calculate ^{9}Li energies.

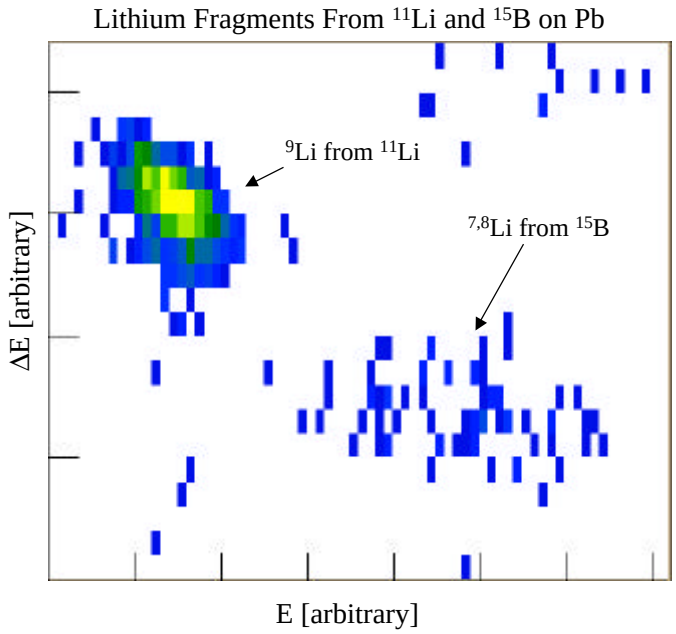

Figure 15 -- DE-E plot showing lithium fragments created by ^{11}Li and ^{15}B beam particles. Fragments shown were detected in coincidence with two neutrons.

3.2 The Detector Setup

A great deal of new equipment was developed for kinematically complete measurements of the dissociation of halo nuclei, such as ^{11}Li. Both the fragment detection system – the Beam Sweeping Dipole, and the Neutron Walls used in this work were developed with this experiment in mind. Below is a schematic of the N4 vault at the NSCL where the studies were performed.

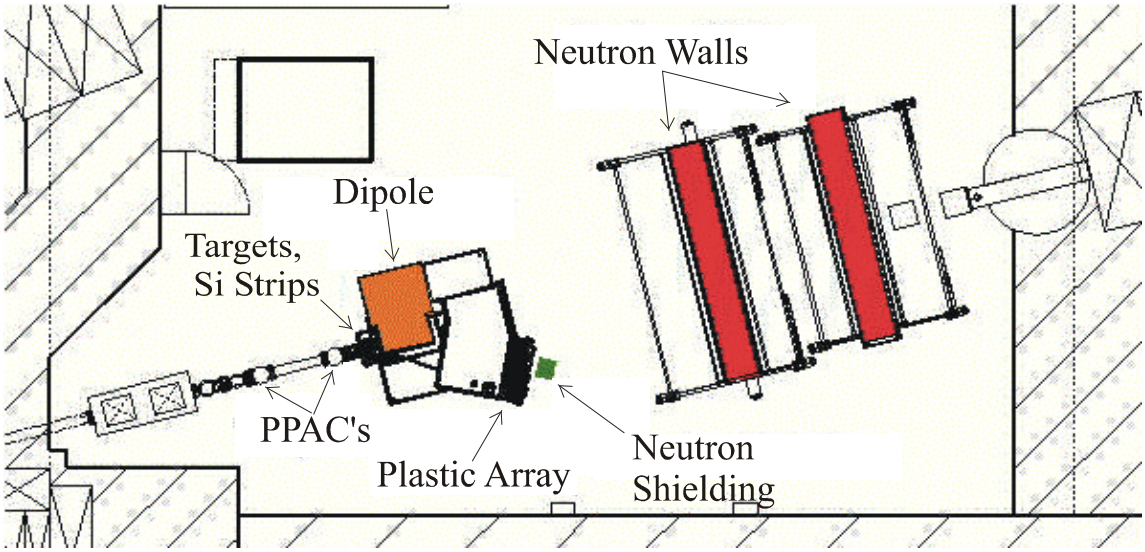

Figure 16 – The layout of the N4 vault, prepared for kinematically complete measurements of halo nuclear dissociation. Charged fragments and unreacted beam particles are swept through the dipole and stopped in the fragment array. Neutrons created in the target are detected by the Neutron Walls. The diagram is not drawn to scale.

3.2.1 Fragment Detectors

The development and operation of the fragment detection system designed for use with the Beam Sweeping Dipole has already been discussed in detail in Section 1, but a few details will be shared here.

As is the nature of most secondary beams, the ^{11}Li beam had a fairly large spot size on the target, and a large emittance. The beam was focused on the target to a size of 2cm x 2cm, and the average angle of beam particles with respect to the beam axis was

greater than 1 degree. In order to determine the direction and point of incidence on the target of each beam particle, a pair of Parallel Plate Avalanche Counters (PPACs) [19] were mounted in the beam line upstream from the target. The PPACs were placed 91.4 cm from each other, with the downstream PPAC 38.6 cm from the target. The charge created in the PPAC's was divided resistively into up, down, left and right signals. From these pulse heights, the particle position in each PPAC was calculated with a resolution of 2 mm, FWHM. Normally these detectors are filled with iso-octane to a pressure of 5 torr and biased to 650 Volts. In this mode, the combined detection efficiency of the two devices was only 60% for ^{11}Li particles. To boost the efficiency of PPAC's in detecting ^{11}Li, ^{8}He, and ^{6}He beam particles, the gas pressure was increased to 7.5 torr and the bias was raised to 775 volts. These measures produced a combined detection efficiency of better than 95% for ^{11}Li particles by the PPACs but also led to breakdown and eventual failure of the detectors. The experiment was paused several times over the course of 10 days of running to replace an expired detector.

Directly behind the target, centered at zero degrees, were a pair of silicon strip detectors purchased from MICRON [ref ft.]. Placed side by side, six inches downstream from the target, the detectors covered an area of 5cm x 10 cm. The readout surface on one side of each detector was divided into 16 horizontal strips, each 3.125 mm wide, while the other side featured 16 vertical strips. The design of opposing segmentation on the detector surfaces essentially divided the detectors into an array of 512, square, (x,y) pixels. The signals from all x and y strips of the detectors were amplified and shaped. During an event readout, only channels with non-zero pulse height were digitized, and the x and y strips with the maximum charge collected defined the fragment's point of interaction in the detector. Generally, more than 99% of the total charge was collected on a single pair of x and y strips. The PPAC detectors were used to calculate each beam particle's point of interaction on the reaction target, and this information, along with an (x,y) measurement from the silicon detectors, was used to measure each fragment's angle

relative to the incoming beam. At 15.24 mm from the target, the 3.125 mm pixels of the silicon detectors subtended an angle of 1.2 degrees.

The detectors were 250 μm thick, and ^{9}Li fragments from the target lost an average of 10.3 MeV in the silicon. This energy loss measurement, together with the total energy measurement made by a scintillator array, was used to isotopically identify fragments and beam particles by the ΔE-E method. In addition to pulse height, a time signal was obtained from the silicon detectors by processing the pre-amp signals with fast amplifiers and constant fraction discriminators. These signals were meant to measure the TOF of fragments from the target to the scintillator array, as well as provide a stop signal for the neutron TOF measurements. Unfortunately, with the Beam Sweeping Dipole power supplies running, the fast signals were prone to noise pick-up problems, and the timing with this system was unstable.

At the exit of the Beam Sweeping Dipole, an array of 16 Bicron BC-408 scintillator bars stopped all fragments and unreacted beam particles. The vertical bars were viewed at each end by a 2" Burle 8575 or similar Hamamatsu photomultiplier tube. Each PMT supplied an anode signal, integrated for pulse height information, and a signal from the eleventh dynode which was processed by a constant fraction discriminator for timing information. The bars were 16" long, and so the signals from both PMT's of each bar were used to correct the pulse height and timing measurements for position dependence along the detector. The scintillation light was transmitted from the point of interaction to each PMT by total internal reflection at the bars' surfaces, but slight losses were expected from exponential attenuation of the light. To negate this effect, the geometric mean of the pulse heights measured by the two phototubes was calculated, producing a position independent energy measurement. To account for a spread in transit time for the light to travel from various locations along the detector to the phototubes, the average of the time signals from the two phototubes was calculated and used as the reference signal for neutron TOF measurements.

3.2.2 The Neutron Walls

Neutrons created in the dissociation events were detected by the NSCL Neutron Wall arrays [20]. Developed for this experiment, the Neutron Walls are a pair of 2m x 2m liquid scintillator neutron detectors. Each Wall is a stack of 25 custom-made glass cells, 2m long, with a 6.25x8.26 cm^2 inner rectangular cross section. The cells are filled with NE America's NE 213, a liquid scintillator with pulse-shape discrimination capabilities. Each end of every cell is read out with a Philips 12 stage, 3-inch photomultiplier tube. Each phototube supplies an anode signal, which is used for pulse height information, and the signal from the last dynode is inverted and processed by a constant fraction discriminator for timing measurements. The cells are mounted inside an aluminum frame, and each array is covered front and back with a 1/32" aluminum skin to make the entire array light tight. A schematic of one Neutron Wall is shown in Figure 17, with a portion of the aluminum skin cut away.

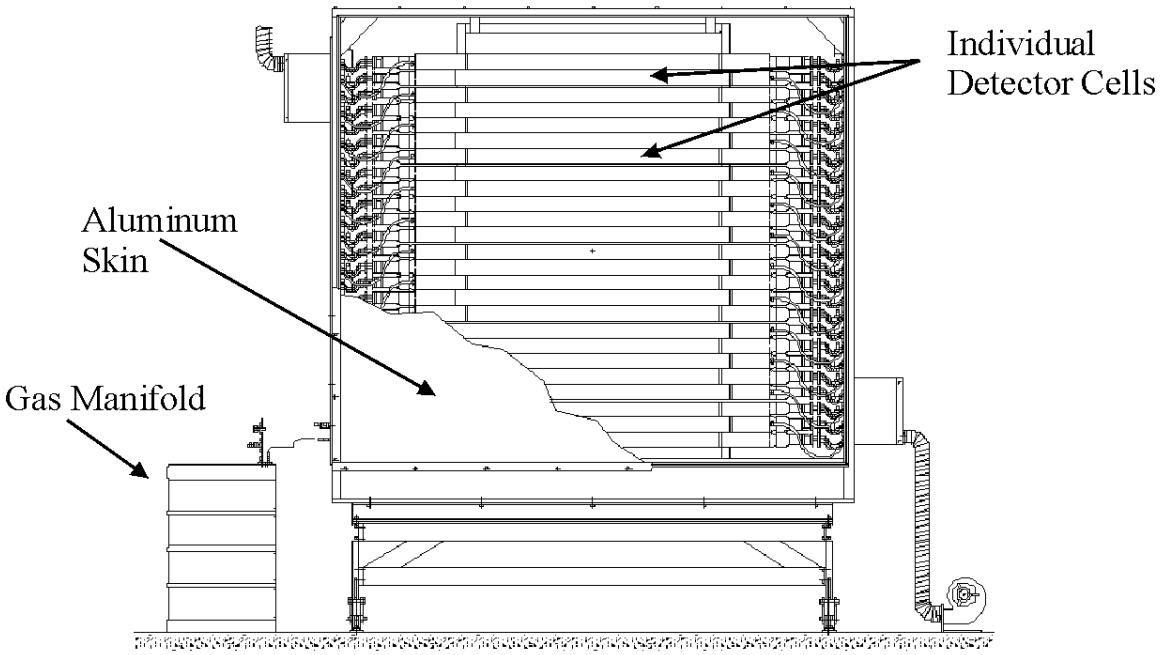

Figure 17 – Schematic of one of the Neutron Walls. In this view, the light tight aluminum skin which covers the array is cut away, revealing the 25 horizontal cells of scintillator inside. The volume of each cell is coupled to a large argon gas manifold to allow for thermal expansion of the liquid inside the glass.

Neutrons are detected primarily by n,p elastic scattering in the scintillator. The recoil protons excite the liquid, creating scintillation light. The amount of light created is not simply related to the incident neutron's kinetic energy, but also to the scattering angle between the neutron and proton. For this reason, the neutrons' energies are measured by Time-of-Flight (TOF) rather than scintillation pulse height.

When a neutron interacts in a Neutron Wall cell, some of the scintillation light travels down the cell in either direction, eventually striking the phototube at each end. To compensate for the transit time of the light travelling through the cell, the mean of the two time signals from each of the cell's phototubes is calculated. Because the total amount of time required for light to travel the entire length of a cell is constant, the mean

of the two signals provides a position independent determination of a neutron's arrival time at the Wall.

The transit time of the scintillation light travelling through a cell is exploited in determining the x-position along a cell where a neutron interacted. A scintillation event in the exact center of a cell would result in the simultaneous arrival of light at each of the cell's two phototubes. Therefore, calculating the difference in arrival time of the light between two phototubes yields a measurement of the distance between the neutron's point of interaction and the center of the cell. The timing resolution of the Neutron Walls improves with increasing pulse height. In an event which produces the same amount of scintillation light as a 4 MeV electron (defined as 4 MeVee), the timing resolution of the device enables a position measurement with a Gaussian sigma of 3 cm. An event which produces only 1 MeVee of light is measured with a sigma of 6 cm. Since the Walls are vertical stacks of discrete detector cells, each 8.26 cm high, identification of which cell fires yields a trivial measurement of the vertical y-position on the Wall where the neutron interacted. The resolution is simply equivalent to the vertical size of the liquid in the cell, 7.62 cm.

Proton recoil scintillation detectors are sensitive to types of radiation besides neutrons. Typically, a large background of γ-rays is present during an experiment. Also, because of their large surface area, the Neutron Walls detect a high number of cosmic rays. Various methods are used to eliminate γ-rays and cosmic rays from neutron data, such as raising the threshold level of the detector. Most γ-rays come from nuclear transitions, so their energies are limited to a typical binding energy, about 8 MeV. Unfortunately, increasing the threshold of the detector impairs its neutron detection efficiency.

The method of background reduction used with the Neutron Walls is known as pulse-shape discrimination. In some scintillators, such as the liquid NE 213, the shape of the scintillation light pulse varies for different types of ionizing radiation. The light has

two components, a prompt and a delayed fluorescence. The prompt fluorescence has a decay constant of a few nanoseconds, while the delayed light has a decay constant on the order of a few hundred nanoseconds. The proportion of light produced by each of these two components varies according to the specific ionization of the ionizing particle. A lightly ionizing particle, such as a cosmic ray or an electron from the compton scattering of a γ-ray, will produce most of its light in prompt fluorescence. A highly ionizing particle, such as a recoil proton, will produce a larger fraction of light in the delayed fluorescence for the same amount of total fluorescence as a lightly ionizing particle. To take advantage of this property of the scintillator, we use a technique which compares the size of the 'head', or first 30 ns of the pulse, to the total pulse height.

A circuit was developed at the NSCL that receives the anode signal from a Neutron Wall phototube. One output of the circuit is simply proportional to the input pulse; it is called QTOTAL. Another channel of the circuit uses the reflection at the end of a clipped delay line to produce a signal that is proportional in size to the 'head' of the input. It is called QFAST. Both signals are integrated by charge-to-digital converters (QDC's), and when plotted against each other, the events fall into one of two regions on the graph. One streak across the plot is formed by γ-ray and cosmic ray events, while below it is the collection of events caused by neutrons. A sample plot illustrating this technique is shown below. The data were taken with a PuBe neutron and γ-ray source.

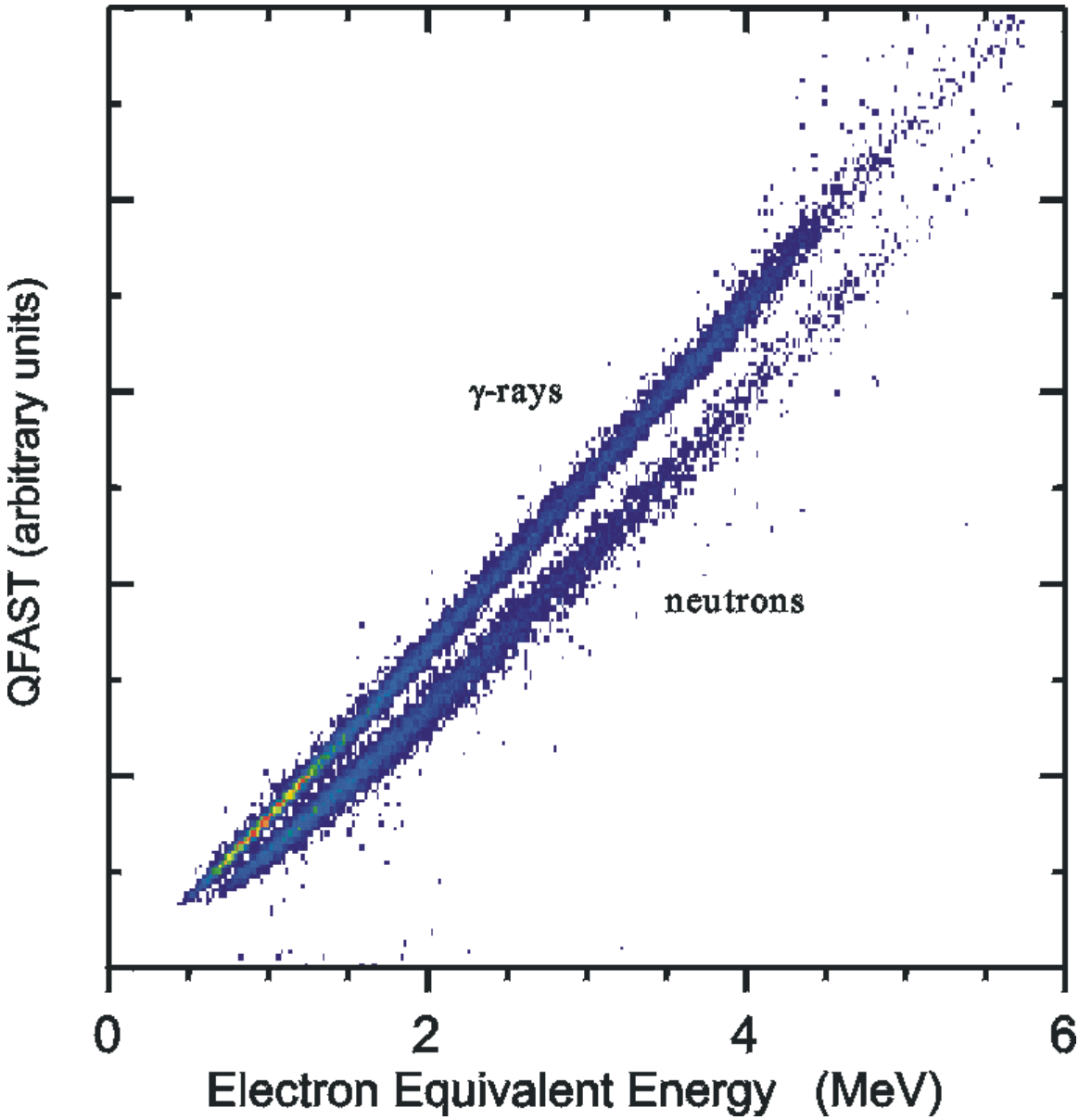

Figure 18 – A PSD spectrum from a cell in the Neutron Wall Array. The cell was illuminated with neutrons and g-rays from a PuBe source.

Both phototubes of the Neutron Wall cell were used in producing the PSD spectrum in Figure 18. Because of the 2 m length of the Neutron Wall cells, attenuation of scintillation light by the liquid is an important effect. However, if the only losses are due to exponential attenuation, the geometric mean of the pulse heights arriving at each

end is independent of the x-position of the source of the light. To ensure the quality of the pulse-shape discrimination method for events over the entire area of the Walls, the geometric mean of both the QFAST and QTOTAL signals from the two phototubes is calculated and used to select either neutron or γ-ray events.

In addition to the QFAST and QTOTAL outputs, the NSCL pulse-shape discrimination circuits also supply a 'head' and 'total' signal which are attenuated by a factor of four. Neutron events in the Walls produce light pulses over a very large dynamic range. If the gain of the phototubes is set high enough that we achieve good discrimination for low pulse height events, the events with large pulses will saturate the QDC modules. Our data analysis software selects neutrons by first comparing the QFAST and QTOTAL signals in a plot like the one shown in Figure 18. If the size of QTOTAL is below the saturation level, the QFAST/QTOTAL comparison is used to determine whether a neutron caused the event. If QTOTAL is saturated, the attenuated signals, QFASTATT and QTOTALATT are used to determine the nature of the event.

An intrinsic property of a neutron detector is its time resolution for a given pulse height. Because of this, a long flight path from target to detector is desirable to maximize the resolution of neutron energy measurements. However, such improvements in the measurement's energy resolution are paid for in lost acceptance, as the detector subtends a smaller solid angle when it is moved farther from the target.

An optimization between resolution and acceptance was made in placing the first of the two Neutron Walls five meters from the target, centered at zero degrees. For a light pulse of the size made by a 1 MeV electron (1 MeVee), the time resolution of the Neutron Wall (σ_t) is 0.8 ns. Events which generate 4 MeVee of light are measured with a timing resolution of 0.4 ns. [21] With these timing characteristics and detectors with a thickness of 6.25 cm, a flight path of 5 meters corresponds to a neutron energy resolution of about 3% when measuring 25 MeV neutrons. Although the Neutron Walls are 2 m high, the vertical aperture defined by the vacuum chamber of the Beam Sweeping Dipole

did not allow neutrons created in the target to see the entire array. Horizontally, the full 2 m length of the cells was accessible to target neutrons, but vertically, the poles of the magnet defined an aperture which only illuminated 1 m of the front Wall with target neutrons. For this reason, only 16 of the 25 cells in each Wall were used in the experiment. In this configuration, the acceptance of the front Neutron Wall was 100% for neutrons ejected at angles up to 5.7 degrees in the lab frame, and 0% for neutrons at angles greater than 12.6 degrees.

The second Neutron Wall was also centered at zero degrees, 84 cm farther from the target than the first Wall. There are two advantages to placing one array directly behind the other. The first is that the thickness of scintillator material seen by incident neutrons is doubled, almost doubling our detection efficiency. The scintillator volume of one Wall is only 6.35 cm thick, which corresponds to an intrinsic neutron detection efficiency (ε_1) of only 11% for 25 MeV neutrons, assuming zero pulse height threshold, and that the neutrons' only mode of interaction in the walls is n,p scattering. That is, when 25 MeV neutrons travel through one Wall, they are detected 11% of the time. Dissociation studies of nuclei such as ^{6}He and ^{11}Li require the detection of two neutrons in coincidence, and the intrinsic efficiency for detecting both coincident neutrons (ε_2) goes like $(\varepsilon_1)^2$ or 1.2%. The efficiency could have been enhanced simply by making one Wall thicker, but since we do not know the depth in the detector where the neutron interacted, an increased thickness would add uncertainty to the length of the neutron's flight path, impairing our energy resolution. The configuration of two sequential detectors enhances intrinsic efficiency without sacrificing resolution. The other advantage of placing one detector behind the other is that we gain the ability to detect coincident neutrons with very small relative momenta. Many models of halo nuclei predict that the two neutrons liberated in a break-up event may leave the target with a very small relative angle. If the relative angle is small enough, both neutrons will interact in the same detector cell, and in our detection scheme, will look like an event created by a

single neutron. By placing one detector behind the other, we gave ourselves the opportunity of detecting two neutrons with zero relative momenta, measuring one of them in the front Wall and the other in the back Wall. While an arrangement of one Neutron Wall placed behind the other enhanced our efficiency, it exacerbated the problem of cross talk.

Cross talk is a familiar problem of one neutron creating signals in two separate detectors. Although neutrons are detected primarily through n,p elastic scattering, the neutrons may induce several other reactions in the scintillator. The liquid is entirely hydrogen and carbon, and the table below lists several of the most likely interactions for neutrons in the detector.

1. $n + p \rightarrow n + p$
2. $n + C \rightarrow n + C$
3. $n + C \rightarrow n' + C + \gamma$ - 4.44 MeV
4. $n + C \rightarrow He + Be$ - 5.71 MeV
5. $n + C \rightarrow n' + 3He$ – 7.26 MeV
6. $n + C \rightarrow p + B$ - 12.59 MeV

Table 2 – Catalog of predominant interactions for a neutron in NE-213 liquid scintillator.

Although any of the reactions above are possible, the first one, n,p elastic scattering, has the highest cross section for 25 MeV neutrons. Elastic scattering from hydrogen also produces the biggest pulses in the scintillator. Alpha particles are too densely ionizing to produce a light pulse above a threshold of a few MeVee. The high cross section and the large pulses make n,p acattering the dominant mode of detection for neutrons of energy $\leq$ 25 MeV. Compared to interactions 3 and 5 in Table 2, cross-talk from n,p scattering can be identified from its simple kinematics. Figure 19 shows a typical example of a cross talk event. In this case, a single neutron scatters from a proton in the first wall, making a signal. The neutron has not lost all of its energy, however, and it recoils into the second wall, scattering again and making a second signal. Each two-

neutron event must be analyzed to distinguish true two-neutron coincidences from cross talk.

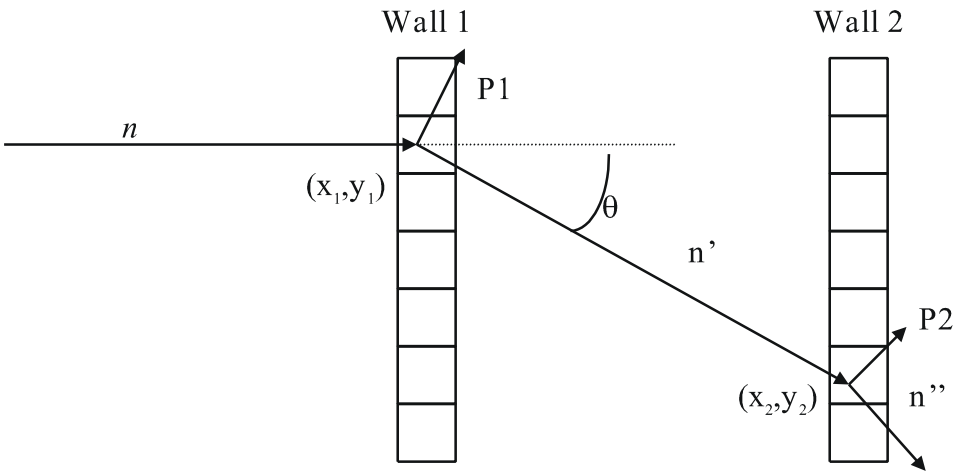

Figure 19 – An example of a cross-talk event between the two Neutron Walls. The neutron scatters off a proton in Wall 1, producing a detectable signal. The recoiling neutron then enters a cell in Wall 2, scattering again and producing a second signal.

The simple kinematics of n,p scattering provide three criteria for identifying cross-talk.

1. The pulse height of the signal in the first cell gives the kinetic energy of the first recoil proton E_{P1}. The energy of the proton defines the scattering angle q of the outgoing neutron. If the scattering angle corresponds to the location of the second pulse, then the event may be cross talk.
2. If the scattered neutron's energy $E_{n'}$, as implied by E_{P1}, corresponds with the energy as determined by the time-of-flight between the two cells, then the event may be cross talk.
3. If the second recoil proton's energy E_{P2} is not greater than the scattered neutron's energy E_n, then the event may be cross talk.

If an event in which one neutron is detected in each wall satisfies all three criteria, it could be cross talk and is rejected. Cross talk also occurs between cells in the same wall, often between neighboring cells. Because of the high uncertainty in calculating q for events in nearby cells, criterion 1 is not used in the analysis of neutron-neutron coincidences detected within one wall. If a single wall detects two neutrons, and the event satisfies criteria 2 and 3, it could be cross talk and is rejected. Monte Carlo simulations of this technique show that our method allows rejection of 80% of x-talk events, while preserving 75% of the true 2-n events [22]

4 Analysis

4.1 Fragment Singles – s_{2n}

Three types of detection events were written to tape during the ^{11}Li experiment. Obviously, coincidence events in which both the fragment detectors and the Neutron Walls registered hits were recorded. In addition to the coincidence data set, both Neutron Wall and fragment detector singles events were recorded. The Neutron Wall singles events were used off-line for analysis of the array, while the fragment singles data provided a measurement of the two-neutron removal cross section. Because of their high counting rates relative to the coincidence rate, both singles event triggers were downscaled so all three event types made approximately equal contributions to the total event rate. Neutron Wall singles were downscaled by a factor of 999, while one in every 500 fragment singles was recorded. The remaining singles hits were subject to a fast clear, and the system was reset for the next event.

In principle, the fragment singles events would have provided for a trivial determination of the two neutron removal cross section, σ_{2n}. The fragment detectors stopped and counted all ^{9}Li fragments created in the target, as well as all unreacted ^{11}Li beam particles. However, the rate of dissociation in the target was difficult to determine from an analysis of the fragment singles alone.

The fragment detection system was designed to identify particles by the ΔE-E method, but for discrimination between ^{9}Li fragments and unreacted ^{11}Li beam, the energy half of the measurement was the only portion that was used. Because the ^{11}Li dissociated with little decay energy relative to the beam velocity, the ^{9}Li fragments left the target with the same energy per nucleon as the ^{11}Li beam. The energy loss half of the ΔE-E measurement was made by the thin silicon array directly behind the target. For small energy losses, energy deposition by a fragment of charge Z, mass A and energy E is described by:

$$dE \propto Z^2 / (E/A)$$

The ^{9}Li fragments and ^{11}Li beam had the same charge, and struck the silicon detector with the same energy per nucleon, so the only way to discriminate between them was by the total energy deposited in the scintillator array.

The first eight of the fragment scintillator bars were used in the analysis of the ^{11}Li experiment. While the majority of the ^{9}Li fragments were detected by bars 5 through 8, the fragments were emitted over a range of angles, and so a significant number also struck bars 1 through 4. Detectors 1 through 6 also stopped the unreacted ^{11}Li beam, with the majority of the particles finding bars 3, 4, and 5. Because of the small dissociation rate in the targets, the vast majority of the fragment singles data were unreacted ^{11}Li. A number of the ^{11}Li particles reacted in the plastic array, liberating two neutrons. The neutrons created in the detectors left the plastic array, carrying off a portion of the incident ^{11}Li's energy, and so the pulse height recorded for such an event was lower than for a ^{11}Li that stopped without dissociating. Reactions in the plastic created a tail on the ^{11}Li energy peak, and because of the small number of ^{9}Li created in the target, this tail dominated the ^{9}Li counts on bars that stopped most of the ^{11}Li beam.

This source of ambiguity was removed, however, in analysis of fragment – neutron coincidences. Because the Beam Sweeping Dipole deflected the unreacted ^{11}Li through an angle before they struck the plastic array, neutrons created by reactions in the scintillators could be shielded from the Neutron Walls. If the shielding had been 100% effective at absorbing neutrons from the plastic array, the coincidence data set would have included only neutrons and ^{9}Li fragments created in either the target or silicon detectors. The number of events originating from the silicon was small relative to the contribution from the target, but these events could not be eliminated though use of the magnet.

Unfortunately, the shielding behind the scintillator bars did not completely absorb the neutron flux created by ^{11}Li reactions in the array. The energy spectra measured in the bars for ^{9}Li – one-neutron coincidences still show contamination from dissociations in

the detectors. However, the shield was effective enough to prevent detection of two-neutron coincidences resulting from ^{11}Li reacting in the scintillators. Although far fewer two-neutron – Li coincidence events were detected than one-neutron – fragment coincidences, we can be certain that all of the two-neutron events were the result of a reaction in either the target or the silicon detector. These events were the key to our analysis of the fragment singles data, and calculation of σ_{2n}.

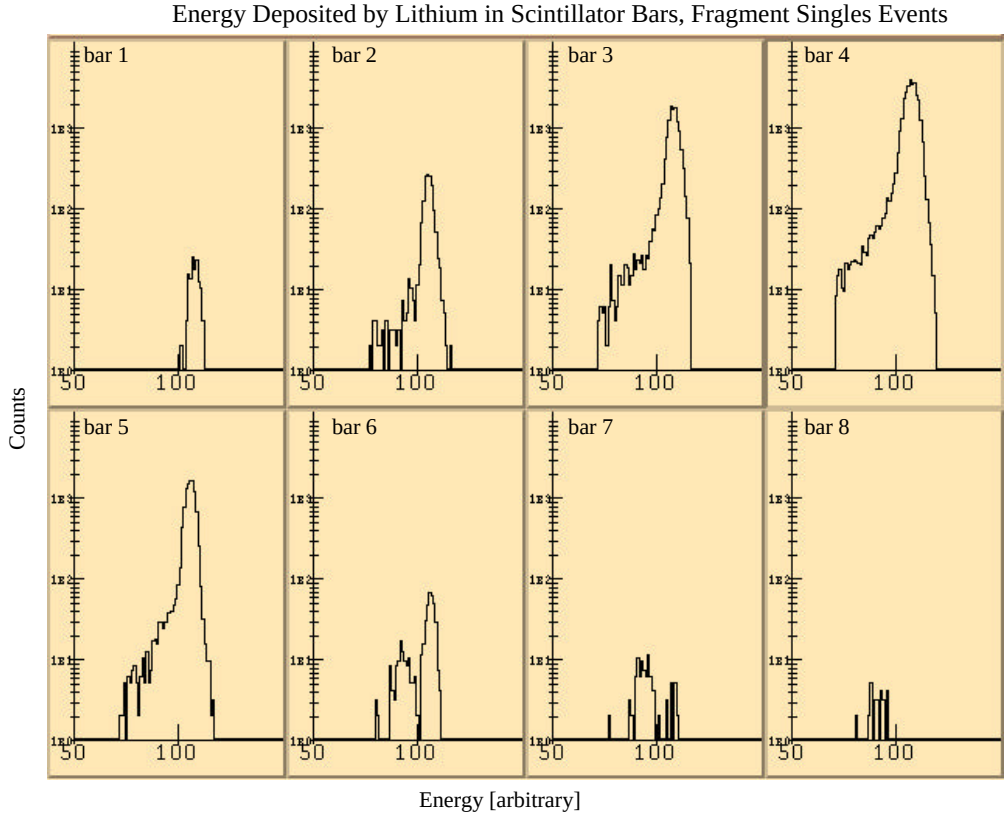

Figure 20 – Energy signals for lithium particles in each of the eight scintillator bars used in the ^{11}Li experiment. Dissociation of ^{11}Li nuclei in the detectors created low energy tails on the ^{11}Li peaks, which dominated the counts due to ^{9}Li fragments created in the target. Bars 6, 7, and 8, which stopped very few ^{11}Li particles, show clear discrimination between target ^{9}Li fragments and unreacted ^{11}Li.

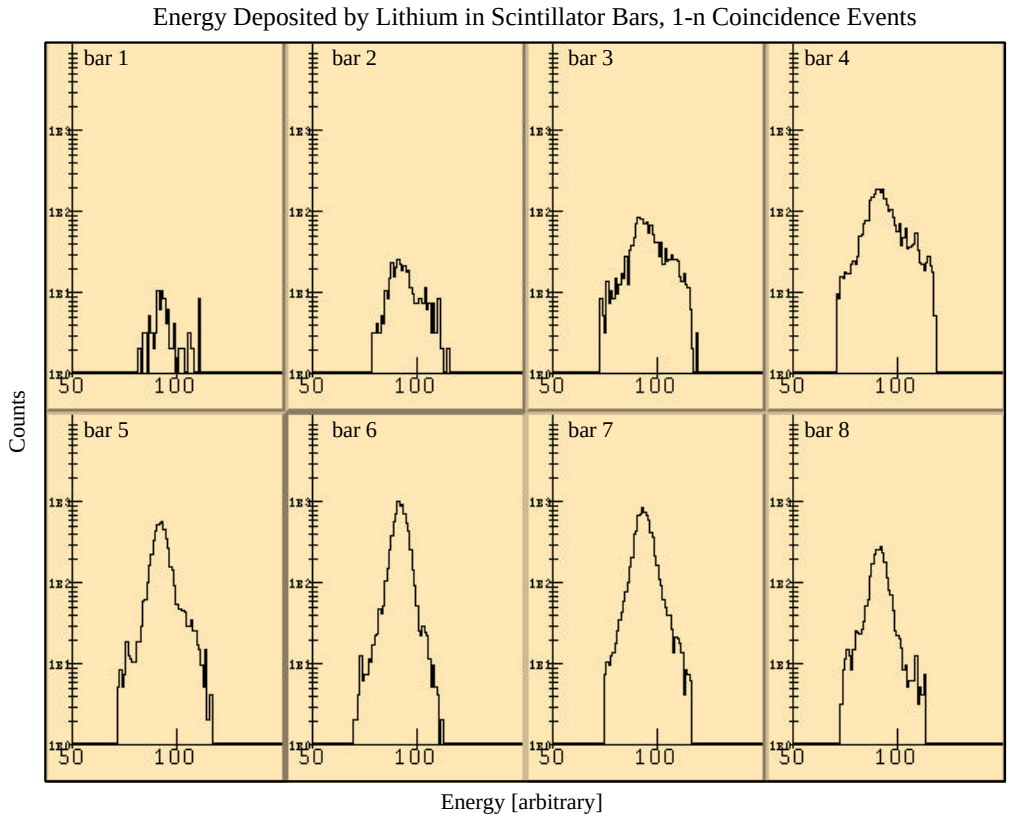

Figure 21 – Energy signals for created in each of the eight plastic bars by lithium particles which were detected in coincidence with a single neutron. Requiring a neutron coincidence reduces the number of ^{11}Li counts in the spectra, but they are not entirely eliminated from the data set.

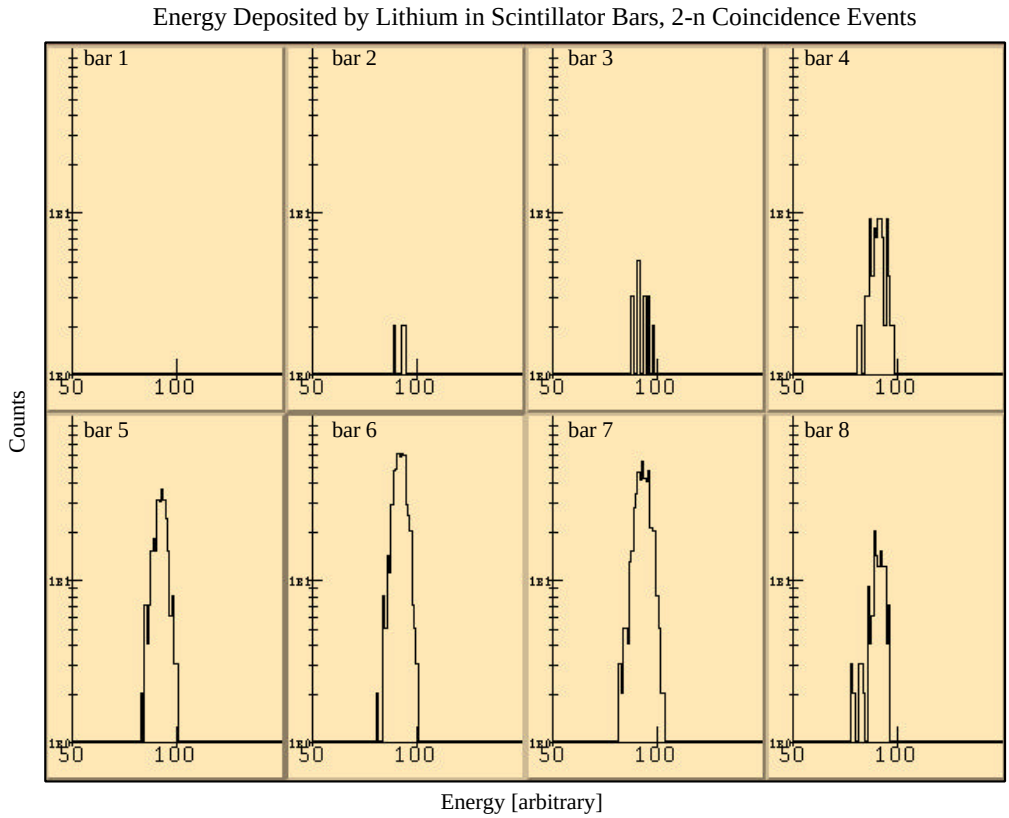

Figure 22 – Energy signals for lithium nuclei detected in coincidence with two neutrons in the Neutron Walls. Only ^{9}Li fragments created in the target or silicon detectors are seen in the spectra.

Figures 20 through 22 show the energy spectra recorded in the eight individual scintillator bars for fragment singles, 1-n coincidence events, and 2-n coincidences. Because of a low reaction rate in the target and beam dissociation in the detectors, the number of ^{9}Li fragments incident on bars 2 through 5 could not be determined for fragment singles events. Analyzing one-neutron coincidence events, however, favored the selection of ^{9}Li fragments which were created in the target or the silicon detectors, as the neutrons which were produced in coincidence with these fragments were directed towards the Neutron Walls. There were still a significant number of ^{11}Li particles in this data set, however, because the shielding behind the plastic detectors did not absorb 100% of the neutrons created in the array. The set of 2-neutron coincidences, however, were composed entirely of ^{9}Li fragments made in either the target or silicon. In an attempt to determine the number of ^{9}Li fragments present in the singles data set, an assumption was made that the relative distribution of ^{9}Lis across the scintillator array was the same, regardless of the number of neutrons detected in coincidence with the fragments. That is, the fraction of ^{9}Li fragments detected by a single scintillator bar in the singles data set was the same fraction of those detected in coincidence with one neutron and also in coincidence with two neutrons.

Very little unreacted ^{11}Li beam struck bars 6, 7, and 8, and so the target ^{9}Li fragments could be counted on those bars in the fragment singles data set. Because of the effect of the Sweeping Magnet, the number of ^{9}Li fragments could be determined for all bars in the 2-neutron coincidence data set. Since the distribution of fragments across the bars was the same for singles, 1-neutron, and 2-neutron coincidences, the 2-neutron coincidences could be used to determine the number of ^{9}Li fragment singles striking bars 1 through 5. The number of ^{9}Li fragment singles detected by bars 6, 7, and 8 were counted for a given target, and the number of ^{9}Li -- 2-neutron coincidences was determined for each of the eight bars. A ratio of the number of singles to 2-neutron events was calculated and used to extrapolate the number of ^{9}Li singles which were

present on bars 1 through 5. The number of ^{9}Li fragments detected by each bar is shown below, for 2-neutron coincidences as well as the extrapolated number for fragment singles. With this determination of the number of ^{9}Li singles, a preliminary σ_{2n} could be calculated for each target.

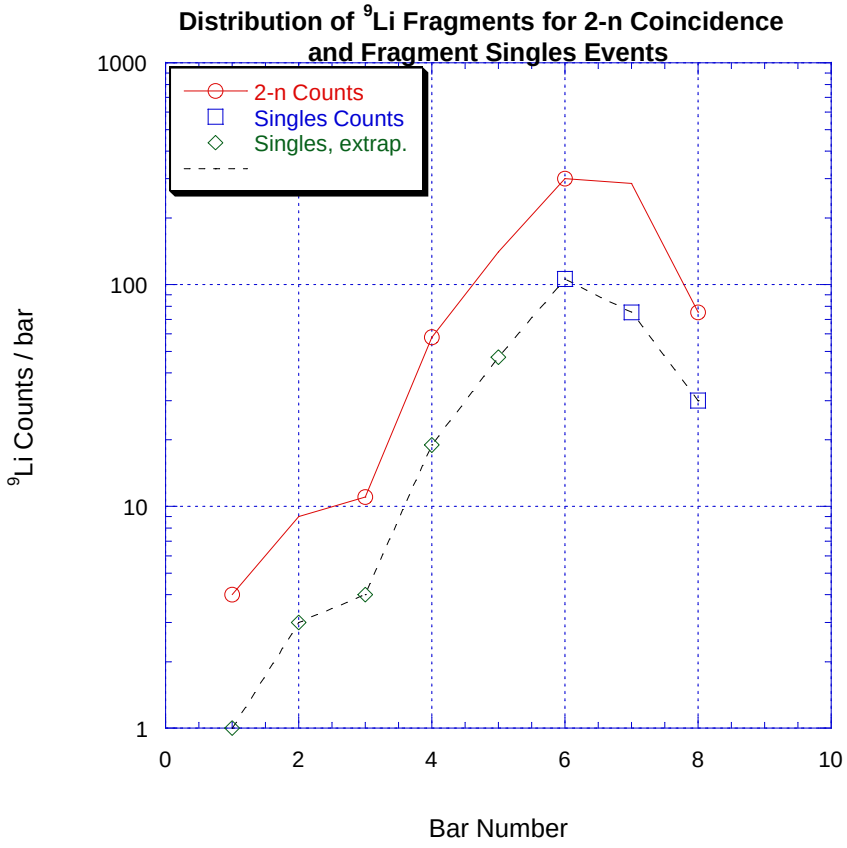

Figure 23 – Distribution of ^{9}Li fragments across the scintillator array, used to determine σ_{2n}.

Two corrections remained to be made to these measurements of σ_{2n}. The first was that the cross sections were determined by comparing the number of ^{9}Li fragment singles to the number of unreacted ^{11}Li particles in the singles data set. This experiment was designed, however, to detect fragments in coincidence with neutrons, and the coincidence and singles data sets were mutually exclusive. Therefore, the number of ^{9}Li singles had to be adjusted by the rate at which neutrons were detected, removing those events from the singles data set. For each target, the number of coincidence events was tallied, and then divided by 500. Every coincidence event in the experiment was recorded, but recall that the fragment singles events were downscaled by a factor of 500. This 'downscaled' coincidence event total was added to the number of ^{9}Li singles, and an adjusted σ_{2n} was calculated.

The other correction made to σ_{2n} was to calculate and subtract out the effect of the silicon detectors. The standard means of performing such a correction is to remove the target and simply count the number of reactions caused by the detectors alone. This reaction rate is then scaled by the number of incident beam particles and subtracted from the total observed with the target in place. A so-called blank run was measured in the 11Li experiment, but the silicon detectors were only 58 mg/cm^2 thick, and the dissociation rate was very small. The statistical uncertainty of a correction based on the blank measurement would have been quite high. Fortunately, one of the three targets used in the experiment was aluminum. The aluminum target nuclei and silicon detector nuclei differ only by one proton, and so the reaction cross section due to either should be very similar. If we assume that the reactions are peripheral and the cross section scales with $A^{1/3}$ of the target, then the cross sections on silicon and aluminum will differ by only 1%, a difference smaller than our statistical errors. With the 240 mg/cm^2 aluminum target in place, we measured dissociations occurring in both the target and the silicon detector. The cross section per target atom was determined for the target/detector system, and multiplied by the number of silicon atoms/cm^2 to calculate the reaction rate in the

silicon. The σ_{2n} for the aluminum target alone could then be determined. The contribution from the silicon detectors to observed reaction rate with the tin and lead targets was calculated and subtracted. The corrected cross-sections are tabulated in Table 3 for the three targets.

Target	σ_{2n}
Pb	5.0 ± 0.4 b
Sn	2.2 ± 0.4 b
Al	0.7 ± 0.1 b

Table 3 – Two neutron removal cross sections for three targets, determined from fragment singles data.

4.2 Momentum Distributions

Because of the very small binding energies of halo nuclei, and consequently their large interaction cross sections, dissociation studies have been a popular experimental method for probing the structure of these nuclei. Specifically, many experiments have measured the momentum distributions of both the halo neutrons and the charged cores following dissociation. [8,23,24,25] Early studies of ^{11}Li found target independence (and therefore reaction mechanism independence) of both neutron angular distributions [26] and ^{9}Li longitudinal momentum distributions. [25] These results were interpreted as evidence that the momentum distributions were direct measurements of the intrinsic momenta of the halo neutrons and core in the ground state of ^{11}Li. Appealing for its simplicity, a common interpretation of such a measurement is that the ground state momentum distributions of the core and halo neutrons can be Fourier transformed into coordinate space, yielding the ground state wave functions for the particles. A subsequent theoretical study of neutron momentum distributions by F. Barranco [27] has shown that while longitudinal momentum distributions are indeed unaffected by varying reaction mechanism, the neutron and fragment transverse distributions will depend highly on the type of reaction which caused the breakup. In this study, Barranco found that the previously observed target independence on neutron momentum distributions was a coincidence arising from relative contribution of various reaction mechanisms.

In the current work, both longitudinal and transverse momentum distributions were extracted for the neutrons and ^{9}Li cores, dissociated on targets of aluminum, tin, and lead. In addition, the complete kinematics of the measurements allowed us to calculate each particle's momentum in the ^{11}Li rest frame.

4.2.1 Fragment and Neutron Longitudinal Momenta

As stated above, early experimental work and subsequent theoretical studies of ^{11}Li have shown that both fragment and neutron longitudinal momentum distributions are somewhat unaffected by effects of the reaction mechanism which produced the free particles. Accordingly, the widths of the momentum distributions measured in this work are independent of target. Both neutron and fragment distributions are well fitted with Gaussian parameterizations. The fragment distributions show asymetric tails due to known detector effects, and this portion of the curve was not included in the fit. In addition to the intrinsic momenta of the neutrons and fragments, the measured distributions include contributions from detector resolutions and from spread in incident beam energy. The distributions are also broadened by the finite target thickness, as we cannot know exactly where in the target, and therefore at exactly what energy, the dissociation took place. The magnitude of this effect on the momentum distributions is easily calculated, and the beam profiles and detector resolutions are determined from analysis of blank runs with no target. The measured distributions were fitted with Gaussians, and then the broadening contributions mentioned above were unfolded from the curves with the aid of a Monte Carlo simulation. The widths of the intrinsic longitudinal momentum distributions, unfolded from the measured spectra, are tabulated in Table 4.

Target	9Li P σ [MeV/c]	n P σ [MeV/c]
Al	24.4 ± 0.8	12.7 ± 0.6
Sn	22.0 ± 1.0	11.6 ± 0.8
Pb	23.6 ± 0.5	11.5 ± 0.5

Table 4 – Widths of longitudinal momentum distributions of both 9Li and neutrons measured in the dissociation of ^{11}Li on three targets. The widths given are the sigmas of Gaussian distributions, and have been unfolded from the measured distributions which include contributions from experimental effects.

The raw spectra measured for both neutrons and fragments are shown in Figure 24 and Figure 25, before the intrinsic momenta are extracted.

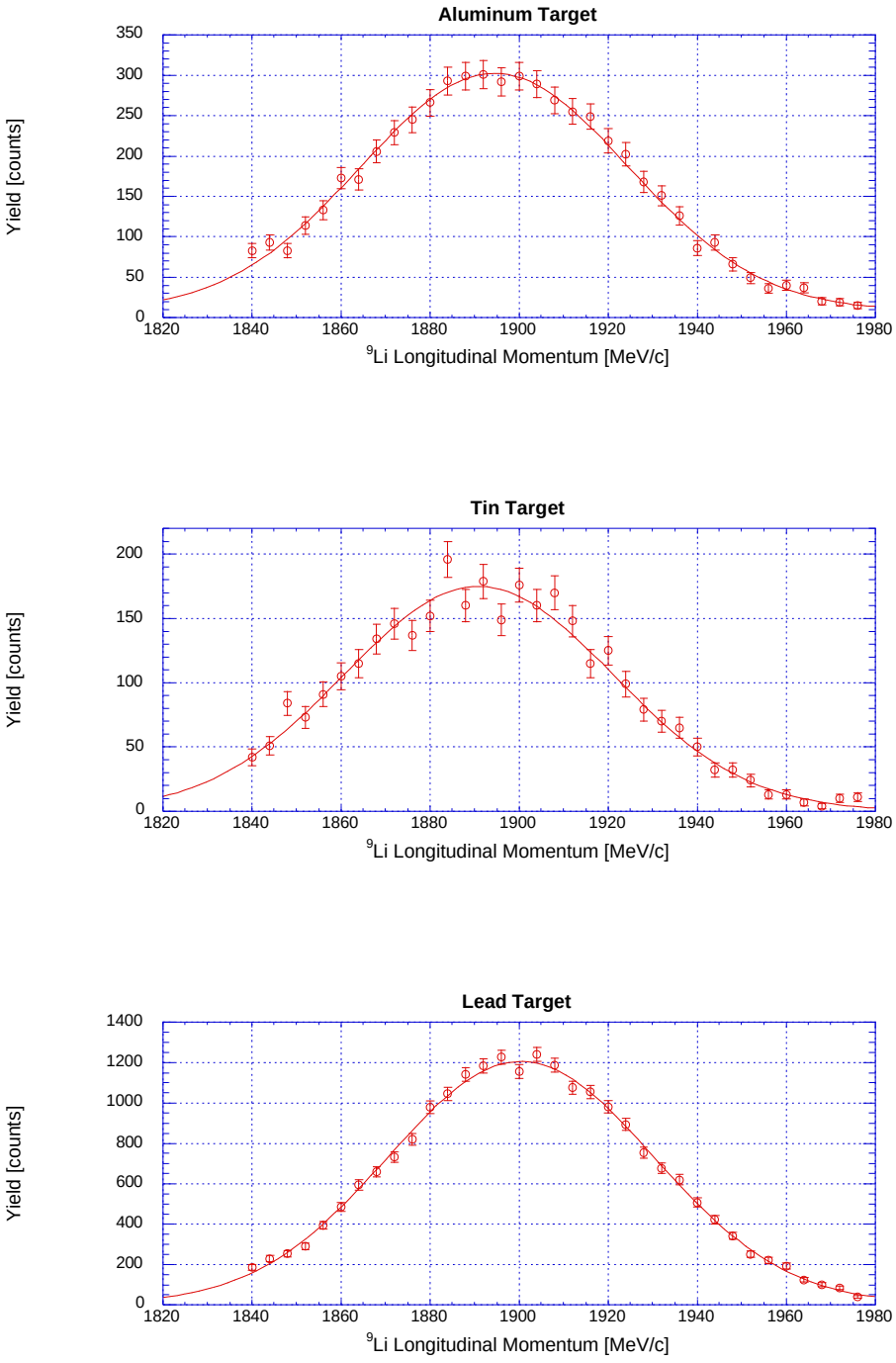

Figure 24 – Longitudinal momentum distributions of ^{9}Li fragments measured from breakup of ^{11}Li on three targets. The lines are Gaussian curve fits, which were used to extract the intrinsic 9Li momenta from experimental effects.

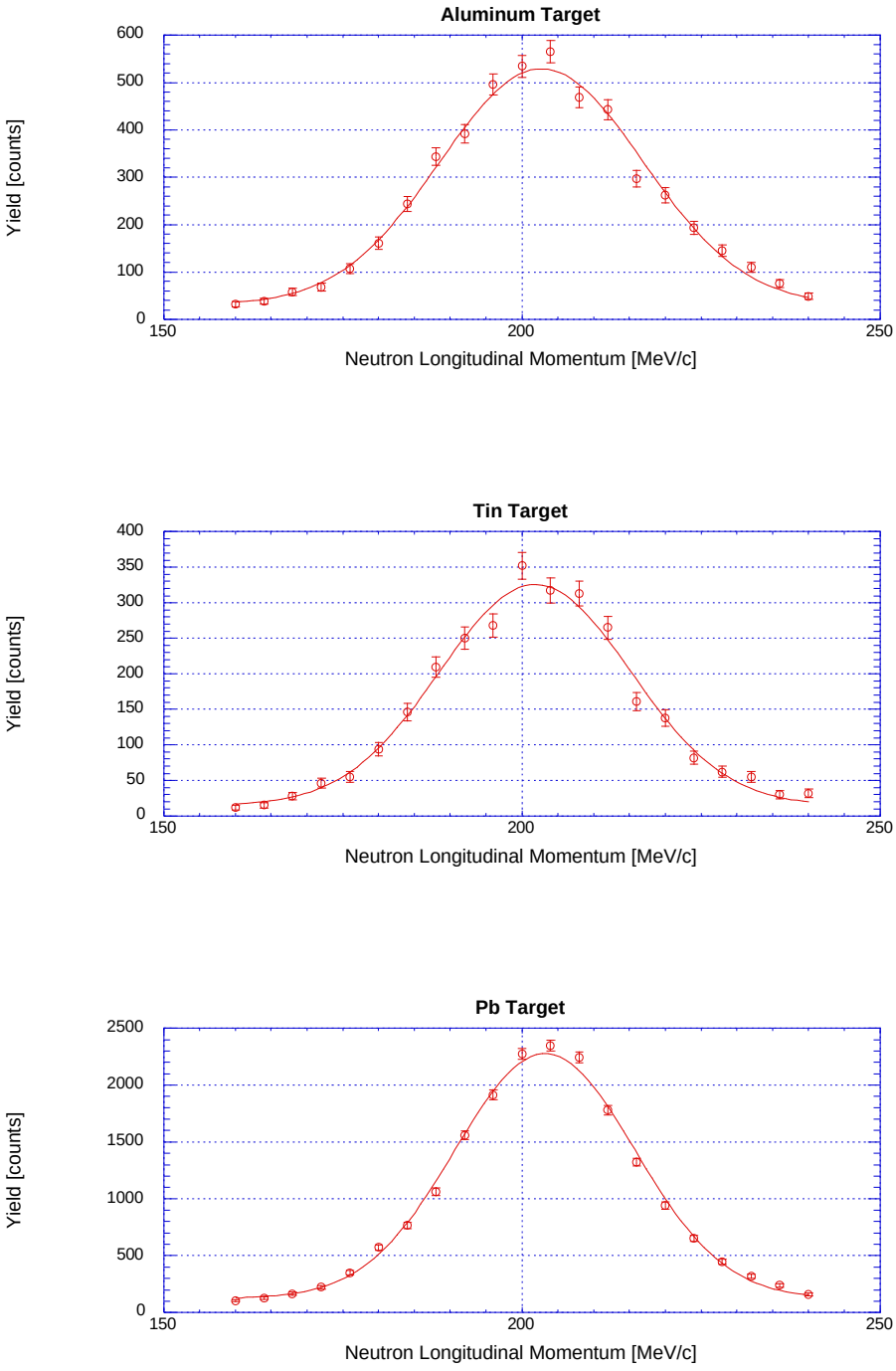

Figure 25 -- Longitudinal momentum distributions of neutrons measured from breakup of ^{11}Li on three targets. The lines are Gaussian curve fits, which were used to extract the intrinsic neutron momenta from experimental effects.

The longitudinal momentum distributions are well fitted by Gaussians. As seen in Table 4, the width parameter is independent of reaction target. The ^{9}Li distributions are slightly broader than those measured by Orr *et al*. on targets of Beryllium, Niobium, and Tantalum. [25] The measurements by Orr also produced distributions which showed no clear dependence on target, and had widths of $s \approx 19 MeV/c$. Measurement of the fragment longitudinal momentum distribution was once viewed, in the context of the Serber model, as a direct probe of the neutron halo wave function. [28] Unfortunately, reactions which preserve the ^{9}Li core in the final state are generally peripheral in nature, and therefore only sample the portion of the wave function external to the radius of the core. [29,30] Consequently, the observed distributions are narrower than the intrinsic momenta of the bound halo neutrons.

4.2.2 Fragment and Neutron Transverse Momenta

Unlike the distributions measured in the beam direction which are thought to sample a portion of the intrinsic momentum of bound nucleons, transverse momentum measurements have been shown to be dependent on reaction mechanism. Several different reaction processes can lead to the dissociation of ^{11}Li and the observation of ^{9}Li or neutrons in the final state. The first, dominant for targets with high Z, is coulomb dissociation, which results in a ^{9}Li fragment and two forward focussed, beam velocity neutrons. The second mechanism, important at smaller impact parameters than typical of coulomb excitations, is diffractive dissociation. In this case, one of the halo neutrons is diffracted by the target nucleus, just as light waves are diffracted by a black sphere. [27] Diffractive dissociation leads to a ^{9}Li and one forward focussed, beam velocity neutron in the final state, as well as one diffracted neutron, which forms a broad angular distribution. A third reaction process, also important at small impact parameters, is stripping. In this case, one of the halo neutrons collides with the target nucleus and is scattered or absorbed by the target. This reaction also results in a fragment and one

forward focussed neutron in the final state. Some measurements of neutron transverse momentum distributions have been reported to correspond to the superposition of a narrow and a broad component. [23,6] While inconsistent with the intrinsic momentum of a bound halo neutron, the broad components of the measured distributions can be understood to arise from diffractive dissociation of the nucleus. [27]

Since the current experiment was performed on several targets such as aluminum, for which diffraction and stripping are thought to dominate, and lead, which induces primarily coulomb dissociation, we had hoped to compare directly the momentum distributions arising from various reaction mechanisms. Barranco predicts that the distribution of transverse momentum of neutrons diffracted by aluminum target nuclei will exhibit a full width at half maximum of 135 MeV/c, compared to a target independent longitudinal full width of only 35 MeV/c. Unfortunately, the low beam energy, which was chosen to optimize the operation of the Neutron Walls and Beam Sweeping Dipole, caused the diffracted neutrons to be emitted at large angles in the laboratory. The acceptance of our setup began to fall for neutrons with transverse momenta exceeding 18 MeV/c, and was zero for neutrons with transverse momenta greater than 46 MeV/c. Therefore, this measurement was not sensitive to effects such as the diffraction of halo neutrons.

The measurement of ^{9}Li fragment transverse momenta, however, proved to be highly target dependent, with the width of the distribution increasing with target Z. This effect simply reflects the greater average scattering angle of fragments produced from reactions with the high Z targets. Table 5 shows the average 9Li scattering angle measured with each target. 9Li fragments created by the lead target were scattered through the largest angle, and correspondingly, the transverse momentum distributions measured with the lead target were the broadest.

Target	Average ^{9}Li θ
Al	2.7°
Sn	2.9°
Pb	3.3°

Table 5 – Average ^{9}Li scattering angle measured with all three targets.

Figure 26 shows the neutron transverse momentum distributions measured in coincidence with a ^{9}Li fragment on each of the three reaction targets. The distributions have been corrected for the momentum dependent acceptance of the detectors, and are fitted with a two dimensional Gaussian of the form $ds/dp = p\exp(-p^2/2s^2)$. Figure 27 shows the ^{9}Li transverse momentum distribution measured on each of the three targets. Like the neutron transverse distributions, they have been fitted with two dimensional Gaussians. The widths of the distributions are summarized in the table below.

Target	9Li $P_\perp$ σ [MeV/c]	n $P_\perp$ σ [MeV/c]
Al	79 ± 3	15 ± 2
Sn	95 ± 5	15 ± 3
Pb	101 ± 3	15 ± 1

Table 6 – Summary of the widths of ^{9}Li and neutron transverse momentum distributions. The widths are sigmas of two dimensional Gaussians fitted to the data.

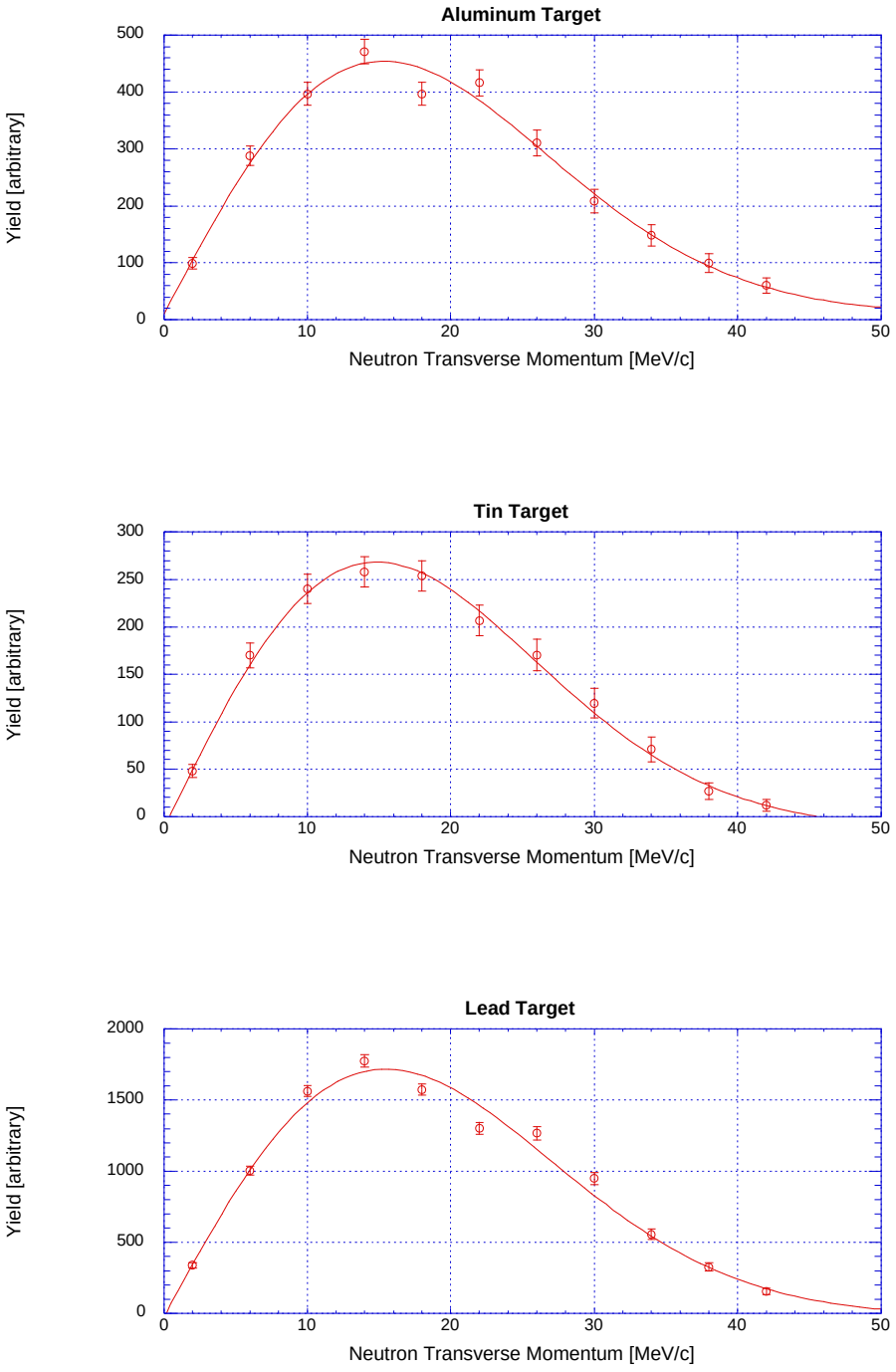

Figure 26 – Neutron transverse momentum distributions. The curves are two dimensional Gaussians which were fitted to the data.

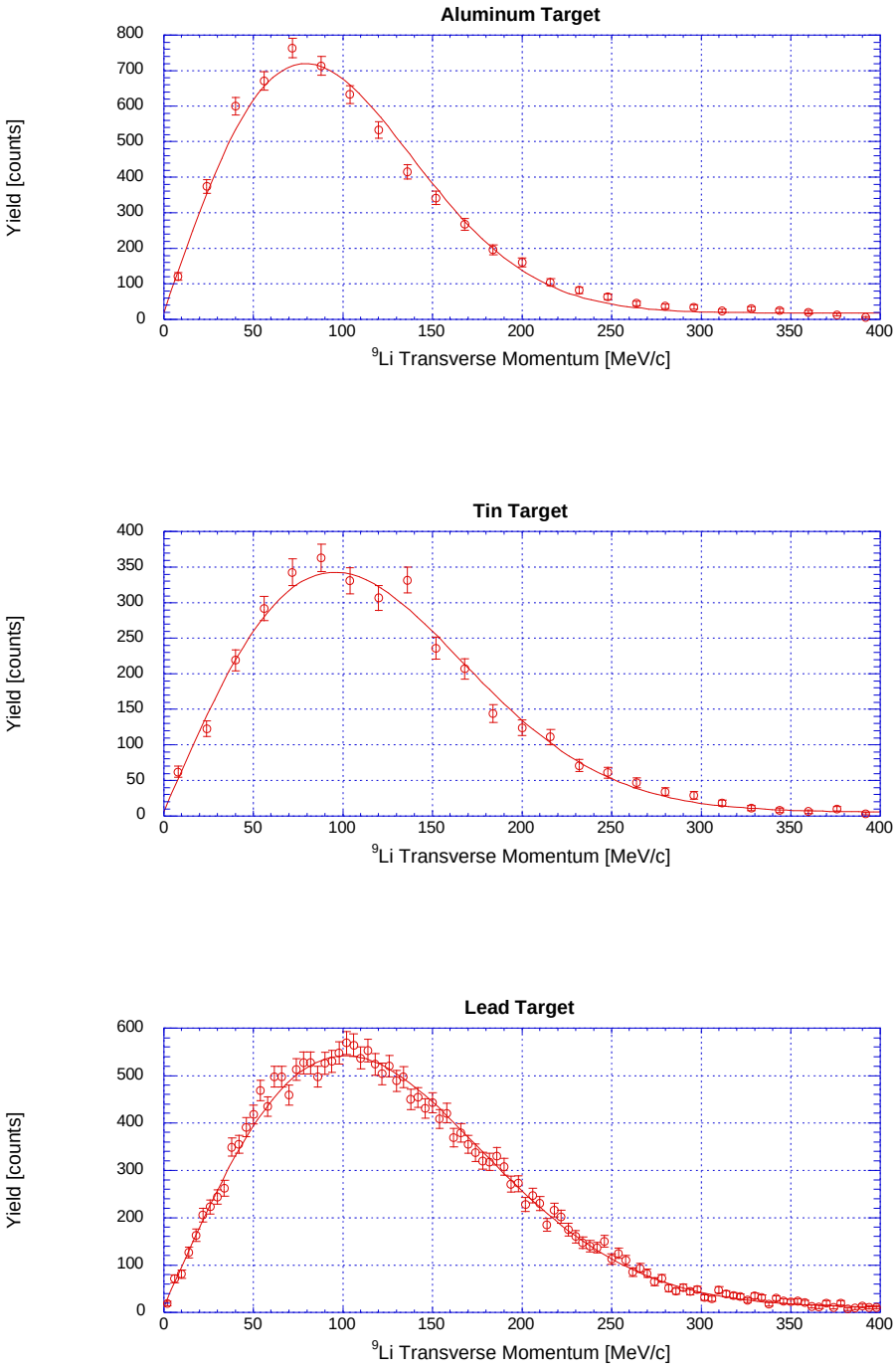

Figure 27 – ^{9}Li transverse momentum distributions. These distributions are measurements of the fragments' momenta perpendicular to the direction of the ^{11}Li beam. The curves are two dimensional Gaussians which were fitted to the data.

4.2.3 Fragment and Neutron Momenta in ^{11}Li Center of Mass Rest Frame

The complete kinematics of the ^{11}Li dissociation study allowed us to calculate the velocity of the ^{11}Li center of mass in its three body final state. The momentum of the ^{9}Li fragment and each of the two neutrons could then be calculated in the center of mass rest frame. In the measurement on the lead target, most reactions which led to the detection of all three particles in the final state were the result of peripheral coulomb interactions. Because these reactions were caused by low energy excitations, they offer a probe into the ground state of ^{11}Li with the smallest possible perturbation. Therefore they may provide the best insight into properties such as the degree of correlation of the halo neutrons. Hansen has suggested that if the ^{9}Li fragment recoils against a dineutron-like structure, the width of its momentum distribution will be twice as large as that of the neutrons. If, on the other hand, the neutrons are completely uncorrelated, the fragment momentum distribution will only be broader than the neutrons' width by a factor of $\sqrt{2}$. The center of mass rest frame distributions measured by Sackett et al. were parameterized by three dimensional Gaussians, with widths $s_9 = 18 \pm 4$ MeV/c and $s_n = 13 \pm 3$ MeV/c, suggesting that the dissociations were well characterized by a completely uncorrelated phase space breakup.

Figure 28 shows the distributions measured in the current work. They are fitted with three dimensional Gaussians of the form $ds/dp = p^2 \exp(-p^2/2s^2)$ with widths $s_9 = 30 \pm 2$ MeV/c and $s_n = 14 \pm 1$ MeV/c. In the context of this discussion, the measured distributions seem to suggest a very strong correlation between the halo neutrons in the ground state of ^{11}Li. However, analysis of our excitation energy spectra in Section 4.3 will show that in fact, the relative widths of the two distributions are indicative of a direct breakup mechanism in which an impulse is delivered to the core of the nucleus, pushing it out of the neutron halo.

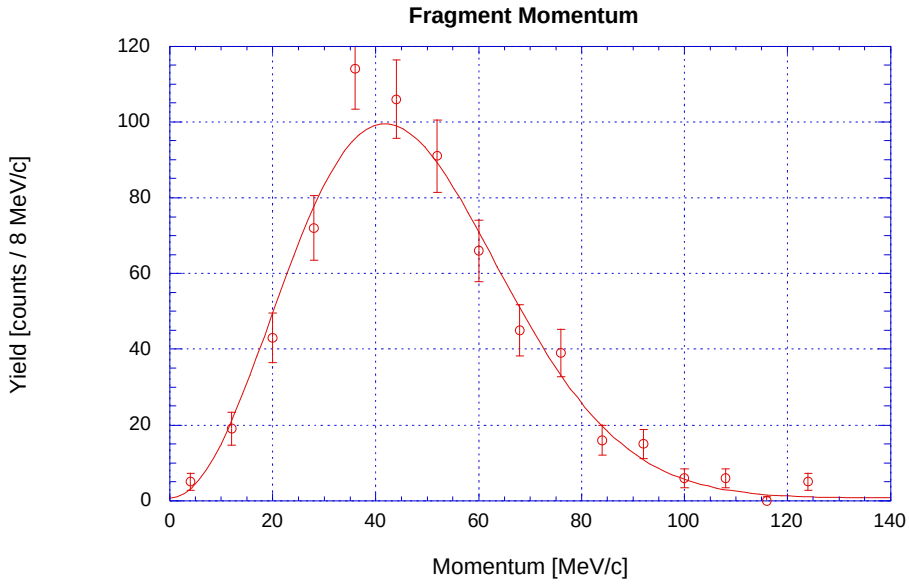

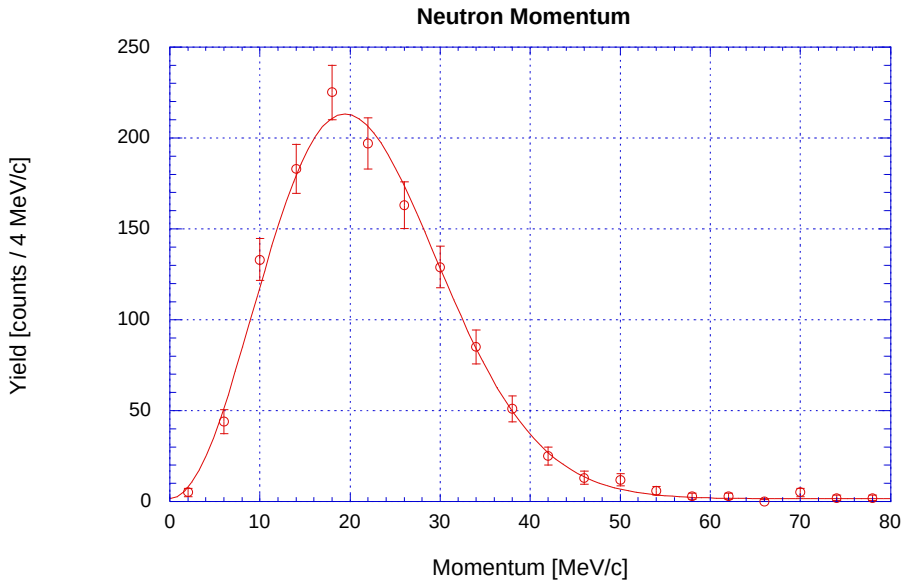

Figure 28 – ^{9}Li and neutron momentum distributions determined in the ^{11}Li rest frame. The curves are three dimensional Gaussians which were fitted to the data.

4.3 ^{11}Li Decay Energy Spectra

The purpose of the 1991 ^{11}Li experiment by Sackett *et al*. was to make a kinematically complete measurement of coulomb dissociation events. By measuring the energies and angles of all three particles in the final state, the decay energy, E_d, of the dissociation could be calculated. The two-neutron separation energy, S_{2n}, is known to be 0.30 MeV for ^{11}Li [12], and so the excitation energy, E_x, of the event was calculated by the simple relation:

$E_x = E_d + 0.30$ MeV

It was estimated that 80% of the reactions observed were due to electric dipole excitation by the virtual photon field of the lead target. Measuring the excitation energy for many events allowed the experimenters to map out the electric dipole excitation function $\sigma_{E1}(E)$ for ^{11}Li, using the relation:

$$\frac{ds_c}{dE} = \frac{N_{E1}(E)}{E} * s_{E1}(E)$$

where $N_{E1}(E)$ represents the flux of virtual photons of energy E. Finally, the electric dipole strength dB(E1)/dE could be calculated from the expression:

$$s_{E1}(E) = \frac{16p^3}{9\hbar c} E \frac{dB(E1)}{dE}$$

While the 1991 experiment successfully measured electric dipole excitations to energies of 700 keV, no study was made with lighter targets, where coulomb excitation is no longer the dominant reaction mechanism. Our current work repeated the dissociation measurements on a lead target, this time detecting neutrons with the Neutron Wall arrays, increasing our efficiency for detecting excitations of higher energy. In addition, measurements were made with targets of aluminum and tin, allowing for a systematic study of the ^{11}Li excitation spectrum when mechanisms such as neutron stripping and diffraction may be comparable to or greater than the coulomb excitation strength.

The decay energy E_d was determined for each ^{9}Li – 2-neutron coincidence event. It was calculated with the expression:

$$E_d = \frac{1}{2} m1 \left|\vec{V}^2_{2n-9}\right| + \frac{1}{2} m2 \left|\vec{V}^2_{n-n}\right|$$

where $m_1 = \frac{m_9(2m_n)}{m_9 + 2m_n}$ and $m_2 = \frac{m_n}{2}$. The mass of ^{9}Li is m_9, and m_n is the mass of a neutron. $\vec{V}_{2n-9}$ is the relative velocity between the ^{9}Li and the two-neutron center of mass, and $\vec{V}_{n-n}$ is the relative velocity between the two neutrons in the rest frame of the two-neutron center of mass.

Some fraction of the fragment – two-neutron coincidences measured were caused by reactions in the silicon strip detectors. As we did in the calculation of the two-neutron removal cross sections, we assumed that silicon and aluminum acted identically as target nuclei. The decay energy distribution measured from the aluminum target was normalized to the total number of counts calculated to have come from the silicon detectors in both the tin and lead runs, and was subtracted from those curves.

In addition to subtracting contributions from the silicon detectors, the decay energy curves had to be corrected for acceptance effects of the Neutron Walls. The Neutron Walls were built specifically to subtend a large solid angle and boost efficiency for detecting events with high excitation energy. However, because of the vertical aperture defined by the poles of the Beam Sweeping Dipole, the efficiency of the experiment began to fall off at decay energies as low as 250 keV. Unfortunately, when measuring reactions with three bodies in the final state, any correction for solid angle acceptance requires the assumption of a model for the decay of the nucleus. In this analysis, two models were selected and studied with a Monte Carlo simulation.

In the first model, a sequential decay model, the breakup proceeded through an intermediate ^{10}Li resonance with an energy of 240 keV. The first neutron recoiled against a bound ^{10}Li system, with all but 240 keV of the available decay energy shared

between the neutron and the ^{10}Li. In the second step of the process, the second neutron recoiled against the ^{9}Li fragment, with the two particles sharing the remaining 240 keV. The other decay mechanism studied in this analysis was a three body, phase space model. In this simulation, the excited ^{11}Li decays directly to a ^{9}Li and two free neutrons, with all three particles sharing the available decay energy in a somewhat random fashion, as allowed by the available phase space. Figure 29 shows the calculated solid angle acceptance of the Neutron Walls for each of the two breakup models as a function of decay energy. Since the two models give very comparable results, only the phase space calculation was used for the remainder of the analysis.

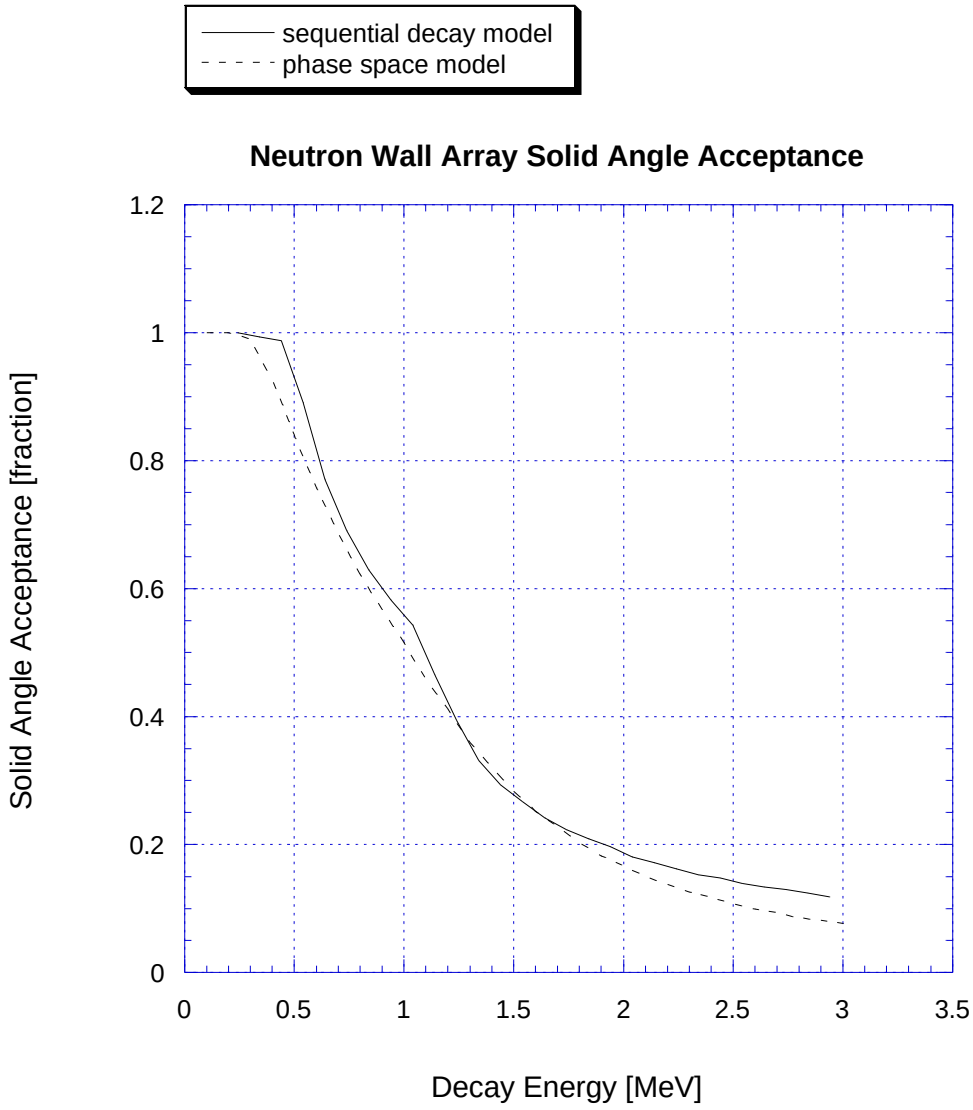

Figure 29 – Solid angle acceptance of the Neutron Walls, determined from two Monte Carlo simulations.

Besides the solid angle acceptance of the Neutron Walls, there are other factors affecting the total neutron detection efficiency. One factor corrects for lost two-neutron detection efficiency in the case that both neutrons interact in the same cell of the Neutron Walls. These events look like single neutron interactions, and result is a small loss of two-neutron efficiency, especially for events of very low decay energy. The other, more important factor is the intrinsic neutron detection efficiency of the Neutron Wall. This number reflects the percentage of neutrons, incident on the array, which are actually detected. The intrinsic detection efficiency is calculated using TOTEFF [32], a standard computer routine for computing the efficiency of neutron detection with liquid scintillator devices. We used TOTEFF to determine that for 22 MeV neutrons like the ones created in our experiment, a maximum of 13.8% of those which are incident on one Neutron Wall may be detected. These two factors are combined to determine our total two-neutron detection efficiency. Plotted below, as a function of decay energy, the two-neutron efficiency represents the fraction of events with a given decay energy for which we detect both neutrons in the final state. The curve in Figure 30 uses the phase space simulation for a calculation of solid angle acceptance.

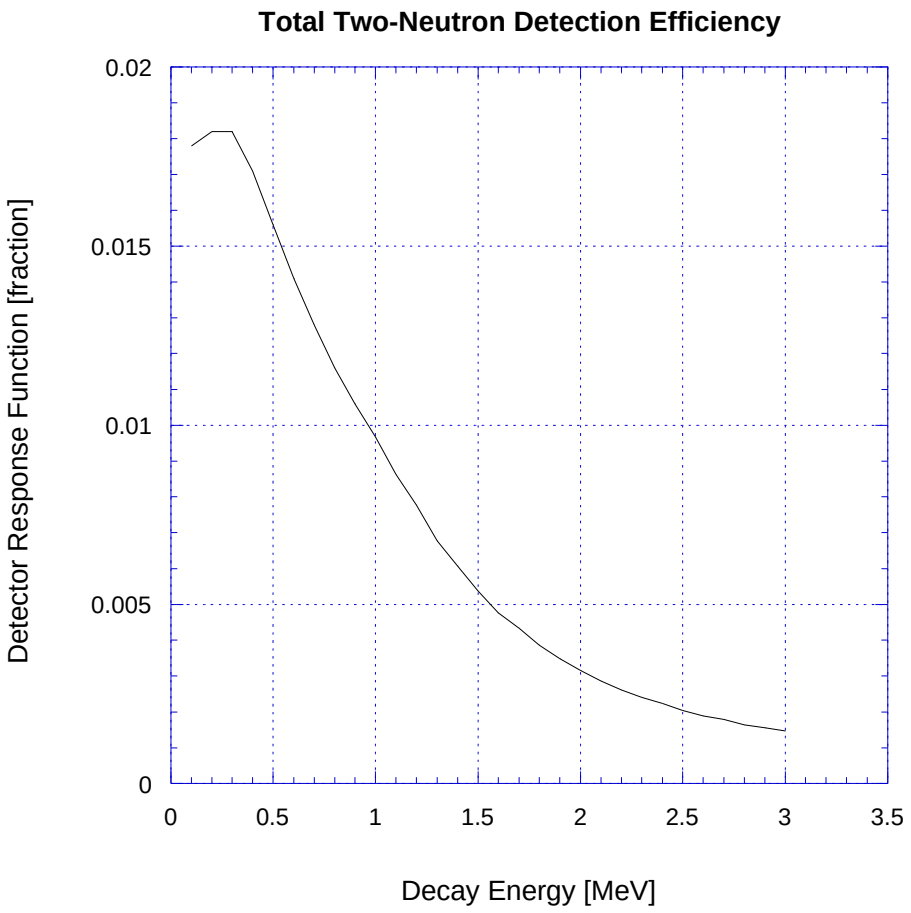

Figure 30 – Total Neutron Wall response function calculated for phase space breakup of ^{11}Li. Including geometrical acceptance of the Walls and intrinsic efficiency of the detectors, this curve represents the fraction of ^{11}Li dissociations in which we detect both neutrons.

In Figure 31 are the decay energy curves for ^{11}Li on targets of aluminum, tin, and lead. The plot for the aluminum curve represents contributions from both the reaction target and the silicon detectors. The curves for tin and lead have had the contribution from the silicon subtracted away, using the spectrum measured with the aluminum target. Also shown are the decay energy curves for all three targets, corrected by the total detection efficiency plotted in Figure 30

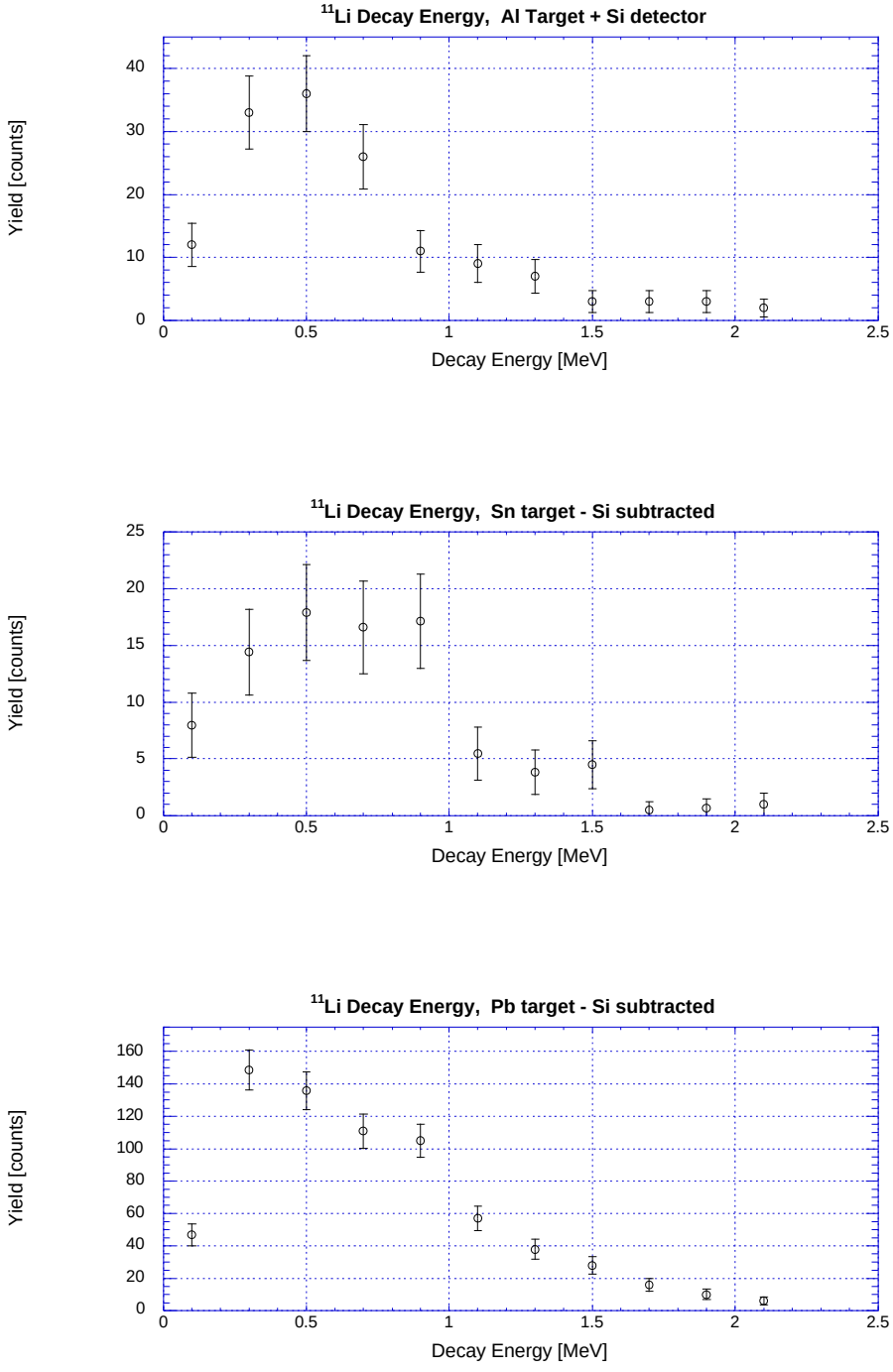

Figure 31 – Decay energy spectra for ^{11}Li measured on targets of Al, Sn, and Pb. The effect of the silicon detectors on the Sn and Pb spectra has been determined from the measurement with the Al target, and subtracted out.

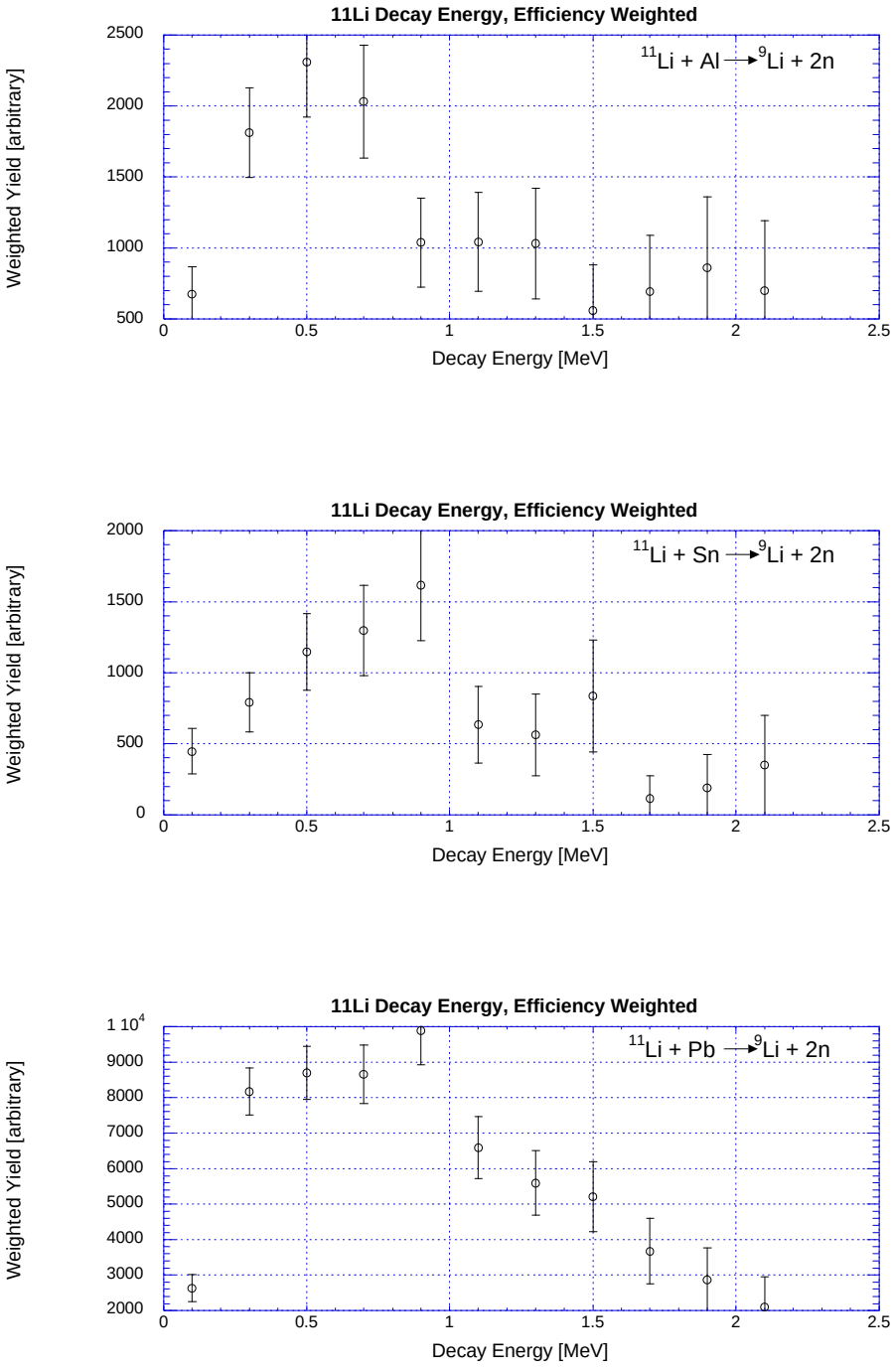

Figure 32 – Decay energy curves of ^{11}Li on targets of Al, Sn, and Pb, weighted by total neutron detection efficiency.

With the decay energy curves corrected for detector efficiencies, we can compare the number of counts in each bin of decay energy to the number of incident ^{11}Li particles, and calculate a measured differential cross section, $d\sigma_m/dE$. The cross sections for the three targets are shown below.

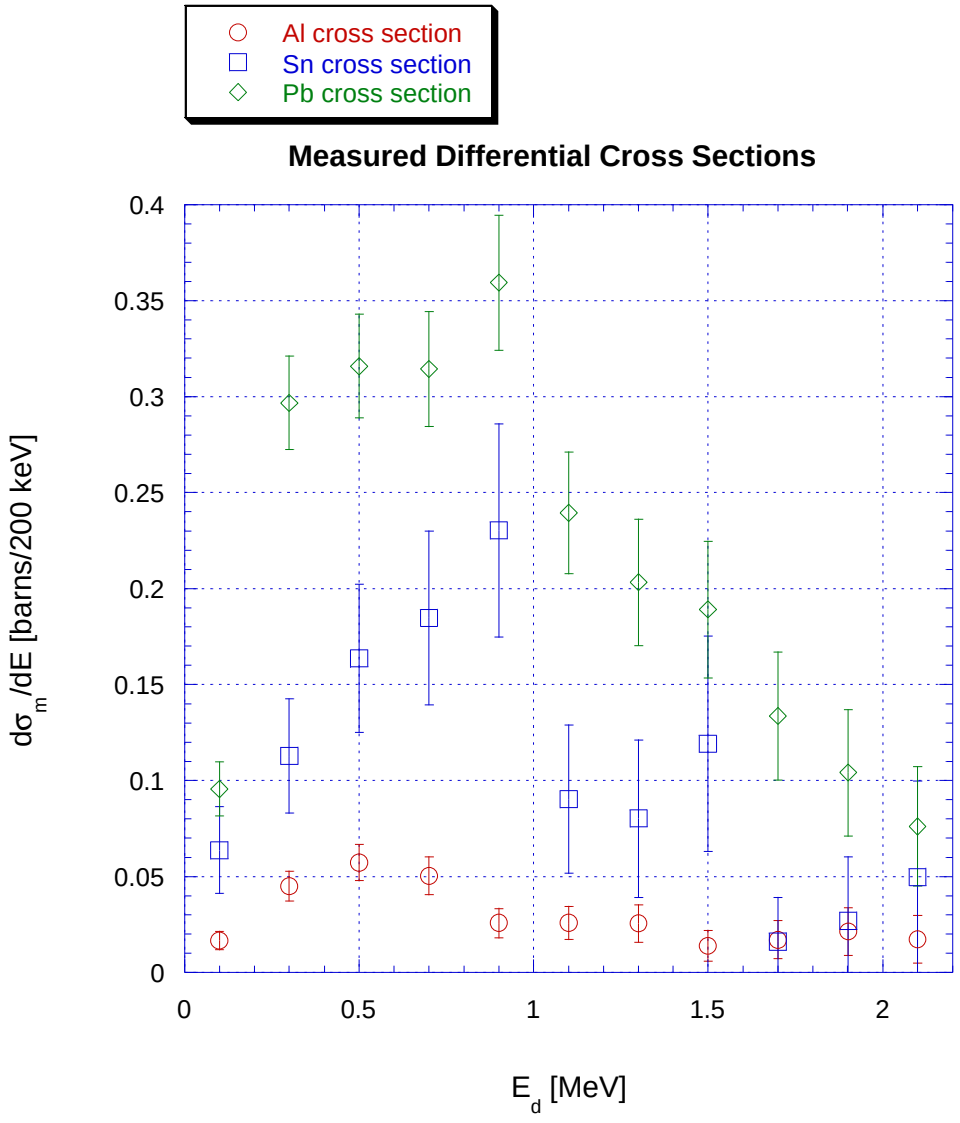

Figure 33 – Measured Differential Cross Sections for ^{11}Li on all three reaction targets. The cross sections include nuclear and coulomb reaction mechanisms.

While the total reaction cross section measured with the aluminum target, 0.7 ± 0.1 barns, is more than a factor of five smaller than the cross section on lead, 5.0 ± 0.4

barns, the virtual photon spectrum from the aluminum target is less intense by a factor of 40. Therefore, while the lead target reaction mechanism is predominantly a coulomb process, the aluminum cross section is dominated by nuclear interactions. Since we expect the nuclear cross section to scale like $A^{1/3}$, where A is the target mass number, we can scale the differential cross section measured with the aluminum target to calculate and subtract the nuclear component of the spectrum obtained with the lead target.

If we assume that the observed cross section from the lead target was due entirely to coulomb excitation, then the electric dipole strength function B(E1) can be mapped out as prescribed above. In order to do this, the virtual photon spectrum from the lead target must be calculated. We used a relatively simple form for the photon spectrum, based on a relativistic approximation. [33,34] The approximation assumes only straight line projectile trajectories, and has been shown to be applicable even to the low beam energy used in this experiment [1]. The spectrum is calculated as:

$$N_{E1}(E) = \frac{2}{p} Z_T^2 a \left(\frac{c}{v}\right)^2 \left[c\mathrm{K}_0(c)\mathrm{K}_1(c) - \frac{1}{2}\left(\frac{v}{c}\right)^2 c^2 \left(\mathrm{K}_1^2(c) - \mathrm{K}_0^2(c)\right)\right]$$

K_0 and K_1 are modified Bessel functions of the argument χ, with $c = Eb_{\min}/\hbar g v$. For this calculation, b_{min} was set to the sum of the nuclear radii of Pb and ^{11}Li. We used a value of 3.2 fm for the value of the ^{11}Li radius. [1] The calculated virtual photon spectrum for the lead target is shown in Figure 34. For comparison, a virtual photon spectrum was also calculated for the tin and aluminum targets, as well.

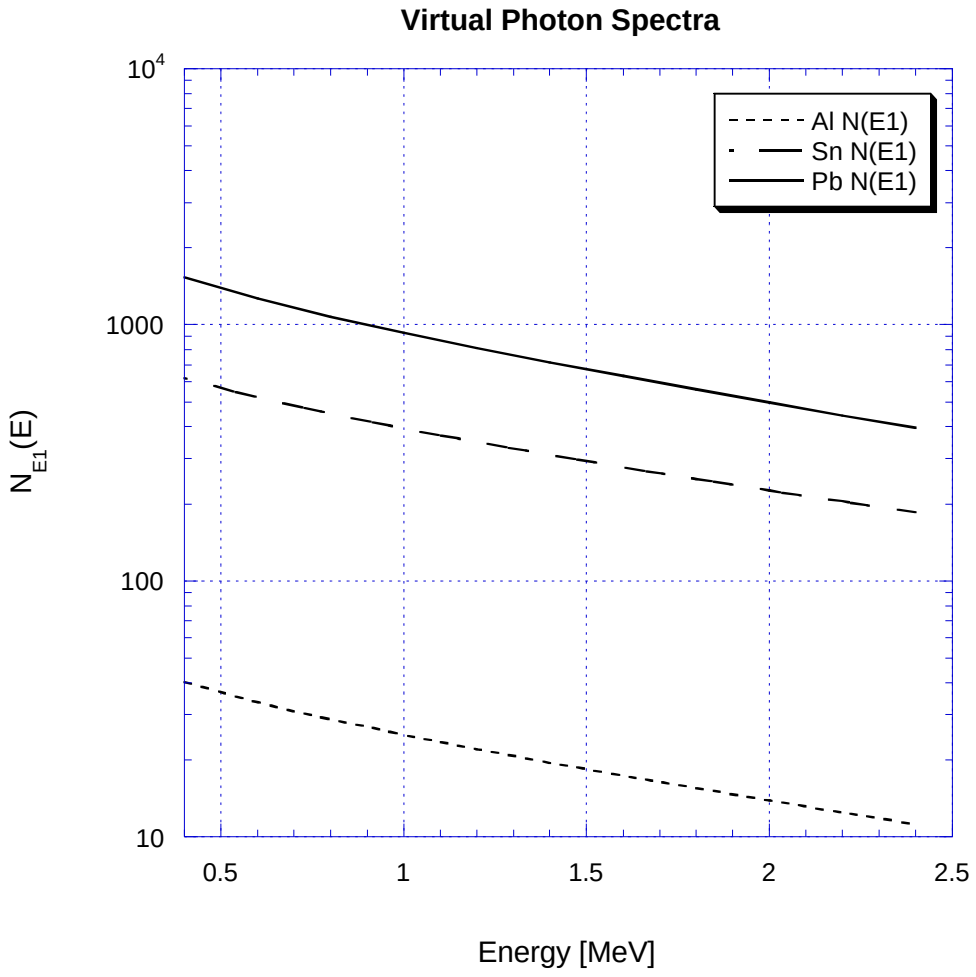

Figure 34 – Virtual photon spectra calculated for 25 A MeV 11Li on targets of Al, Sn, and Pb, using a relativistic approximation.

The virtual photon spectrum shown in Figure 34 can be used to calculate the electric dipole strength for ^{11}Li, using the lead target cross section data. Because experimental effects such as neutron acceptance have been divided out of the data, our B(E1) curve can then be compared to other experiments and theories. An obvious comparison to make is with the B(E1) strength measured in Sackett's 1991 experiment. Because the detector efficiencies were considerably more complicated than in the current work, the intrinsic strength function was not unfolded from the detector response.

Instead, a Briet-Wigner resonance was assumed for the shape of the true strength function. This representation of the strength function was then driven through a Monte-Carlo simulation of the experiment, and the results were compared with the measured cross section. A best fit to the data was obtained with a resonant energy of E_0=0.7 MeV and width Γ = 0.8 MeV. The function also included a transmission coefficient, T(E), appropriate for the energy dependence of s-wave neutrons.

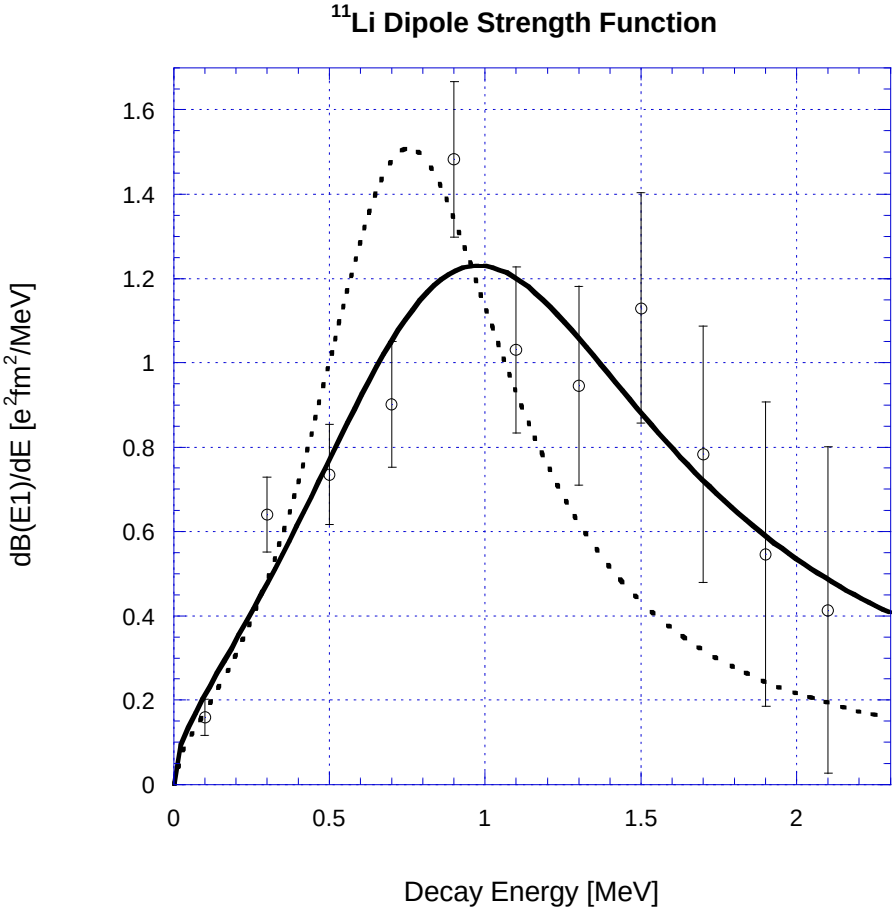

Figure 35 – Electric Dipole Strength function of ^{11}Li, measured with lead target. The solid curve represents a fit to the data with a Breit-Wigner function; E_0 = 0.83 MeV and Γ = 1.5 MeV. The dotted curve represents the strength function measured by Sackett *et al*.

Fitting the data from the current work to a Breit-Wigner function yields a resonant energy $E_0 = 0.83 \pm 0.07$ MeV and a width, $\Gamma = 1.5 \pm 0.3$ MeV. The resonance energy is slightly higher than the value reported by Sackett, and the width measured in this experiment is larger than Sackett's by a factor of two. These discrepancies are understandable, as the small array of neutron detectors used in the prior study did not provide experimenters enough efficiency to sample high decay energy events.

Another kinematically complete measurement of ^{11}Li dissociation on lead was measured at 43 MeV/A by S. Shimoura *et al*. [17]. The excitation function measured in his study also exhibited a peak near 0.7 MeV of decay energy, and also had a high-energy tail that extended beyond the region measured by Sackett *et al*. Although Sackett's data were fitted with a Breit-Wigner resonance curve, the data displayed evidence of a direct breakup mechanism as opposed to decay through a resonant state. This observation will be discussed in section 4.4. Like Sackett's data, the measurement by Shimoura also seemed to point to a direct breakup mechanism.

The electric dipole strength function measured by Shimoura *et al*. was compared to a theoretical function calculated by Pushkin, Jonson, and Zhukov. [35] The calculation produces an analytical dipole strength function, derived in a three-body model which uses Yukawa wavefunctions for the ground state, and three-body plane waves for the final state. The expression can be used to calculate the strength function for any two-neutron halo nucleus, and requires only knowledge of the two-neutron separation energy S_{2n}. While the exact expression is a hypergeometrical function that is fairly involved to compute, the authors found that it can be approximated quite well with a simple approximation using an effective binding energy $S_{2n}^{eff} = a \cdot S_{2n}$. The approximation is given by:

$$\frac{dB(E1)}{dE} \propto \frac{E^3}{\left(s_{2n}^{eff} + E\right)^{11/2}}$$

Pushkin *et al.* found good agreement between their calculation and the Shimoura data using a binding energy of $S_{2n} = 0.34$ MeV, and $S_{2n}^{eff} = a \cdot S_{2n}$, with $a = 1.45 - 1.55$. This expression was fitted to our data, with S_{2n}^{eff}, and an over-all normalization as parameters of the fit. We obtained a best-fit value of 0.67 ± 0.06 MeV for S_{2n}^{eff}. Figure 36 shows our strength function, fitted with the Pushkin parameterization.

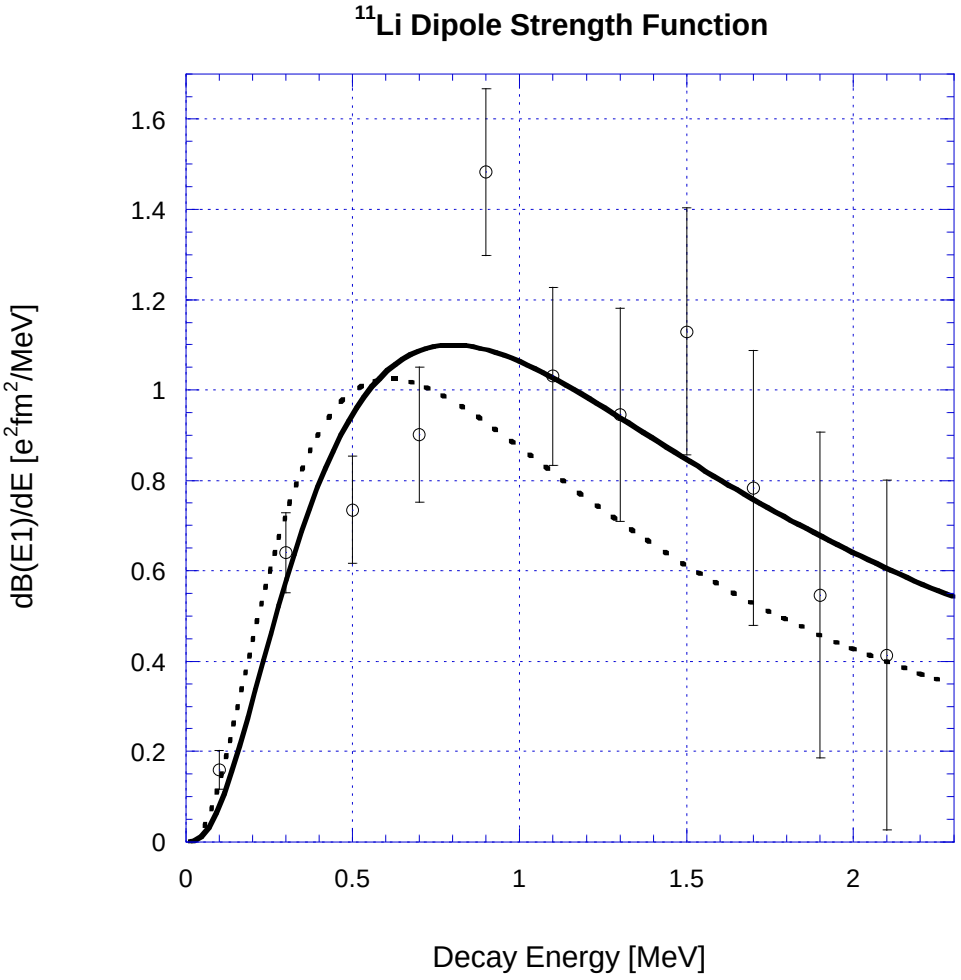

Figure 36 – Electric Dipole Strength function measured with lead target. The solid curve is a parameterization by Pushkin, with $S_{2n}^{eff} = 0.67 \pm 0.06$ MeV. The dotted curve represents the fit to Shimoura's data, with $S_{2n}^{eff} = 0.51$ MeV.

As mentioned, Shimoura *et al*. found in their data evidence for a direct breakup mechanism for the decay of ^{11}Li, as opposed to a decay which passes through a resonant state with a significant lifetime. In addition to analyzing the invariant mass of the entire ^{11}Li system after decay, Shimoura computed the relative energy between the ^{9}Li fragment and the two-neutron center of mass, $E_{^{9}Li-2n}$, as well as the relative energy between the two neutrons in the two-neutron center of mass rest frame E_{n-n}. These quantities are related to the total decay E_d energy by the relation:

$$E_d = E_{^{9}Li-2n} + E_{n-n}$$

If the ^{11}Li is excited to a resonance, and then decays to a three body final state, the decay energy spectra will be governed by the available phase space of the final states. In such a process, the average fragment – two-neutron center of mass relative energy, $\left\langle E_{^{9}Li-2n} \right\rangle$ will be roughly equal to the average neutron – neutron relative energy $\left\langle E_{n-n} \right\rangle$. The average decay energy measured in Shimoura's work was 1.7 MeV. The decay energy, however, was not equally partitioned between the two subsystems of the final state. Instead, they found that the majority of the available decay energy was consumed by the recoil of the ^{9}Li fragment against the two-neutron center of mass. They measured $\left\langle E_{^{9}Li-2n} \right\rangle$ = 1.15 ± 0.06 MeV, and $\left\langle E_{n-n} \right\rangle$ = 0.38 ± 0.03 MeV.

Our work, as well, indicates that on average, $E_{^{9}Li-2n}$ exhausts the majority of the available decay energy. Because the acceptance of the device used for our measurements provided less acceptance for high energy events than that used by Shimoura, our mean decay energy $\left\langle E_d \right\rangle$ was 0.738 MeV, somewhat lower than that measured by Shimoura. Our measured decay energy spectrum was parameterized with a Breit-Wigner curve, and this distribution was used to select decay energy for simulated events. The Monte-Carlo calculation simulated the phase space decay of ^{11}Li nuclei, specifically computing the quantities $E_{^{9}Li-2n}$ and E_{n-n}. The distribution of these quantities was then compared to the spectra measured in the experiment. The results of these comparisons are shown in Figure 37.

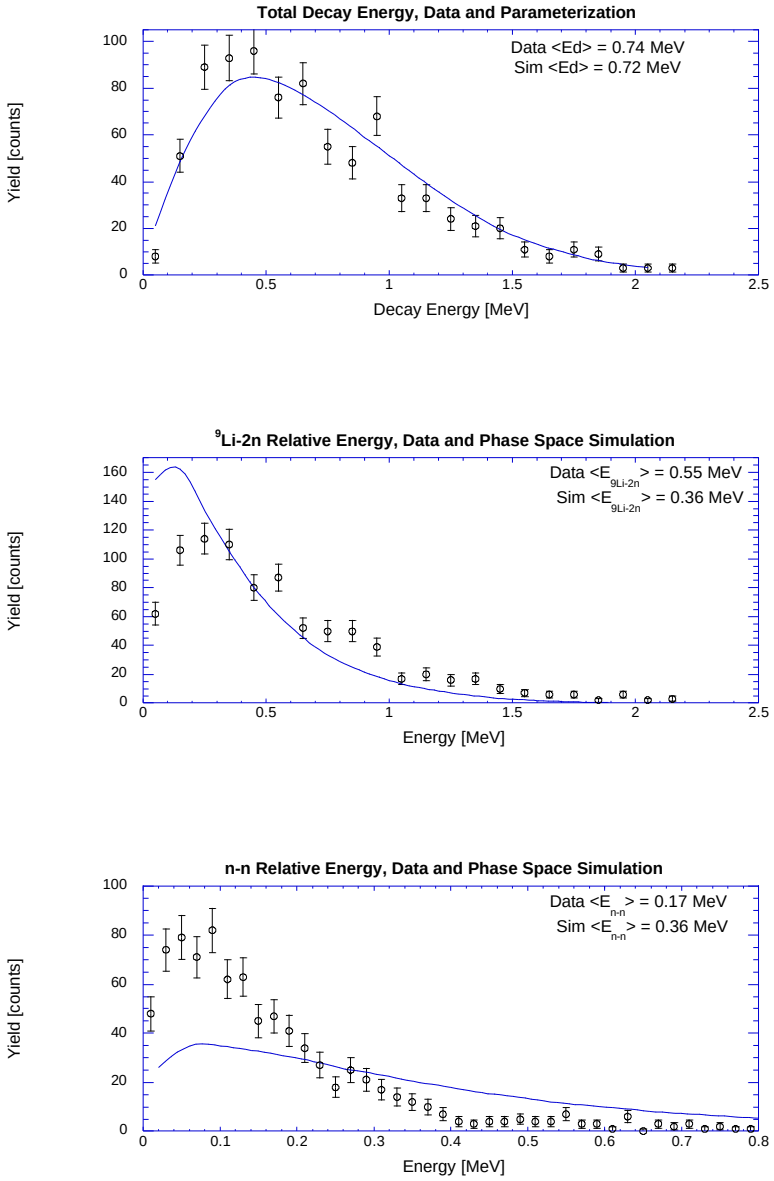

Figure 37 – Decay energy spectra measured for ^{11}Li on Pb. The top panel, which plots the total decay energy of the ^{11}Li system, was parameterized by a Breit-Wigner shape and that function was used to select decay energies for a simulation of three-body phase space decay of ^{11}Li. The curve in the top panel shows the Breit-Wigner function after being driven through the simulation and altered by the acceptance of the detectors. The points in the middle panel are the measured distribution of the ^{9}Li-2n portion of the decay energy. The solid curve shows the same parameter, obtained by the simulation of phase space decay. The bottom panel compares the measured distribution of the n-n relative energy to the phase space simulation. Average values for both data and simulation are reported on all spectra.

The simulation of phase space decay of a resonance in ^{11}Li predicts that for the total decay energy spectrum measured here, we would expect to find $\langle E_{^9Li-2n} \rangle$ = 0.39 MeV and $\langle E_{n-n} \rangle$ = 0.32 MeV. Instead we find that the majority of the available decay energy, 0.55 MeV on average, is exhausted by the ^{9}Li-2n subsystem. We interpret this observation as evidence of a direct breakup mechanism in the coulomb excitation of ^{11}Li. Rather than exciting a so-called soft dipole resonance in ^{11}Li which oscillates and then decays, the data suggest that the coulomb force of the target nucleus actually pushes the ^{9}Li core directly out of the ^{11}Li halo. The halo neutrons are essentially spectators in this process, and therefore a fairly small portion of the observed decay energy is seen in the relative energy of the two neutrons.

4.4 Post-Breakup Coulomb Acceleration

Perhaps the most surprising result derived from Sackett's 1991 ^{11}Li experiment was the observation that the velocities of the neutrons in the final state were, on average, lower than the velocities of the ^{9}Li fragments [1,2]. This velocity difference was interpreted as evidence of a direct breakup reaction mechanism, in which the ^{11}Li dissociates very close to the target lead nucleus. In this model, as the ^{11}Li projectile approaches a target nucleus, it is slowed by the large coulomb field of the lead. The coulomb field perturbs the ^{11}Li, and it is transformed directly into a three body final state consisting of a ^{9}Li fragment and two free neutrons. Because the ^{9}Li is still in close proximity to the lead nucleus, the repulsive coulomb force of the target accelerates the ^{9}Li fragment away, and it departs at a velocity higher than it had at the time of dissociation. The neutrons, however, are unaffected by the coulomb field of the lead, and so they continue to travel at the same velocity as they were at the moment of breakup. In this way, the average velocity of the neutrons tends to be lower than that of the fragments.

The difference between the average velocities of the two neutrons and the velocity of the fragment was calculated, event-by-event in Sackett's analysis. The centroid of this distribution was 0.008c. Assuming an average impact parameter for a breakup reaction of 20 fm, [36] it was determined that the velocity difference between fragments and neutrons corresponded to an excited state with a mean lifetime of 50 fm/c. A soft dipole resonance state with a lifetime of 50 fm/c would have a width of 4.0 MeV, which was more than four times the width of the peak measured in the dipole strength function. Therefore, the short lifetime of the excited ^{11}Li was interpreted as evidence of a direct breakup reaction mechanism, rather than a soft dipole mode.

The current experiment was designed to make a more systematic study of the coulomb acceleration effect. Kinematically complete measurements of ^{11}Li were made on a variety of reaction targets, as it was expected that the magnitude of the acceleration effect would vary with the size of the target nuclei's coulomb fields. A dependence of the acceleration on the target nucleus would lend credence to the effect as a physical phenomenon, as opposed to an artifact of a systematic error. In addition, the magnitude of the acceleration was studied as a function of impact parameter, as the effect is expected to be enhanced in reactions with the ^{11}Li travelling very close to the target nucleus.

The plots in Figure 38 show the magnitude of the difference between the ^{9}Li fragment's velocity and the average velocity of the two coincident neutrons. The data show that in this experiment, as well, the ^{9}Li's are travelling faster in the final state than the two neutrons. The centroid of the distribution measured with the lead target, 0.009±0.001c agrees with Sackett's measurement of 0.0090±0.0003c. Surprisingly, the magnitude of the velocity shift observed with the lead target is equal to the effect measured with the other targets, as well. We had expected to find a smaller coulomb acceleration effect for the data measured with the aluminum target than for the lead data, simply because the aluminum nucleus has a much smaller coulomb field than lead.

However, the complete kinematics of the measurements allowed a measurement of the angle of deflection of the center of mass of the ^{11}Li system by the target nucleus. Assuming pure coulomb trajectories for the ^{11}Li center of mass and neglecting recoil of the target nucleus, an average impact parameter can be calculated for dissociation events with each target, as can an average distance of closest approach. The acceleration of the ^{9}Li fragment is caused by the coulomb repulsion of the target nucleus, and in a simple assumption that dissociation occurs at the point of closest approach to the target, the amount of coulomb energy between the fragment and target can be calculated.

Target	Scattering Angle	Distance of Closest Approach	Coulomb Energy [MeV]
Al	2.7°	7.1 fm	7.91
Sn	2.9°	27 fm	8.00
Pb	3.3°	37 fm	9.56

Table 7 – The average scattering angle of the center of mass of the ^{11}Li is reported for each of the three reaction targets. Assuming pure coulomb trajectories, average distance of closest approach between projectile and target is calculated. Also reported is the coulomb energy between ^{11}Li and the target nucleus at the distance of closest approach.

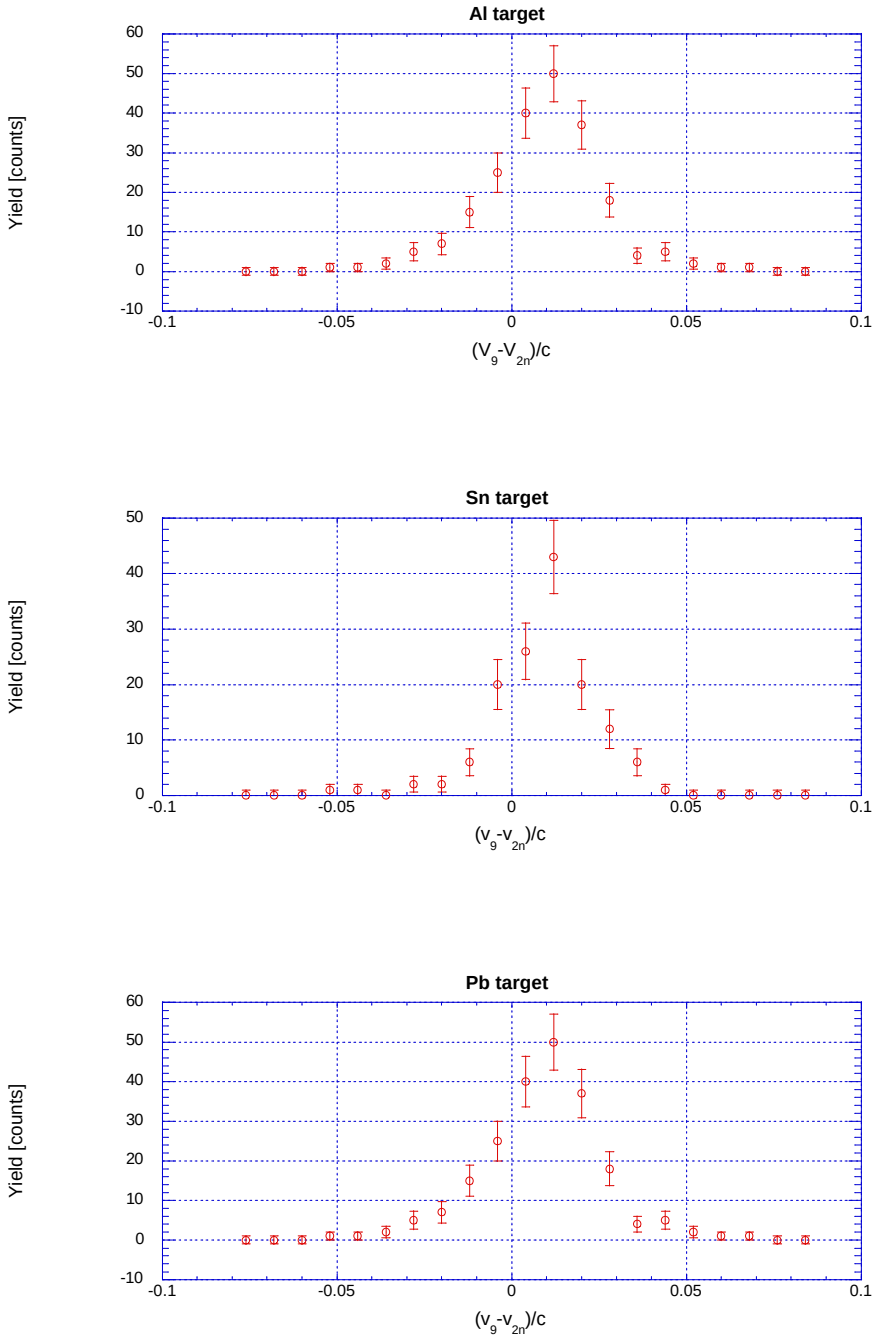

Figure 38 – Difference between the ^{9}Li velocity and the average each of the two neutron velocities. Distributions are shown for all three reaction targets. The centroids of the three distributions are 0.009 +/- 0.001 on Al, 0.010 +/- 0.001 on Sn, and 0.009 +/- 0.001 on Pb.

Table 7 summarizes the coulomb potential energy between a ^{9}Li fragment and each target nucleus, calculated at the distance of closest approach to each target, assuming pure coulomb trajectories. The calculations show that while there is a large difference in the coulomb field between the aluminum and lead nuclei, the potential energy between the targets and the ^{9}Li fragments differ less than 20% at the average distances of closest approach extracted from the data. The simplicity of this approach must be stressed, but it does show that it could be possible for all three targets to provide a similar coulomb acceleration effect.

As a critical evaluation of their coulomb acceleration observation, Sackett et. al. checked to confirm that their measurements displayed the conservation of momentum. Because the ^{11}Li projectile is much lighter than the lead target nucleus, it was assumed in Sackett's analysis that the recoil momentum of the lead nucleus could be ignored. If all measurements were performed correctly, then, the velocity of the incident beam particle should equal the velocity of the center of mass of the three body final state. The difference in velocity of the ^{11}Li system before and after breakup was calculated event-by-event, and the centroid of this distribution was –0.001 c, very near zero. This result provided a good check that the observed coulomb acceleration was not due to a systematic error.

A similar check was performed on the current measurement. Unfortunately, the difference in center-of-mass velocity before and after breakup is found to be non-zero for all three targets. The results are summarized in Table 8 below:

Target	COM velocity difference
Al	-0.0029 ± 0.0002 c
Sn	-0.0025 ± 0.0003 c
Pb	-0.0027 ± 0.0001 c

Table 8 – Difference between ^{11}Li center of mass velocity, before and after reaction. The table shows that for each of the three targets, the ^{11}Li center of mass tended to be travelling slower after breakup.

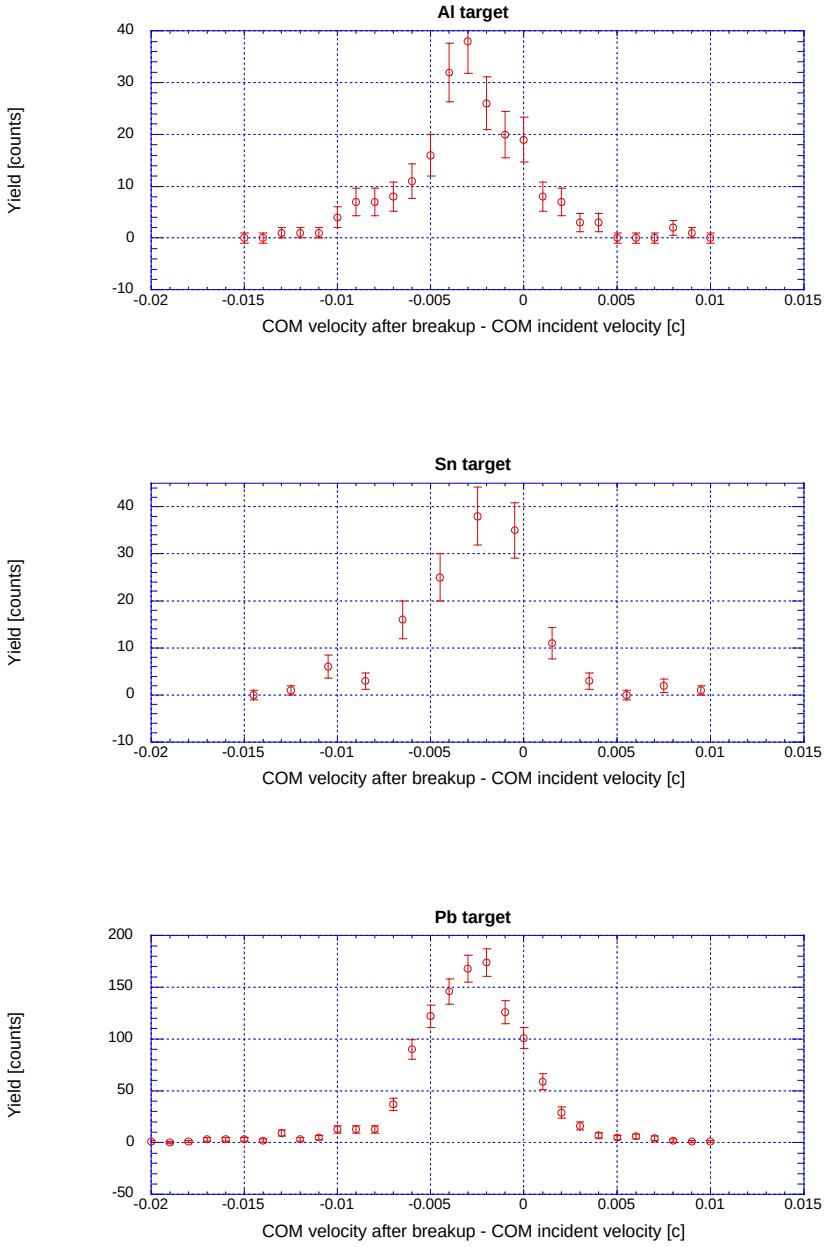

Figure 39 – COM velocity difference for ^{11}Li on each of the three reaction targets. The width of the peak for the lead data, 0.006 FWHM, represents the velocity resolution of the system. The dominant effect in this resolution is the 3% momentum aperture in the A1200 fragment separator which produced the ^{11}Li beam.

The fact that the center of mass velocity is observed to be somewhat less in the final state than the velocity of the incident beam means that we cannot exclude systematic error as the source of the coulomb acceleration effect we have measured. It should be noted, however, that in the 1991 experiment, each incident beam particle's velocity was measured by a timing scintillator. In the current work, the final state center of mass velocity is measured for each event, but this is compared to an average incoming beam velocity determined from the magnetic rigidity of the beamline. The beam particles' velocity distribution is expected to have a width of 3%, as defined by the momentum aperture at Image 1 of the A1200. This corresponds to a width of 0.007c, more than twice the measured shift in center of mass velocity. It is possible that the observed difference in center of mass velocity is due to an incorrect assumption of the average incident beam velocity. Therefore, while the observed difference between the final state center of mass velocity and incoming beam velocity does not support the existence of coulomb acceleration as a true phenomenon, the experimental uncertainties also preclude a dismissal of the observation.

Since Sackett's measurement of ^{11}Li dissociation, the coulomb acceleration effect has received some experimental scrutiny. In particular, two recent experiments have examined the breakup of the one-neutron halo nucleus ^{11}Be [37,38]. Both of these studies attempted to measure the magnitude of the coulomb acceleration of the ^{10}Be fragment as a function of impact parameter. It is expected that for events which occur with a smaller impact parameter, a direct breakup would occur closer to the target nucleus, resulting in a larger acceleration of the fragment. One of these studies [37] found that the magnitude of the effect increased with decreasing impact parameter, while the other found no such dependence on fragment velocity [38].

The complete kinematics of this work allow an event by event measurement of the deflection angle of the ^{11}Li center of mass. By making cuts on the data with respect to the deflection angle, and assuming simple coulomb trajectories, we can study the

average magnitude of the coulomb acceleration effect as a function of impact parameter. If we assume that dissociation occurs at the distance of closest approach for each trajectory, we can calculate the expected increase in the acceleration effect for smaller and smaller impact parameters. Figure 40 shows the difference between the ^{9}Li fragment velocity and the average velocities of the two coincident neutrons, as a function of impact parameter, for all three targets. Plotted with the data are curves displaying the expected trend in coulomb acceleration if the trajectories of the ^{11}Li were described by pure coulomb orbits and dissociation always occurred at the distance of closest approach for each impact parameter. Certainly, these assumptions greatly oversimplify the processes we are studying, and it would be surprising to find excellent agreement between the data and such predictions. However, if the data did display a trend similar to these calculations, we could say with some certainty that the observed velocity difference between fragments and neutrons is evidence of a direct break-up mechanism, and not the manifestation of a systematic error in the experiment. Unfortunately, no such trend is evident in the data.

The purpose of the analyses was to distinguish the observed coulomb acceleration effect from a possible systematic error. None of them have shown that the acceleration is inconsistent with such an error.

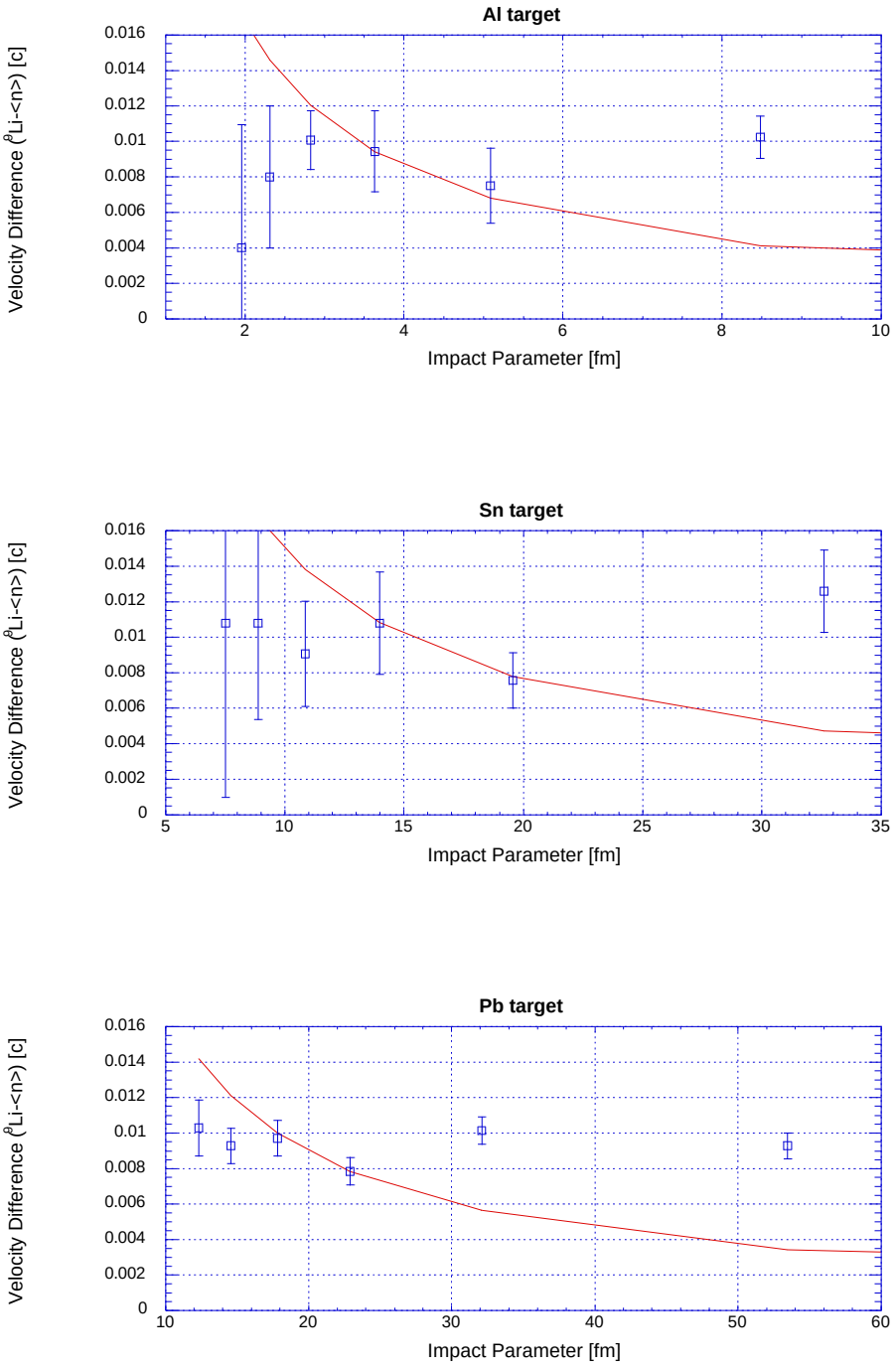

Figure 40 – Coulomb reacceleration of the ^{9}Li fragment plotted as a function of impact parameter for the dissociation event. The curves show the trend in the data which would be expected if all reactions occurred at the projectile's distance of closest approach to the target.

4.5 ^{10}Li Decay Energy

Theoretical models of ^{11}Li depend on knowledge of the ground state of the neutron unbound ^{10}Li nucleus. The shell model predicts that the ground state consists of a $0p_{1/2}$ neutron coupled to a $0p_{3/2}$ proton, forming a 1^+ or 2^+ state. However, for some light nuclei with N=7, the $1s_{1/2}$ state is lower in energy than the $0p_{1/2}$ state. The $½^+$ ground state of ^{11}Be is formed by a closed $0p_{3/2}$ proton shell and a $1s_{1/2}$ valence neutron. We might expect then, that the valence neutron of ^{10}Li would be found in a $1s_{1/2}$ orbital, coupling to a $0p_{3/2}$ proton to form a 1^- or 2^- ground state. [39,40,41]

Intense experimental interest in the structure of ^{10}Li has not done much to clear the picture. [16,42-50] Many experiments have observed a p-wave resonance, but the energy of the resonance is not well defined. The energy of the state has been reported at 800±250 keV, [46] and 538±62 keV. [48] Other references report the observation of two p-states, at 420±50 keV and 800±80 keV [47] and at 240±60 and 530±60 keV [44].

There are also a number of experiments which have reported very low energy ^{10}Li decays, interpreted as s-wave strength. [39, 49, 16,51] Unbound s-wave neutrons are not subject to coulomb or angular momentum barriers, and therefore do not constitute an actual resonance. The interaction is generally low in energy, and is commonly described in terms of a scattering length. An experiment at GSI by Zinser et al. [16] measured the decay energy of ^{10}Li after one neutron was stripped from a ^{11}Li projectile by a ^{12}C target. The data were parameterized by a pair of Breit-Wigner resonance shapes. The lower of the two resonance-like structures, located at 0.21 MeV was interpreted as an s-wave interaction, while the higher energy strength, peaked at 0.62 MeV, was believed to be a p-wave resonance. They reported an intensity ratio of 1:4 for the s to p components.

A recent paper by Bertsch et al. [51] provides parameterizations for the s-wave and p-wave structures in the decay energy spectrum of ^{10}Li. The s-wave distribution, characterized by a neutron-^{9}Li scattering length *a* is given by:

$$\frac{ds}{dE} \sim k\left[\frac{1}{a^2+k^2}\right]^2\left[\cos(ka)-\frac{a}{k}\sin(ka)\right]^2$$,with

$a/\hbar \approx \sqrt{2mE_B} = 0.124\, fm^{-1}$.

Bertsch parameterized the p-wave resonance with a Breit-Wigner shape:

$$\frac{ds}{dE} = A\frac{\Gamma}{(E-E_R)^2+\Gamma^2/4}$$

The width of the resonance, Γ, was given an energy dependence of the form

$\Gamma = E^{3/2}\frac{g_1}{1+g_2E}$, with g_1=2.74 MeV$^{-1/2}$ and g_2=3.3 MeV^{-1}.

Bertsch analyzed the Zinser neutron stripping data using his parameterizations for the s and p-wave interactions. To account for the effect of the experimental resolution, Bertsch used his calculations as the input to a Monte-Carlo routine which calculated the ^{10}Li decay energy after the angles and momenta of the particles were folded with a finite experimental resolution. The results of the Monte-Carlo calculations were fitted to the Zinser data by varying three parameters of the distribution. The parameters of the fit were: the s-wave scattering length *a*, the p-wave resonance energy E_R, and the s/p relative intensity. The best fit to the data was obtained with a scattering length a = -1 fm, E_R=0.25 MeV, and a relative intensity corresponding to 66% s-wave.

Our present work has allowed a similar study of the ^{10}Li system. We have observed the dissociation of ^{11}Li on targets of aluminum, tin, and lead. Reactions induced by the aluminum target are primarily neutron stripping reactions which leave us with a neutron unbound ^{10}Li system in the final state. The stripped neutron is usually absorbed by the target or scattered to a large angle where it cannot be detected by the Neutron Walls. The other halo neutron, interacting with the ^{9}Li fragment, is emitted in the forward direction in the laboratory frame, where it can be detected with our array. The ^{9}Li is detected in coincidence with the forward neutron, and a relative energy distribution is constructed for ^{10}Li. Just as in our measurement of the ^{11}Li decay energy, the acceptance of our neutron array decreases with increasing ^{9}Li-n relative energy. The

energy-dependent acceptance of our array was calculated and divided out of the measured spectrum.

The parameterizations given by Bertsch [51] for the s-wave and p-wave ^{9}Li-n interactions were sampled for the input of a Monte-Carlo calculation which folded in the angle and energy resolutions of our experiment. The output of the Monte-Carlo routine was then compared to our data, and the s-wave scattering length, the p-wave resonance energy, and the s/p relative intensity were varied to achieve a best fit to the data. Figure 41 shows the relative energy data and fits. The best fit is achieved with a scattering length a = -5 fm, resonance energy E_R=0.4 MeV, and a relative intensity corresponding to 60% s-wave. Also shown are the best fits which can be achieved with the scattering length fixed at a = -1 fm and a = -10 fm. Figure 42 shows the individual s and p components of the best fit.

The value of –5 fm for our best-fit s-wave scattering length suggests a stronger ^{9}Li-n interaction than the value of –1 fm obtained by Bertsch's fit of the Zinser data. However, other experiments have found an even stronger attraction, with Shimoura reporting a scattering length a = -16 fm [45] and Thoennessen measuring a < -20 fm. Bertsch [51] has pointed out that finite experimental resolution causes the measured data to rise less steeply at low relative energy than the theoretical curves do. Because the rise of our data is essentially defined by a single data point, it may be that the s-wave scattering length is even more negative than we have measured.

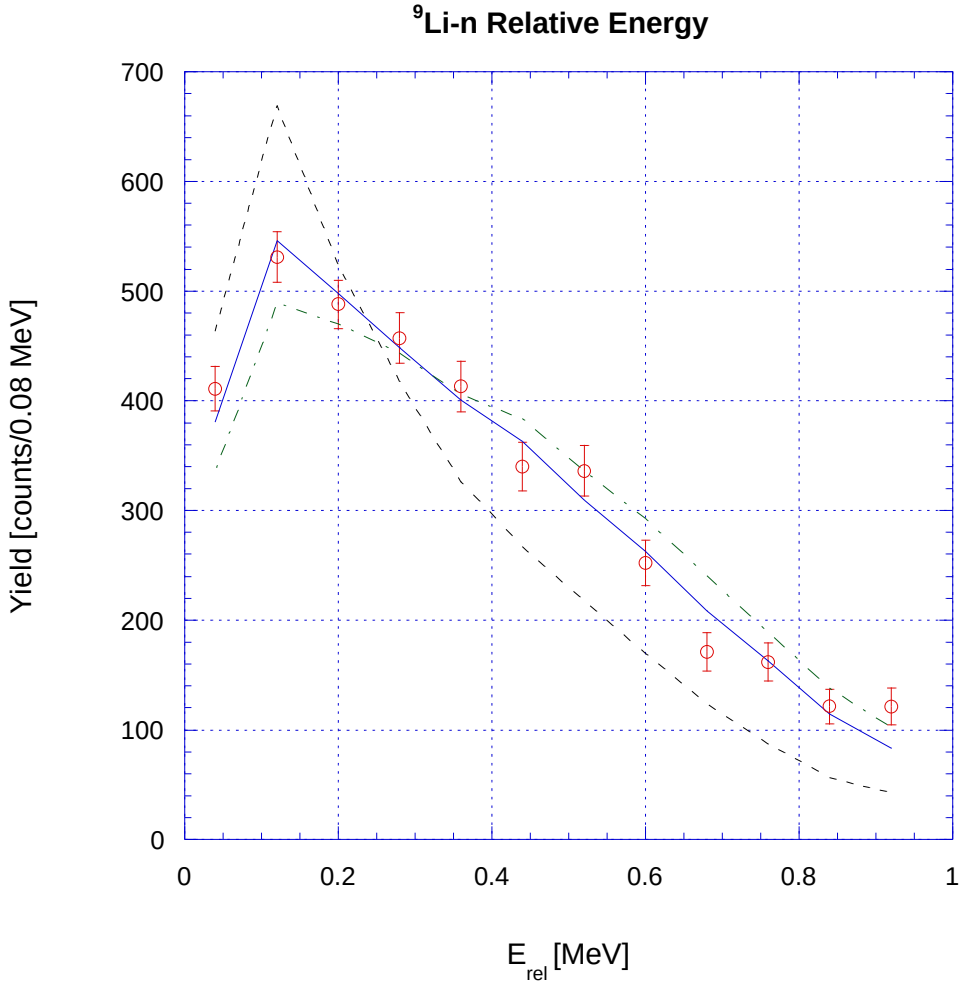

Figure 41 – Fits of the ^{9}Li-n relative energy spectrum with an s-wave and p-wave interaction, including experimental resolution. The best fit, the solid line, uses a scattering length a=-5 fm, p-wave resonance energy E_R=0.4 MeV, and an s/p relative intensity corresponding to 60% s-wave. The dashed and dot-dashed curves use scattering lengths of –10 fm and –1 fm, respectively.

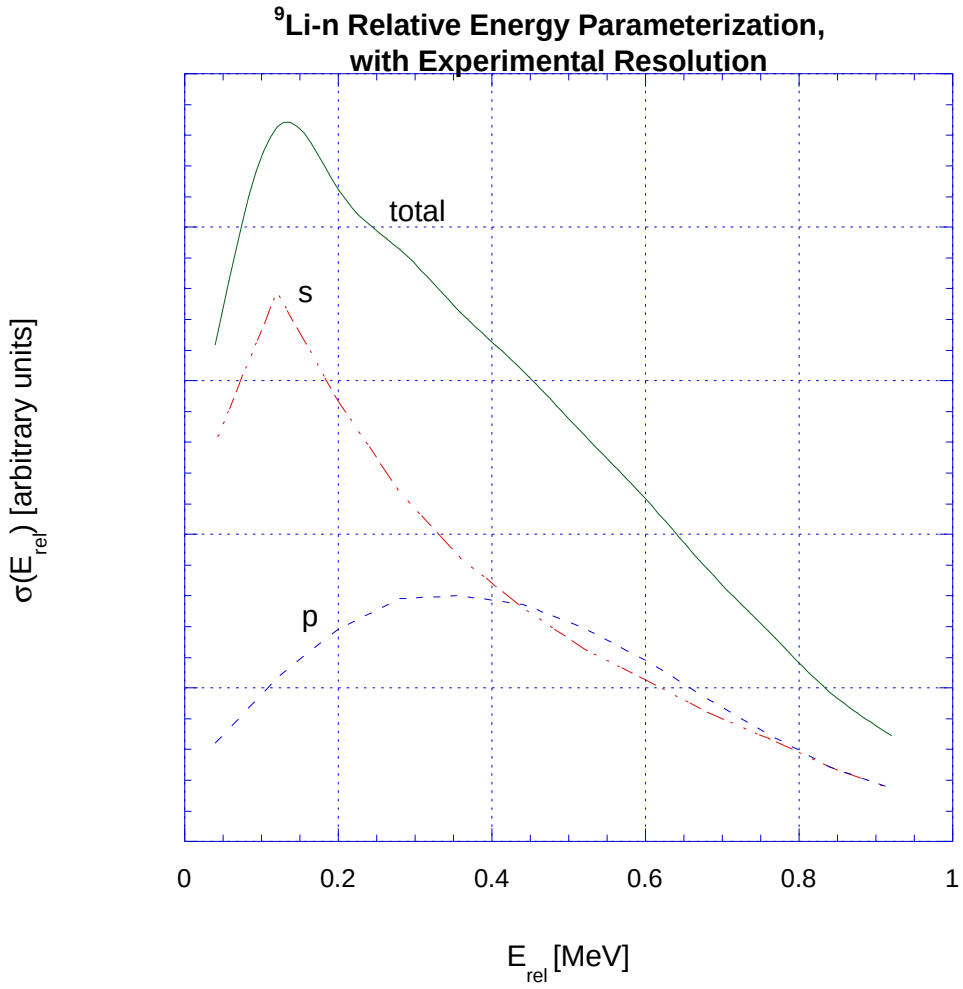

Figure 42 – Energy distribution of the s-wave and p-wave components which were used in the fit of the ^{9}Li-n relative energy data. The curves shown have had the experimental resolution folded in.

4.6 Neutron-Neutron Correlations

One of the most interesting features of ^{11}Li, like other two-neutron halo nuclei, is its Borromean quality. That is, while the three-body ^{9}Li-n-n system is bound, neither the ^{9}Li-n nor the n-n subsystems are bound. Central to an understanding of the ^{11}Li nucleus, then, is a measurement of the degree to which the halo neutrons are correlated in the nucleus. An early study of ^{11}Li dissociation attempted to infer the correlation of the two halo neutrons from the width of the momentum distributions of those neutrons, measured in nuclear breakup reactions. [52] The momentum widths of the halo neutrons were used to predict the angle between the two neutrons' momenta in the center of mass rest frame of the ^{11}Li system. This analysis suggested that in the final state, the two halo neutrons tended to move in the same direction, perhaps suggesting a strong correlation in the nucleus. As mentioned above, another coulomb dissociation experiment by Shimoura *et al.* [17] found a very small relative energy between the two halo neutrons in the final state, and this was interpreted as consistent with an extended 'di-neutron' model, a strongly correlated system. Later analysis of Sackett's coulomb dissociation experiment [53] reported an actual measurement of the cosine of the angle between the two neutrons in the final state center of mass rest frame. The neutron-neutron relative energy spectra collected in this experiment were found to be consistent with those measured by Shimoura, however the distribution of n-n angles was compared very favorably to a completely uncorrelated halo neutron model. The distribution of angles was flat over nearly the entire range from 0 to 180 degrees, with some enhancement present at small angles. The interpretation presented with the data claimed that for an uncorrelated three-body phase space decay, the distribution should be constant over the full range of angles. The enhancement found at small relative angles was claimed to be caused entirely by a more favorable acceptance of the neutron array for neutron pairs travelling in the same direction.

We have already shown that the relative energy between the two neutrons in the final state represents a small portion of the total available decay energy. This result agrees with the analyses of Shimoura and Ieki. However, rather than interpret this observation as evidence of a di-neutron we consider it to be an indication of a direct breakup reaction mechanism, where the ^{9}Li core is pushed out of the ^{11}Li halo by the virtual photon field of the target nucleus.

The complete kinematics of this experiment also permit a measurement of the angle between the two neutrons in the rest frame of the ^{11}Li. Like the data presented by Ieki, this work also finds a large number of neutron pairs with a small relative angle. However, in contrast to the previous work, we find that such a distribution is not consistent with the three-body phase space decay of a resonant state. Rather, the distribution of n-n angles in a phase space breakup mechanism is enhanced near 180 degrees, with little change in the measured distribution caused by the acceptance of the neutron array. Figure 43 shows a simulated distribution of the cosine of the angle between two neutrons, resulting from a three-body phase space breakup. The shape of the distribution in the top panel is independent of decay energy, while the lower panel includes the effect of the acceptance of the Neutron Walls and Beam Sweeping Dipole, with a decay energy of 1 MeV. A decay energy of 1 MeV is larger than the average decay energy measured in the experiment, yet the acceptance of the system causes only a slight upturn of the distribution between $\mathrm{Cos}(\theta) = 0$ and $\mathrm{Cos}(\theta) = 1$.

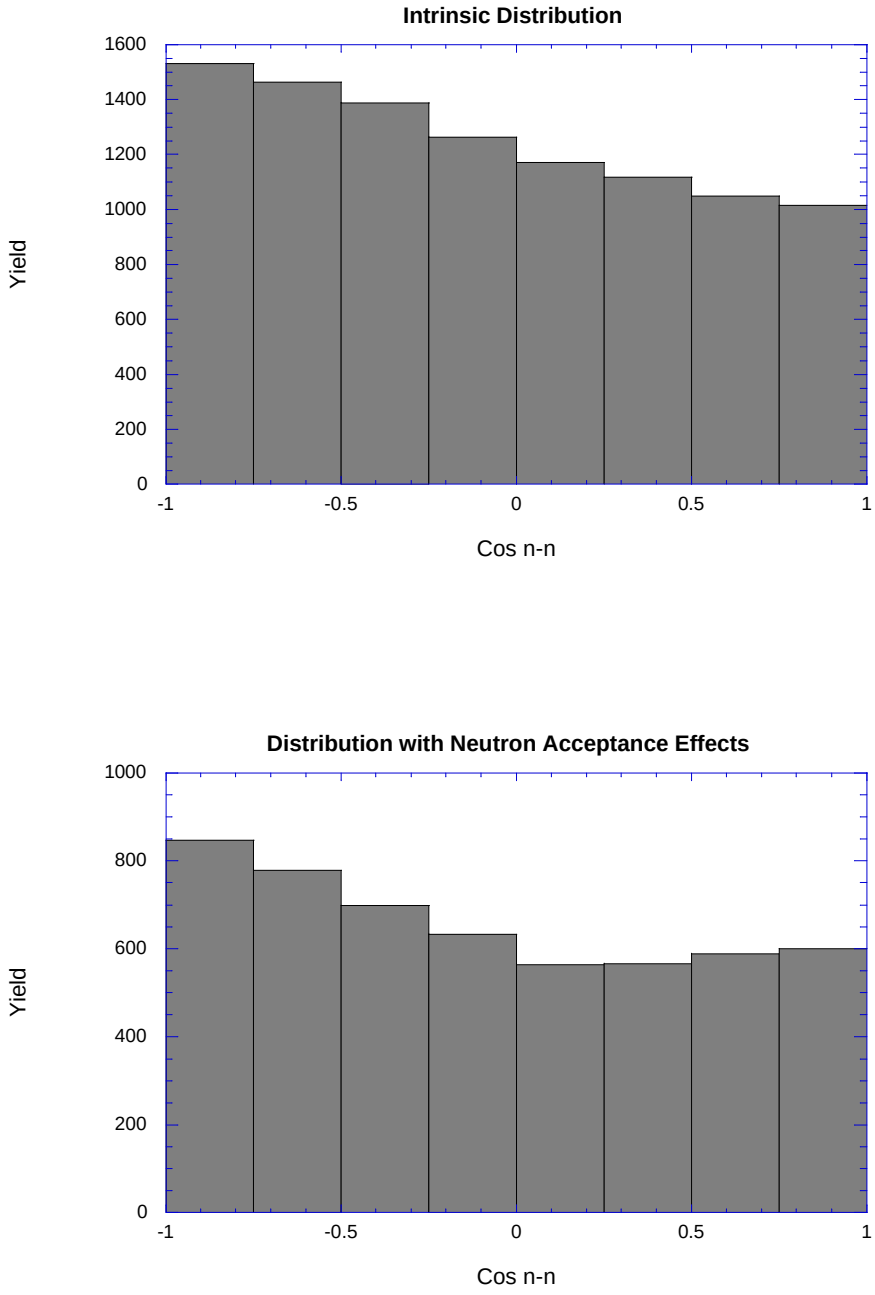

Figure 43 – Monte Carlo simulation of the phase space decay of ^{11}Li, calculating the cosine of the angle between the two neutrons' velocities, in the rest frame of the ^{11}Li center of mass. The top histogram, the intrinsic distribution, is independent of decay energy. The bottom histogram includes the acceptance of the Neutron Walls as used in this work, in detecting events with 1 MeV decay energy.

The asymmetric distribution of neutron-neutron relative angles shown in the Monte-Carlo simulations is surprising, in that it does not agree with the calculation of Ieki et. al., but it can easily be understood. In such a calculation, the first step is to choose a direction and energy for the 9Li fragment. The distribution of fragment energies $N(E_9)$ is given by:

$$N(E_9) = \sqrt{E_9\left(E_{9\max} - E_9\right)}$$

$$E_{9\max} = E_d * \left(\frac{M_{11} - M_9}{M_{11}}\right)$$

where E_d is the total decay energy, and M_{11} and M_9 are the masses of ^{11}Li and ^{9}Li. Next, a velocity is chosen for the two-neutron center of mass such that its momentum is equal to and opposite that of the ^{9}Li fragment. Whatever decay energy remains after computing the velocities of the fragment and two-neutron center of mass is shared equally between the two neutrons. In the rest frame of the two-neutron center of mass, the two neutrons recoil back to back, isotropically in any direction, with equal and opposite momenta.

Figure 44 shows the cosine of the neutron-neutron angle, plotted against the fragment's energy. Three limiting cases can be observed in the plot. The first two occur when the fragment receives either zero kinetic energy, or it gains the maximum energy allowable, E_{9max}. When the fragment receives no kinetic energy, the velocity of the two-neutron center of mass is also zero, and so all of the decay energy is given to the opposing recoil of the two neutrons. In this case, the angle between them is 180°. In the other limiting case, where $E_9 = E_{9max,}$, all of the available decay energy is exhausted by the opposing recoil between the ^{9}Li and the two-neutron center of mass. Now the n-n angle is uniquely 0°. The final unique situation occurs when the n-n angle is 90°. In order for the angle between the two neutrons to be 90°, the velocity of the two-neutron

center of mass in the ^{11}Li rest frame must be equal in magnitude to the velocity of each neutron in the 2-n center of mass rest frame.

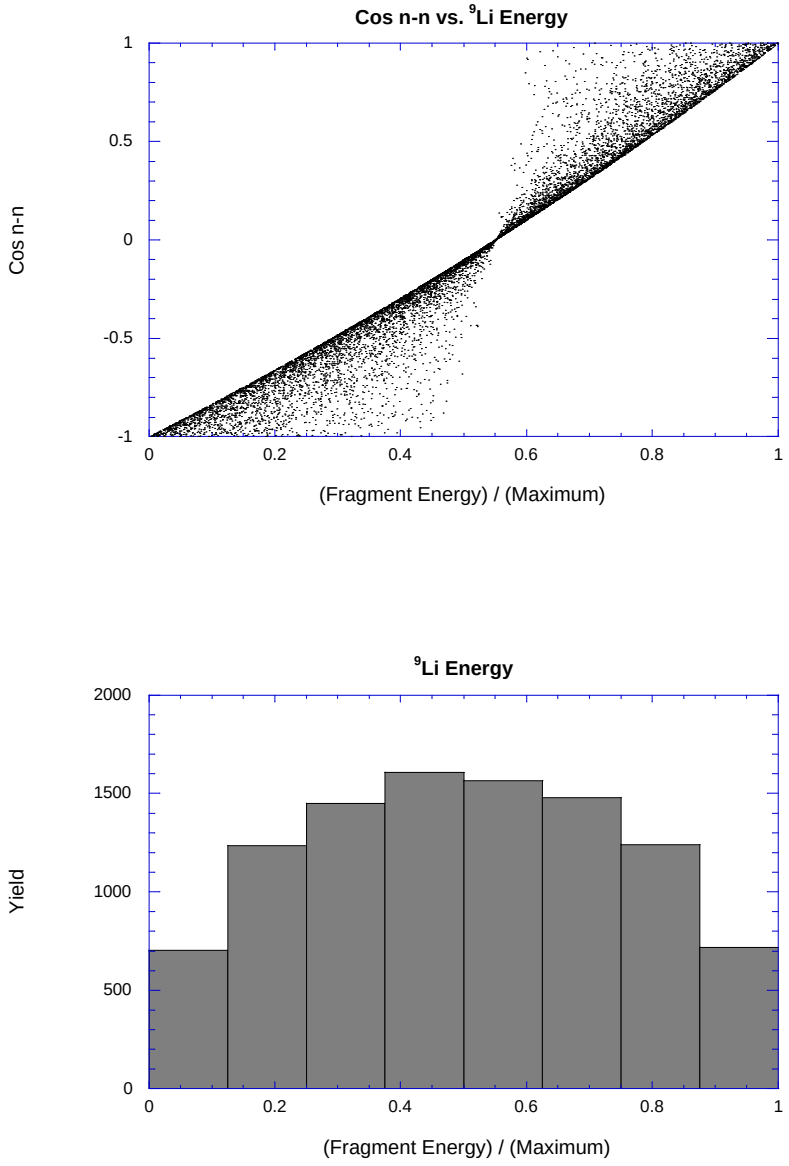

Figure 44 – Results of a Monte Carlo simulation of the phase space breakup of ^{11}Li. The top panel plots the cosine of the angle between the two neutrons' velocities in the rest frame of the ^{11}Li, versus the energy of the ^{9}Li fragment. The bottom panel is a histogram of the decay energy given to the ^{9}Li fragment, showing that the distribution is symmetric.

As the top panel in Figure 44 illustrates, the only time the angle between the neutrons is equal to 90° is when the energy of the fragment E_9/E_{9max} = 0.55. When the ^{9}Li fragment receives 55% of the maximum allowable energy, the velocity of the two-neutron center of mass recoils against it with 55% of its maximum allowable energy, balancing the momentum of the fragment. The remaining decay energy, shared equally between the two neutrons, is such that the velocity of each neutron in the 2-n center of mass rest frame is equal to the velocity of the 2-n system in the ^{11}Li rest frame. The result is that the angle between the two neutrons in the ^{11}Li rest frame is uniquely 90°.

The lower panel in Figure 44 shows that the distribution of fragment energies is symmetric about the point E_9/E_{9max} = 0.50. Because the fragment energies are distributed evenly about the point E_9/E_{9max} = 0.50, while the n-n angle is 90° when E_9/E_{9max} = 0.55, more events are generated with an angle greater than 90° than there are with an angle less than 90°. In the case of the decay of ^{6}He, the alpha core comprises a smaller fraction of the total mass, and so the n-n angle is 90° only when the alpha energy E_4/E_{4max} = 0.60. The slope of the n-n angle distribution is even steeper from 180° to 0° for this case than it is for ^{11}Li decay.

A comparison of this three-body phase space breakup to the actual measured distribution of Cos(θ) shows that such a simulation does a poor job of reproducing the decay of ^{11}Li.

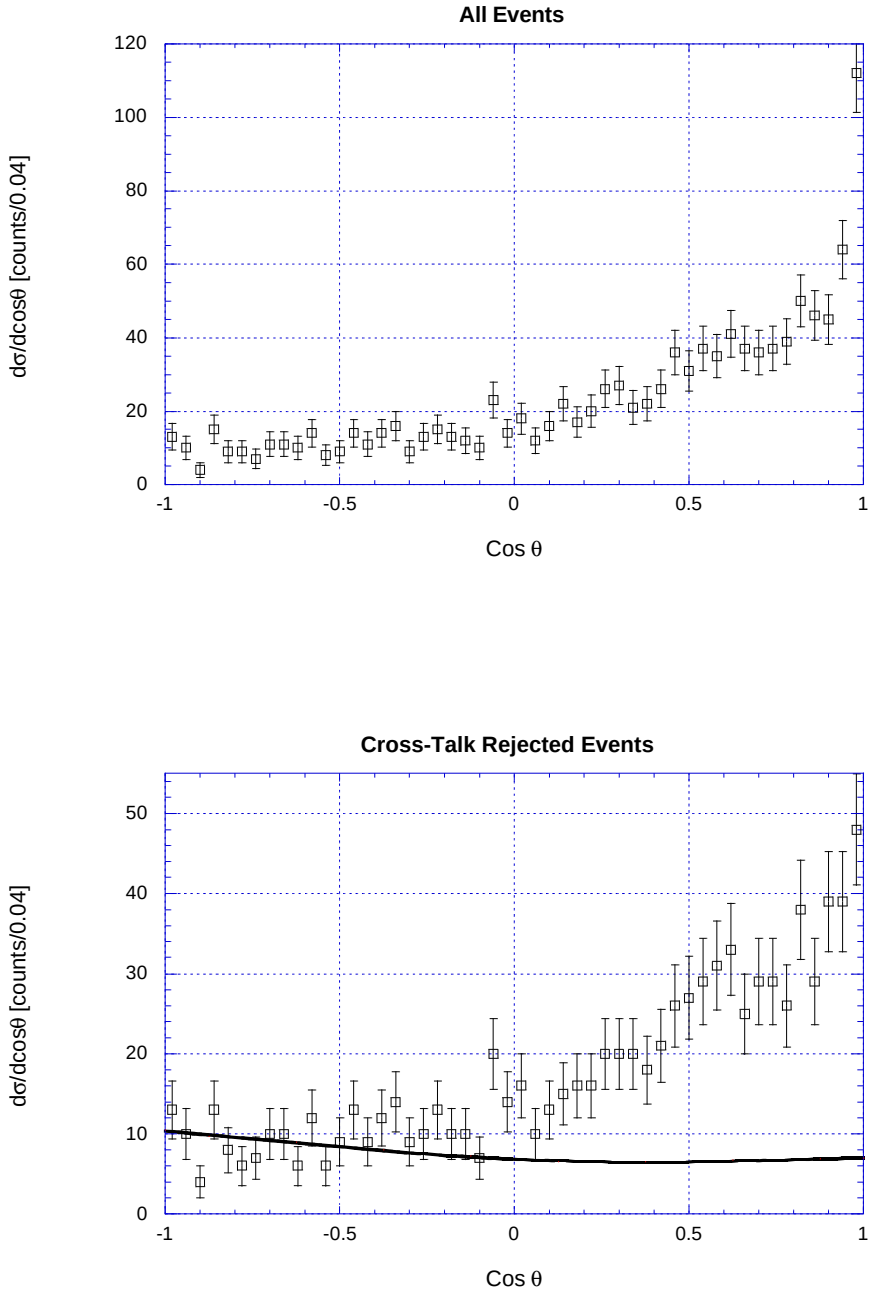

Figure 45 – Distributions of the measured angle between the two neutrons' velocities in the rest frame of the ^{11}Li. The top panel histograms all events, and the bottom panel represents the distribution after cross talk rejection. The curve in the bottom panel is a Monte-Carlo simulation of phase space decay with acceptance effects for events with 1.0 MeV decay energy.

The top panel in Figure 45 shows the raw, measured distribution of neutron-neutron relative angle in the rest frame of the ^{11}Li. The most striking feature of the distribution is the extreme enhancement at Cos(θ) = 1. As mentioned in Section 3.2.2, a common difficulty in experiments that detect coincident neutrons is the problem of cross talk. Cross talk events, events in which one neutron is detected in two separate cells of the detector array, tend to artificially enhance the spectrum in regions of low relative momentum between the neutrons, or in this case, small relative angle. To deal with this problem, we have developed three reliable criteria for the rejection of cross talk, described in Section 3.2.2. The bottom panel in Figure 45 shows the measured distribution of *Cos(q)*, using our method of cross talk rejection. The only qualitative change between the raw and cross-talk-rejected spectra is the suppression of the sharp enhancement present at *Cos(q)*=1. To ensure optimum rejection of cross talk, each of the three rejection criteria was expanded over a larger region, eliminating an increasingly larger fraction of the cross talk as well as the number of true two-neutron coincidence events which are mistaken for cross talk. As more suspect events were rejected, the total number of counts in the *Cos(q)* distribution decreased, but the shape of the spectrum did not deviate from that displayed in Figure 45. Therefore, we feel that the spectrum in the lower panel of Figure 45 represents an optimum rejection of cross talk. Monte Carlo simulations of cross talk rejection in the Neutron Walls have shown that we can expect to reject 80% of all cross talk events, reducing their contribution to the total data set to only 8%. The price of this is a simultaneous rejection of 27% of the true two-neutron coincidence events. If both the raw and cross talk-rejected spectra are summed from *Cos(q)* = -1 to *Cos(q)* = 0.9, away from the main cross talk contamination, the ratio of the number of counts in the two curves is 0.81. This figure is consistent with the predicted rejection rate of 27% of the true coincidences.

Having assured ourselves that the distribution shown in the lower half of Figure 45 is relatively free of cross talk effects, we can compare it to the simulation of an

uncorrelated three-body phase space decay. The solid curve shown with the data in Figure 45 represents the phase space simulation, including the acceptance of the Neutron Walls for decay energies of 1 MeV. Not only does the curve fail to rise appreciably for small relative angles, it actually displays an enhancement for large angles, as described earlier in this section.

The large number of events observed with a small relative angle between the two neutrons should not be surprising, considering our analysis of the decay energy spectra collected in this measurement. Recall that in contrast to a three-body phase space decay, a large portion of the available decay energy tended to be exhausted by the ^{9}Li - two-neutron center of mass subsystem. A significantly smaller fraction of the available decay energy was measured in the neutron-neutron relative energy spectrum. Since the angle between the neutrons in the ^{11}Li rest frame is determined by the neutron-neutron relative energy, these two observations are consistent. As in Section 4.3, we interpret this measurement as the manifestation of a direct breakup process in which the coulomb field of the target nucleus pushes the ^{9}Li core out of the halo of the ^{11}Li, leaving the two halo neutrons as spectators in the process.

In addition to the measurement of the neutron-neutron relative angle, we also have constructed a histogram of the relative momenta between the two neutrons. This method of probing the correlation between halo neutrons has been used in every kinematically complete measurement of ^{11}Li to date. [16, 17, 2, 53] In this analysis, we do not compute the complete relative momenta between the two neutrons, as the z – component (beam direction) of the neutrons tends to be simply a reflection of the beam energy. Rather, we calculate the relative momenta in the transverse plane only. For comparison to an uncorrelated set of neutrons measured by the same system, we randomized the set of momenta measured for neutron 2, and calculated the relative momenta between two neutrons from different events. This set of mixed events is labeled “randomized” in the plot below.

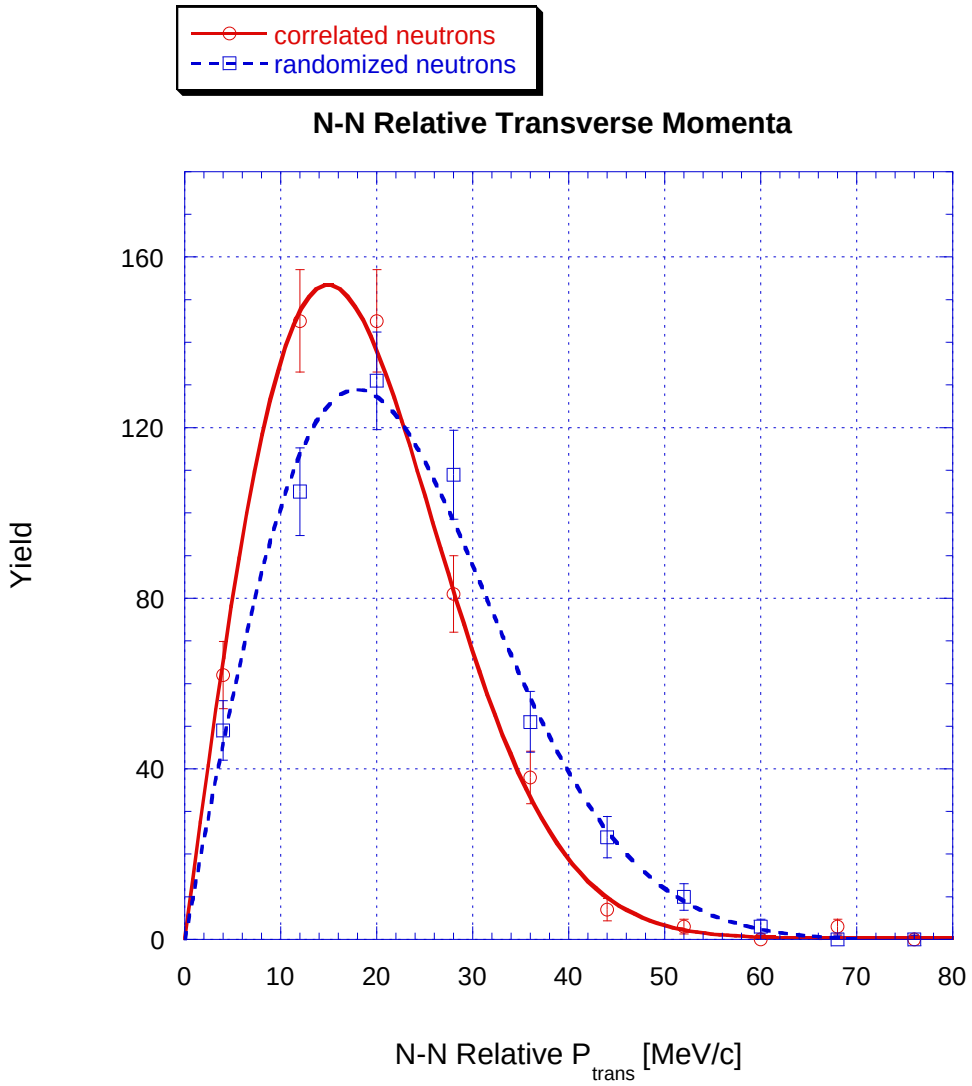

Figure 46 – n-n Relative transverse momenta. The solid curve connects points calculated for actual neutron pairs detected in coincidence. The dotted curve represents the same calculation for neutron pairs which have been mixed randomly between events.

As we might have expected from the n-n relative energy spectra and the n-n angle distributions, the correlated set of neutrons display a significantly lower relative momentum than the set which has been randomized by event mixing. Again, this effect is produced by a decay mechanism in which the n-n subsystem gets a small portion of the total available decay energy.

5 Summary

We have studied the dissociation of ^{11}Li at 23 MeV/A on targets of aluminum, tin, and lead. The fragment singles data facilitated a calculation of the total two-neutron removal cross section, σ_{2n}. We obtained values of $\sigma_{2n} = 0.7 \pm 0.1$ b on aluminum, $\sigma_{2n} = 2.2 \pm 0.4$ b on tin, and $\sigma_{2n} = 5.0 \pm 0.4$ b on lead. The two-neutron removal cross section we measure on the lead target agrees with the measurement of Sackett *et al*. [1].

The ^{9}Li—two-neutron coincidence data were used to map out the coulomb dissociation cross section as a function of excitation energy. The virtual photon spectrum was divided out, yielding a dipole strength function dB(E1)/dE. This curve was fitted with a Breit-Wigner resonance shape, with a resonant energy of E_R=0.83 MeV and a width Γ=1.5 MeV. Both the resonance energy and the width of the curve are larger than that measured by Sackett et al. (E_R=0.7 MeV, Γ=0.8 MeV). These differences are probably caused by the current experiment's larger acceptance for events with high decay energy.

The strength function was well reproduced by a calculation by Pushkin *et al*., [35]. The shape of the curve is dependent only on the binding energy of the initial state and suggests a direct breakup reaction mechanism rather than decay through a resonance. In an experiment similar to this one, Shimoura *et al*. [17] found that a large fraction of the available decay energy was exhausted by the recoil of the ^{9}Li fragment against the two-neutron center of mass. This observation also pointed to a direct breakup mechanism in which the ^{9}Li fragment was pushed out of the neutron halo by the coulomb field of the target nucleus. This work also finds that the majority of the decay energy is exhausted by the ^{9}Li—two-neutron center of mass recoil. This finding is in contrast to the study by Sackett *et al*., who found that their data were well described by a phase-space breakup model.

For each two-neutron coincidence measurement, the angle between the recoiling neutrons was calculated in the ^{11}Li center of mass rest frame. We found that the

distribution was fairly constant, except for an enhancement at small relative angles. While our distributions resemble those measured by Sackett *et al*., they reported that the spectrum was well described by a completely uncorrelated phase-space breakup. However, we found that a phase space breakup of ^{11}Li actually tends to favor large relative angles, and that our data exhibit a strong directional correlation. Rather than a manifestation of a strong pairing interaction in the ^{11}Li ground state, the correlation found in our data is probably caused by the direct breakup mechanism described in the discussion of the dipole strength function. Because the ^{9}Li fragment is pushed away from the neutron halo by the coulomb field of the target nucleus, in the ^{11}Li center of mass frame the two halo neutrons tend to recoil in the same direction – opposite the direction of the fragment.

^{9}Li—one-neutron coincidences measured from dissociation on the aluminum target were used to study the nature of the neutron unbound ^{10}Li system. Our data showed evidence for low-energy s-wave strength, as well as a higher energy p-wave resonance. Using the parameterizations for s- and p-wave interactions given by Bertsch *et al*., we fitted our data with an s-wave scattering length of –5 fm, a p-wave resonance energy of 0.4 MeV, and a relative intensity corresponding to 60% s-wave strength.

Bibliography

Bibliography

[1] Sackett *et al*., Phys. Rev. **C48** (1993) 118.

[2] Ieki *et al*., Phys. Rev. Lett. **70** (1993) 730.

[3] D. Sackett Ph.D. Thesis, Michigan State University (1992)

[4] D. Cebra *et al*., Nuclear Instruments and Methods in Physics Research **A313** (1992) 367.

[5] W. Press, S. Teukolsky, W. Vetterling, B. Flannery, *Numerical Recipes in Fortran, Second Edition* (Cambridge University Press, Victoria Australia, 1992) p704.

[6] J. Wang Ph.D. Thesis, Michigan State University (1999)

[7] I. Tanihata *et al*., Phys. Rev. Lett., **55** (1985) 2676.

[8] T. Kobayashi *et al*., Phys. Rev. Lett., **60** (1988) 2599.

[9] A. Goldhaber, Phys. Lett. **B53** (1974) 306.

[10] P.G. Hansen and B. Jonson, Europhys. Lett. **4** (1987) 409.

[11] R.N. Boyd and I. Tanihata, Phys. Today (1992) 44.

[12] T. Kobayashi *et al*., Phys. Lett. **B232** (1989) 51.

[13] T. Kobayashi *et al*., Phys. Lett. **B232** (1989) 51.

[14] K. Ikeda, Nucl. Phys. **A538** (1992) 355c.

[15] F. Ajzenberg-Selove, Nucl. Phys. **A490** (1988) 1.

[16] M. Zinser *et al*., Nucl. Phys. **A619** (1997) 151.

[17] S. Shimoura *et al*., Phys. Lett. **B348** (1995) 29.

[18] B.M. Sherrill *et al*., Nucl. Instr. and Meth. **B56/57** (1991) 1106.

[19] D. Swan, D.J. Morrissey, and J. Yurkon, Nucl. Instr. and Meth. **A348** (1994) 314.

[20] P.D. Zecher *et al*., Nucl. Instr. and Meth. **A401** (1997) 329.

[21] P.D. Zecher, Ph.D. Thesis, Michigan State University (1996).

[22] J. Wang *et al*., Nucl. Instr. and Meth. **A397** (1997) 380.

[23] T. Kobayashi, Phys. Lett. **B232** (1989) 51.

[24] K. Riisager *et al*., Nucl. Phys. **A540** (1992) 365.

[25] N.A. Orr *et al*., Phys. Rev. Lett. **69**, (1992) 2050.

[26] R. Anne *et al*., Phys. Lett. **B250** (1990) 19.

[27] F. Barranco, E. Vigezzi, and R.A. Broglia, Z. Phys. **A356** (1996) 45.

[28] N.A. Orr, Nucl. Phys. **A616** (1997) 155.

[29] P.G. Hansen, Phys. Rev. Lett. **77** (1996) 1016.

[30] H. Esbensen, Phys. Rev. **C53** (1996) 2007.

[31] I. Tanihata *et al*., Phys. Lett. **B287** (1992) 307.

[32] R. Kurz, computer code TOTEFF, University of California Report UCRL-11339, unpublished (1964), modified for NE-213 by R. Doering, MSU (1974)

[33] C.F. Weizsacker, Z. Phys. **88** (1934) 612.

[34] E.J. Williams, Phys. Rev. **45** (1934) 729.

[35] A. Pushkin, B. Jonson, and M.V. Zhukov, J. Phys. G. **22** (1996) L95.

[36] G. Baur "*Proceedings of International Symposium on Structure and Reactions of Unstable Nuclei*", Niigata, Japan (1991).

[37] T. Nakamura *et al*., Phys. Lett. **B331** (1994) 296.

[38] J. Bush *et al*., Phys. Rev. Lett. **81** (1998) 61.

[39] M. Thoennessen *et al*., to be published (1998).

[40] P.G. Hansen, Nucl. Phys. **A630** (1998) 285.

[41] B.A. Brown, Proc. Int. School on Heavy Ion Physics, 4^{th} Course: Exotic Nuclei, (Erice 1997)

[42] T. Kobayashi *et al*., Nucl. Phys. **A616** (1997) 233c.

[43] S. Shimoura *et al*., Nucl. Phys. **A616** (1997) 208c.

[44] H.G. Bohlen *et al*., Nucl. Phys. **A616** (1997) 254c.

[45] S. Shimoura *et al*., Nucl. Phys. **A616** (1997) 387c.

[46] K.H. Wilcox *et al*., Phys. Lett. **B59** (1975) 142.

[47] H.G. Bohlen *et al*., Z. Phys. **A344** (1993) 381.

[48] B.M. Young *et al*., Phys. Rev. **C49** (1994) 279.

[49] R.A. Kryger *et al*., Phys. Rev. **C47** (1993) R2439.

[50] A.I. Amelin *et al*., Sov. J. Nucl. Phys. **52** (1990) 782.

[51] G.F. Bertsch, K. Hencken, and H. Esbensen, Phys. Rev. **C57** (1998) 1366.

[52] I. Tanihata *et al*., Phys. Lett. **B287** (1992) 307.

[53] K. Ieki *et al*., Phys. Rev. **C54** (1996) 1589